Journal of Applied Physics

RESEARCH ARTICLE | OCTOBER 19 2023

Plasma propulsion modeling with particle-based algorithms

F. Taccogna ; F. Cichocki ; D. Eremin ; G. Fubiani ; L. Garrigues

J. Appl. Phys. 134, 150901 (2023)
https://doi.org/10.1063/5.0153862

AIP Publishing

Journal of Applied Physics PERSPECTIVE pubs.aip.org/aip/jap

Plasma propulsion modeling with particle-based algorithms

Cite as: J. Appl. Phys. **134**, 150901 (2023); doi: 10.1063/5.0153862
Submitted: 12 April 2023 · Accepted: 30 September 2023 ·
Published Online: 19 October 2023

F. Taccogna,[1,a)] F. Cichocki,[2] D. Eremin,[3] G. Fubiani,[4] and L. Garrigues[4]

AFFILIATIONS

[1]Institute for Plasma Science and Technology (ISTP), CNR, Bari, Italy
[2]Fusion and Technology for Nuclear Safety and Security Department (FSN), ENEA, Frascati, Italy
[3]Institute of Theoretical Electrical Engineering, Ruhr University Bochum, Universitätsstraße 150, 44801 Bochum, Germany
[4]LAPLACE, Université de Toulouse, CNRS, INPT, UPS, Toulouse, France

[a)]**Author to whom correspondence should be addressed:** francesco.taccogna@cnr.it

ABSTRACT

This Perspective paper deals with an overview of particle-in-cell/Monte Carlo collision models applied to different plasma-propulsion configurations and scenarios, from electrostatic ($\boldsymbol{E} \times \boldsymbol{B}$ and pulsed arc) devices to electromagnetic (RF inductive, helicon, electron cyclotron resonance) thrusters, as well as plasma plumes and their interaction with the satellite. The most important items related to the modeling of plasma–wall interaction are also presented. Finally, the paper reports new progress in the particle-in-cell computational methodology, in particular, regarding accelerating computational techniques for multi-dimensional simulations and plasma chemistry Monte Carlo modules for molecular and alternative propellants.

I. INTRODUCTION

Electric propulsion (EP) has been developed since the early 1960s, and its use onboard satellites, orbiting platforms, and interplanetary probes has increased significantly in the last two decades.[1–4] The need for a detailed understanding of the working physics and precise estimation of the performance to enable cheaper innovative designs has spurred the development of a large number of simulation codes, with particle-based methods[5,6] playing a significant role.

Plasma thrusters can be classified in terms of the gas ionization process, the basic conversion mechanism for the kinetic energy gained by the ions,[7] or the main acceleration mechanism of the plasma.[1] In this Perspective paper on EP numerical simulations, however, we will classify thrusters in terms of their modeling needs. From this point of view, electric thrusters (with the exception of electro-thermal thrusters) fall within the electrostatic (ES) and electromagnetic (EM) categories. Thrusters belonging to the former can be modeled by retaining only Poisson's equation, while the second category requires including the full set (or a subset) of Maxwell's equations.

ES thrusters are based on the acceleration of positive charges under the action of a DC electric field, with cathode emitting electrons being used to neutralize the positive charge flow, thus preventing space vehicle charging.[2] Most ES thrusters feature a cylindrical geometry and an electrical power input varying from hundreds of W to tens of kW. In ES thruster concepts such as gridded ion engines (GIEs)[8] and $\boldsymbol{E} \times \boldsymbol{B}$ based devices [see, e.g., Hall thrusters (HTs),[9–11] cylindrical HT,[12] highly efficient multistage plasma thruster (HEMPT),[13] cusped-field thruster (CFT),[14] and co-axial magneto-isolated anode (CAMILA)[15]], positive ions are generated under the ionization of a propellant gas (usually Xe) by high energetic electrons, and are accelerated by an imposed potential difference between two electrodes. In the case of GIEs, the electrodes are represented by a system of polarized electrostatic grids negatively biased with respect to the plasma potential and featuring multi-apertures. In $\boldsymbol{E} \times \boldsymbol{B}$ thrusters, like the HT, the potential difference is imposed between an inner anode and an external cathode, and the DC electric field that accelerates the ions is sustained inside the discharge channel under the action of an applied magnetic field. The growth of the micro and nano-satellites market has fostered the development of alternative device concepts to deal with the low electrical power available (less than 100 W). Colloid thrusters (CTs)—also called electrospray thrusters—enter in the category of ES engines, although positive charges are now liquid

droplets produced by an electrospray process.[16] Finally, in pulsed arc thrusters (PATs), the plasma expands after being formed from the ablation [in pulsed plasma thruster (PPT)] or the evaporation [in vacuum arc thruster (VAT)] of a solid propellant grain.[17] PATs can be considered ES thrusters because the magnetic field induced by the plasma current is generally negligible compared to either the externally applied field (in VATs) or the field induced by the external circuit current (in PPTs).

Differently, electromagnetic (EM) thrusters ionize and accelerate the propellant under the combined action of time-dependent magnetic and electric fields, and, in some cases, electromagnetic waves.[1,2,18] Therefore, the necessity of solving for the full (reduced in some cases) set of Maxwell's equations is associated with two different reasons: the type of electron heating for plasma generation and the type of plasma acceleration. Regarding the former, power absorption can be due to RF induction heating (as in inductive plasma thrusters, IPTs[19–23]) or wave heating (as in RF Helicon wave[24] HPT; microwave electron cyclotron resonance,[25–27] ECRT; and ion cyclotron resonance, VASIMR[28] thrusters). This sub-category of EM thrusters is electrodeless, thus having the advantage of limiting the plasma–wall interaction and mitigating the problem of thruster lifetime. Regarding plasma acceleration, since EM thrusters are quasi-neutral (except inside the Debye sheaths at the walls), this is related to a $\boldsymbol{j} \times \boldsymbol{B}$ term (hence, the naming Lorentz Force Accelerators, LFAs), and $\boldsymbol{B}$ can present, in some cases, a significantly large self-induced component (and hence the need of including, at least, Ampère's law). This is the case of the magneto-plasma-dynamic thrusters (MPDTs), where the magnetic induction field can be either applied (AF)[29] or self-induced (SF).[30]

Today, the design and development of electric thrusters are still semi-empirical and require long and expensive life tests. There is a need to better understand key plasma processes occurring in the complex partially magnetized plasmas, such as electron heating, electron and ion transport, the plasma–wall interaction, or the ion-induced erosion, and to address the question of alternative propellants. The experimental characterization of electric thrusters in ground-test facilities has some intrinsic issues: (i) the difficulty of having reliable diagnostics on devices that often do not allow direct and non-invasive access; (ii) the influence of the ground-test facilities on thruster performance (operations of the thruster are very sensitive to the chamber background pressure[31]); (iii) the reproducibility of the natural thruster working conditions, such as the typical space environment conditions or flow (for atmospheric breathing EP concept[32]). Numerical simulations play a crucial role since they can control these effects. Moreover, it is also of paramount importance to better understand the discharge configuration and the emitted plasma plume interaction with the spacecraft for realistic geometries, which require the development of 3D numerical tools. In this respect, full-Particle-in-Cell (PIC) simulations would be very expensive, but they could still be used to improve the precision of more affordable 3D hybrid PIC-fluid codes,[33–35] in which electrons are treated as a fluid, and which generally make strong assumptions affecting the physics (e.g., the polytropic approximation). If these improved 3D hybrid PIC-fluid codes were made available to the industry, the efficiency of existing products could be increased, and new design breakthroughs would be enabled.

In recent years, numerical simulations have increasingly benefited the basic understanding leading to engineering optimization of electric thrusters. This is due to several concurrent contributions: (i) the evolution of computer hardware[36] that has allowed the representation of multi-dimensional geometries and multi-scale phenomena avoiding numerical tricks (e.g., artificial vacuum permittivity,[37] mass ratio,[38] size scaling[39]), (ii) the implementation of sophisticated new algorithms and numerical diagnostic tools,[40] and (iii) the availability of new collisional[41] and surface interaction[42] data.

In particular, the kinetic and non-local description is indispensable to capture the intrinsic nature of different EP concepts since low-pressure partially magnetized plasmas feature a large number of inherently kinetic, non-equilibrium, and non-local phenomena. Among the different kinetic approaches[43] available (particle-based, grid-based, and polynomial expansion), the particle representation allows for a simple and intuitive implementation to account for a detailed description of plasma–gas and plasma–wall interactions, although it suffers from the inevitable but controllable limitation due to inherent discrete particle noise[44–47] and from its computationally intensive nature. This Perspective article critically discusses the different particle-based methodologies used to describe the plasma (electron and ion species) and coupled gas phases in both the discharge and plume regions of the most common EP configurations.

The paper is organized as follows. Section II introduces the most commonly used particle-based models for the plasma and gas species. Then, the different Particle-in-Cell schemes for the plasma discharge simulations are presented in Sec. III. Models available for plasma plumes simulation, satellite interaction, and plume-electromagnetic compatibility are presented in Sec. IV, while future simulation challenges are addressed in Sec. V. Conclusions are drawn in Sec. VI.

Finally, we assembled a very comprehensive list of references that should be credited for the original work.

II. PARTICLE-IN-CELL AND MONTE CARLO SIMULATIONS

The Particle-in-Cell (PIC) technique[5,43,48–51] is a Lagrangian/Eulerian (or particle-mesh) method, applicable to low temperature and low pressure discharges like those of electric thrusters that are characterized by a weakly coupled and low collisional plasma, exhibiting non-equilibrium behavior and non-local properties.

The PIC approach dates back to the late 1950s when pioneering simulations of Buneman[52] and Dawson[53] were implemented to study some basic properties of collisionless plasmas. A few years later, the first stochastic Monte Carlo simulations of the charged particle transport were applied to drift tubes[54,55] and gas discharges,[56–58] while aerodynamicists developed a particle-particle simulation method for the neutral species collisions,[6] known as Direct-Simulation Monte Carlo (DSMC). Subsequently, the PIC approach started to be coupled with Monte Carlo methods for the simulation of collisional processes[59,60] also in plasma discharges, with the first applications to plasma thrusters appearing in 1990s, thanks to the contributions of Arakawa's[61] and Martinez-Sanchez's[62,63] research groups and Adam-Héron.[64]

In PIC/Monte Carlo models, the distribution function f of both plasma (ions and electrons) and neutral gas species is approximated with an ensemble of N macro-particles (or super-particles) as

$$f(\boldsymbol{r}, \boldsymbol{v}) = \sum_{p=1}^{N} w_p S(\boldsymbol{r} - \boldsymbol{r}_p)\delta(\boldsymbol{v} - \boldsymbol{v}_p), \tag{1}$$

where w_p is the statistical weight of the pth macro-particle (many models considering a uniform weight for all particles of a given species); $\boldsymbol{r}_p$ and $\boldsymbol{v}_p$ are its position and velocity vector, respectively; δ is the Dirac delta function; and S is the macro-particle cloud shape function determining how the macro-particle weight is distributed in space and satisfying the integral relation $\iiint S(\boldsymbol{r}')\mathrm{d}^3r' = 1$. Commonly used shape functions in PIC methods are the Dirac delta δ (for the nearest-grid-point, NGP, scheme), the rectangular function (for the cloud-in-cell, CIC, scheme), or the triangular function (for the triangular shaped cloud, TSC, scheme).[48] Directly related to the cloud shape function and the chosen PIC mesh is then the interpolation function (also known as assignment function shape), defined as

$$W(\boldsymbol{r}) = \iiint S(\boldsymbol{r}')b_0\left(\frac{\boldsymbol{r} - \boldsymbol{r}'}{\Delta r}\right)\mathrm{d}^3r', \tag{2}$$

where b_0 is the rectangular function and Δr is the mesh spacing.[48] Most authors in the literature refer directly and exclusively to this interpolation function W as it enables a direct computation of particle bulk properties at the mesh nodes, without any need of integration [see Eq. (6)]. The three examples given above for the shape function (Dirac delta, rectangular, and triangular functions) correspond to b-spline interpolation functions and to b_0 (NGP), b_1 (CIC), and b_2 (TSC) splines, respectively.

As illustrated in Fig. 1, the PIC/Monte Carlo method consists in solving the corresponding species (electron, ion, and atom/molecule) Boltzmann's equations featuring the following steps:

1. The trajectories of the macro-particles between collisional events are obtained by solving Newton's equation (assuming negligible relativistic effects, given the electron energy ranges of interest in EP),

$$\begin{cases} m_p \frac{\mathrm{d}\boldsymbol{v}_p}{\mathrm{d}t} = q_p(\boldsymbol{E}_p + \boldsymbol{v}_p \times \boldsymbol{B}_p), \\ \frac{\mathrm{d}\boldsymbol{r}_p}{\mathrm{d}t} = \boldsymbol{v}_p, \end{cases} \tag{3}$$

where q_p and m_p are the elementary particle charge and mass, respectively, while $\boldsymbol{E}_p$ and $\boldsymbol{B}_p$ are the electric and magnetic fields at the macro-particle location, obtained from their values $\boldsymbol{E}_g$, $\boldsymbol{B}_g$ at the grid point g as

$$\begin{cases} \boldsymbol{E}_p = \sum_g \boldsymbol{E}_g W(\boldsymbol{r}_g - \boldsymbol{r}_p), \\ \boldsymbol{B}_p = \sum_g \boldsymbol{B}_g W(\boldsymbol{r}_g - \boldsymbol{r}_p). \end{cases} \tag{4}$$

The trajectories of the macro-particles are obtained through the integration of the discretized form of Eq. (3) over a time step Δt (leap frog method with Boris algorithm being the most commonly used[5,48]).
2. The macro-particles may reach the physical walls or computational domain boundaries, where various processes (absorption, reflection, emission of additional particles) may take place as defined by the plasma-surface and gas-surface models. Here, again, different probabilistic Monte Carlo models can be used depending on the process implemented (see Sec. III C). This step may also include any particle injection algorithm, which is often necessary to maintain the plasma.
3. The collisions of the particles are handled through the Nanbu (no-time counter scheme) stochastic Monte Carlo rules[60,65,66]

$$f(t + \Delta t, \boldsymbol{v}_p) = (1 - P)f(t, \boldsymbol{v}_p) + PQ(\boldsymbol{v}_p), \tag{5}$$

with the following probabilistic interpretation: inside a cell (the distribution function f is considered independent of $\boldsymbol{r}$), a particle with velocity $\boldsymbol{v}_p$ will collide with probability P, according to the collision laws (determining the post-collisional velocity components) described by $Q(\boldsymbol{v}_p)$. Different Monte Carlo schemes have been set up for electron–molecule, ion–molecule, molecule–molecule, and Coulomb collisions[60] based on the linear/non-linear character of the corresponding Boltzmann's equation and on the different nature of the interacting force between the colliding partners. The Monte Carlo schemes for collisions can be roughly classified in two main categories: (i) Monte Carlo Collision (MCC) or Test-Particle Monte Carlo (TPMC) methods, which consider a fluid collisional background as the target for the "projectile" macro-particles and (ii) Direct-Simulation Monte Carlo (DSMC) methods, in which collisions between macro-particle pairs are actually considered. Electron-neutral and ion-neutral collisions are often simulated with MCC/TPMC algorithms, while collisions between neutrals or between charged particles with DSMC.
4. For the most general electromagnetic (EM) scheme, the charge and current densities of macro-particles as well as the electric/magnetic fields are computed on a discrete grid. The latter quantities are obtained from Maxwell's equations with a dedicated solver that takes into account the space charge density ρ_c and current density $\boldsymbol{j}$ generated by the ensemble of

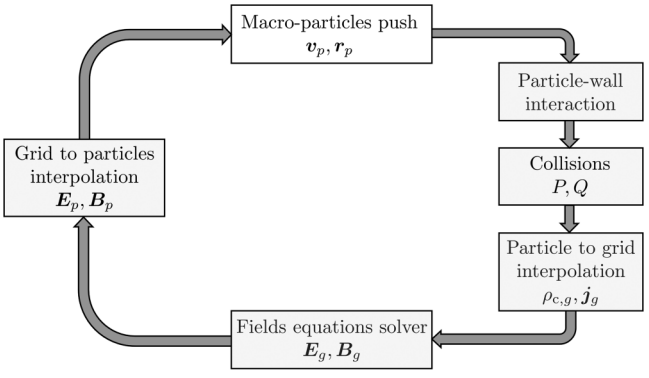

FIG. 1. Scheme of a typical PIC–Monte Carlo loop.

charged particles at each grid point g,

$$\begin{cases} \rho_{c,g} = \frac{1}{V_g}\sum_p q_p w_p W(\boldsymbol{r}_g - \boldsymbol{r}_p), \\ \boldsymbol{j}_g = \frac{1}{V_g}\sum_p q_p w_p \boldsymbol{v}_p W_j(\boldsymbol{r}_g - \boldsymbol{r}_p), \end{cases} \tag{6}$$

with V_g representing the cell volume associated to the grid point, and W_j representing the interpolation function for the current density (which may be different from the one used for the charge density in the charge-conserving methods[67–70]). In the electromagnetic case, the effects of an external power source appear as boundary conditions on the electromagnetic fields (or the scalar and vector potentials) in Maxwell's equations or a prescribed external time-dependent current density in an antenna or a driving coil, the latter being relevant for inductively coupled plasma (ICP) discharges. The magnetic field is equal to the sum of an induced time-dependent and an externally generated static magnetic fields. For the electrostatic (ES) case, on the other hand, the magnetic field is imposed while the electric field is calculated from the space charge density, by solving Poisson's equation with a power source typically specifying a fixed voltage between the electrodes.

The PIC/Monte Carlo method is, therefore, characterized by a combination of different algorithms with their own accuracy order: the pusher (time-integrator) to solve the mesh-free equations of motion, the field solver for the mesh-based Maxwell's equations, the interpolation schemes to couple mesh-free quantities with the mesh-based ones, and the stochastic Monte Carlo rules for volumetric binary collisions and surface processes. All parts are important and we have to deal with their numerical error to reduce the full error of the PIC method. The physical constraints, such as the conservation of mass, momentum, and energy are important to the physical experiments and should be conserved by the underlying numerical schemes. The standard PIC scheme described above has then to be adapted to the considered scenario, e.g., an ES or EM one. Furthermore, the different numerical ideas to solve the time-dependencies, e.g., explicit or implicit schemes (see Sec. V C), have a strong influence on the numerical stability of PIC codes.[47] For example, in EM codes, an explicit solver with integration time step Δt has to satisfy $\omega_{p,e}\Delta t < 0.2$, where $\omega_{p,e}$ is the electron plasma frequency, or the Courant–Friedrichs–Lewy (CFL) condition $c \leq \Delta r/\Delta t$, where c is the phase wave velocity and Δr the mesh spacing. In addition, the grid solver has to satisfy the electron Debye length $\Delta r \leq \zeta\lambda_{D,e}$, where $\lambda_{D,e}$ is the Debye length and ζ is a constant of order 1. Finally, the collision probabilities should be sufficiently small, in order to minimize the effect of "missed" collisions (i.e., multiple collisions during a time step). It is a good practice to keep the collision probability P of a given species below 5%–10% to limit the error to less than 1%.[51,71] To conclude, despite the difficulties and constraints described above, the particle representation enables an efficient handling of the multi-dimensionality associated with non-equilibrium discharges and considerable flexibility to model advanced physics (such as internal energy excitation, chemical reactions, surface interactions, etc.).

III. PIC MODELS OF THRUSTER DISCHARGES

A. Electrostatic PIC

In electrostatic PIC models, the self-induced field effects are generally considered negligible, at least concerning the thruster main physical mechanisms and performance. Therefore, this is the case of thrusters in which the plasma currents induce fields that are much smaller than the external applied ones (as in gridded ion engines with magnetic field cusps, or $\boldsymbol{E}\times\boldsymbol{B}$ thrusters[72]), thrusters in which any self-induced field has only a minor impact on the working physics (e.g., in colloid thrusters), or thrusters in which the inductive effects of the plasma currents are less important that those of the external circuit (e.g., in pulsed arc thrusters). An electromagnetic characterization of the latter (still unexplored in the EP community) would, however, help evaluate the ES modeling limitations.

In this approximation, the magnetic induction field $\boldsymbol{B}(\boldsymbol{r}, t)$ is prescribed in both space and time and is not coupled with the plasma currents. Therefore, the PIC model for macro-particles is uniquely coupled with Poisson's equation for the electrostatic potential ϕ,

$$\epsilon_0\nabla^2\phi = e\left(n_e - \sum_s Z_s n_s\right), \tag{7}$$

where ϵ_0 is the vacuum dielectric constant; n_e is the electron number density; e is the elementary charge; and Z_s and n_s are, respectively, the charge number and the number density of the considered ion species. Therefore, at each time step, from the knowledge of the deposited number densities of electron and ion species, a Poisson's solver is employed to obtain the electric potential, and hence, the self-consistent electrostatic field $\boldsymbol{E}_{ES} = -\nabla\phi$. This is then interpolated from the PIC mesh nodes to the particles position to advance them in the following time step, as shown in Fig. 1.

Equation (7) is discretized with methods of varying complexity (in some cases, accounting for adaptive mesh refinement, AMR), from finite differences to finite volumes methods. The resulting linear system is solved with highly efficient sparse solvers embedded in software packages, employing either direct (e.g., MUMPS,[73] PARDISO,[74] PETSc,[75] SuperLU,[76]) or iterative methods (e.g, HYPRE,[77] PETSc[75]), with the latter being more computationally efficient in expensive 3D geometries. The assumed boundary conditions for ϕ are of periodic, Dirichlet, or Neumann type: the first are generally applied at specific periodic boundaries of reduced scale simulations (e.g., at the azimuthal boundaries of cylindrical geometries or at the periphery of a single ion beamlet simulation, extracted from a multi-aperture gridded thruster); the second are applied to boundary surfaces whose potential is known *a priori* (e.g., at the electrodes), while the third are used at either open boundaries (refer to Sec. IV B for more details) or at dielectric surfaces. In this latter case, knowing the local surface charge density σ_c accumulated on the surface and applying Gauss's law, the normal-to-surface component of the electric field is

$$\nabla\phi\cdot\mathbf{1}_n = -\frac{\sigma_c}{\epsilon_0}, \tag{8}$$

where $\boldsymbol{1}_n$ represents the unit vector pointing toward the plasma. The above equation holds true when the electric field inside the material is zero (e.g., for metals), while it is only approximate for dielectric materials.

Recent works[78] have also considered the effect of the relative permittivity ϵ_r of any considered dielectric material by solving the generalized version of Poisson's Eq. (7),

$$\nabla \cdot (\epsilon_r \nabla \phi) = -\frac{\rho_c}{\epsilon_0}, \tag{9}$$

in a extended domain that includes the wall material in order to correctly compute the electric field discontinuities at the plasma–dielectric interface.[79]

In the vast majority of ES PIC simulations existing in the literature, an easy-to-implement explicit scheme is used (refer to Sec. V C for alternative implicit schemes) so that the strong constraints presented in Sec. II exist on the grid spacing and time step resolution to avoid numerical instabilities, with the only difference that the CFL condition is now based on the fastest species, the electrons, i.e., $v_e \leq \Delta r/\Delta t$ (numerical issues arising when a significant fraction of electrons do not comply with this condition). The resulting computational cost can be huge, depending on the considered thrusters. For PAT thrusters, the plasma density peaks to 10^{22} m^{-3}, corresponding to a minimum Debye length $\lambda_{D,e} \approx O(10^{-7})$ m and hence to a time step $\Delta t \approx O(10^{-13})$ s (from CFL condition, having assumed an electron temperature of $\approx$ 10 eV). Since meaningful simulations should cover at least a few cm's domain size and a few μs's temporal evolution, approximately 10^5 cells per direction and 10^8 time steps are necessary. In the other ES thrusters ($\boldsymbol{E} \times \boldsymbol{B}$, GITs or CTs), the plasma density level is lower, with a typical maximum value around 10^{18} m^{-3}, yielding $\lambda_{D,e} \approx O(10^{-5})$ m and $\Delta t \approx O(10^{-11})$ s, respectively. When neutrals dynamics are simulated, the steady state is reached after fractions of ms so that a total of around 10^3 cells per direction and 10^7 time steps are generally required. For the above reasons, and especially in 3D simulations (with $N_{ppc} \approx O(10^2)$ particles per cell), it is therefore necessary to use supercomputers and High Performance Computing (HPC) techniques (see Sec. V B). Nevertheless, numerical tricks (e.g., enlarged vacuum permittivity and/or reduction of ion mass or thruster size scaling) are still used in many simulations to reduce the computational time (see Refs. 38, 39, and 80–85 for $\boldsymbol{E} \times \boldsymbol{B}$ thrusters and Refs. 86–88 for PATs).

In the following paragraphs, some peculiarities of the different ES thruster types are further discussed.

1. Pulsed Arc Thrusters

PATs are generally simulated by assuming a magnetic induction field $\boldsymbol{B} = \boldsymbol{B}(\boldsymbol{r}, t)$ that is not coupled with the plasma (hence, the validity of the electrostatic approximation). In VATs,[86,87] this is non-uniform in space but assumed to be constant in time, while in PPTs, it also varies with time.[88] In particular, it is obtained as a function of the current flowing in the external circuit between the capacitor plates and of the instantaneous position of the accelerated plasma beam packet, with the use of Biot–Savart's formulas.[88] Therefore, even for PPTs, no self-consistent solution of Ampère's law, accounting for the plasma currents, is generally considered, at least in PIC models. The neutral atoms transport, including ablation or evaporation, collisions, and surface-interaction (see Sec. III C for more information) is then described with a kinetic approach.[86,88] The use of complex mixtures of solid propellant materials leads to a large level of uncertainty in terms of the collisional input data (see Sec. V A), if available at all in the literature. Moreover, the production of multiply charged ions from different species induced by the high-voltage [for example chlorine and carbon ions for polytetrafluoroethylene (PTFE) used as propellant for PPT[88]] at very high densities leads to an obvious increase of the computational time, making it necessary to reduce the simulation cost with the usual numerical tricks cited above.[87]

2. Electro-spray thrusters

In these thrusters, the magnetic induction field is generally absent, $\boldsymbol{B} = \boldsymbol{0}$. Particle-based models are here employed to model the extraction of the charged particles through an accelerating grid aperture (or many of them to analyze beamlets coalescence). Regarding the formation of such charged particles/droplets from Taylor's cone, more fundamental studies based on molecular dynamic (MD) simulations are needed, like those reported in Refs. 89 and 90. These studies are particularly relevant as they can provide more precise injection conditions for particle-based models, which currently consider a thermal injection of ions/liquid droplets.

In this context, Narayanan *et al.*[91] modeled the transport of charged particles emitted from a source at one end of the computational domain expanding through an aperture positioned downstream and polarized at a negative voltage. The size of the aperture is two orders of magnitude larger than the emission source, and an AMR technique was implemented to reduce the computational cost. Zao *et al.*,[92] on the other hand, also simulated the droplet acceleration using a particle–particle method (where the droplets are modeled with spherical particles) and the electrostatic force between them using Coulomb's interaction. This method avoids the use of a mesh and hence the constraints associated with Poisson's equation resolution.

3. Gridded ion engines

In gridded ion engine (GIE) simulations, the magnetic induction field is either absent or assumed to be constant in time and prescribed in space, $\boldsymbol{B} = \boldsymbol{B}(\boldsymbol{r})$. Although simulations of very similar negative ion sources for neutral beam injection (NBI) for nuclear fusion reactors are abundant in the literature,[94–99] simulations covering the interior of gridded ion engines are not very common in the plasma propulsion community, although a few examples exist where the ion generation region (sometimes called "driver" region) is not self-consistently simulated[100] but accounted for as an effective "volumetric injection region." More commonly, GIE simulations assume given upstream plasma conditions (in terms of plasma density and electron temperature) and focus exclusively on the ion beam extraction and acceleration process. This is indeed fundamental for both the design of the extraction grids and for the estimation of their ion-induced sputtering levels and hence the ion thruster lifetime. Moreover, most times, a hybrid particle-fluid approach is used[93,101] (refer to Sec. IV A for a more detailed description), in

which the electron density is given by a simplified Boltzmann's relation with a fixed electron temperature (sometimes two electron populations are considered for the separated upstream and downstream plasma electrons), alleviating the constrains related to the electrons dynamics. Three-dimensional codes[8,93,102,103] are then capable of simulating realistic conditions, including a large number of grid apertures. They are now sufficiently mature to be used for the optimization and design of the accelerating grids (thickness, spacing, and grid voltages) minimizing ion impacts on the grids (see Ref. 8 for a more complete overview of the available tools). Figure 2 finally shows the results for the ion extraction, acceleration, and beamlets coalescence of a multi-aperture GIE, obtained with a hybrid PIC model, featuring fluid electrons and non-neutral regions between the grids and close to the exit plane (see Sec. IV A for more information on non-neutral hybrid models). Two different and orthogonal cross sections through the thruster center are shown.

4. $E \times B$ thrusters

In these thrusters, the magnetic induction field is prescribed and constant in time $\boldsymbol{B} = \boldsymbol{B}(\boldsymbol{r})$. Although hybrid PIC models with fluid electrons assume a particle description for the neutrals (as in Refs. 104–106), in fully kinetic simulations, the propellant gas generally follows a fluid description. It is modeled as a non-uniform background with given density and temperature conditions,[81,107–109] which are considered fixed in time, in order to reduce the computational time. Scaling of the thruster size, and prescribing the neutral density profile[39,110–112] or the source term profile[113] are commonly used techniques and permit the study of specific processes and to assess their influence on the thruster operations. Even if these studies have shown limited conclusions, they offer opportunities to make parametric analyses minimizing the computational cost, before gradually increasing the complexity including the coupling between different physical phenomena. A typical example is the study of the electron cyclotron drift instability (ECDI) and its role on the so-called anomalous electron transport. This kinetic instability[114] takes place in the azimuthal $\boldsymbol{E} \times \boldsymbol{B}$ direction of a HT and is due to the different velocities between magnetized electrons (azimuthally drifting under the action of the axial electric and radial magnetic fields) and ions, that, on the other hand remain unmagnetized and are accelerated almost purely in the axial direction. One-dimensional azimuthal,[115–119] two-dimensional axial-azimuthal,[81,107,108,111,114,115,118,120] and two-dimensional radial-azimuthal[110–112,121–124] models have been developed. Simulation results show the existence of a coherent structure in the azimuthal direction with resonances at discrete values

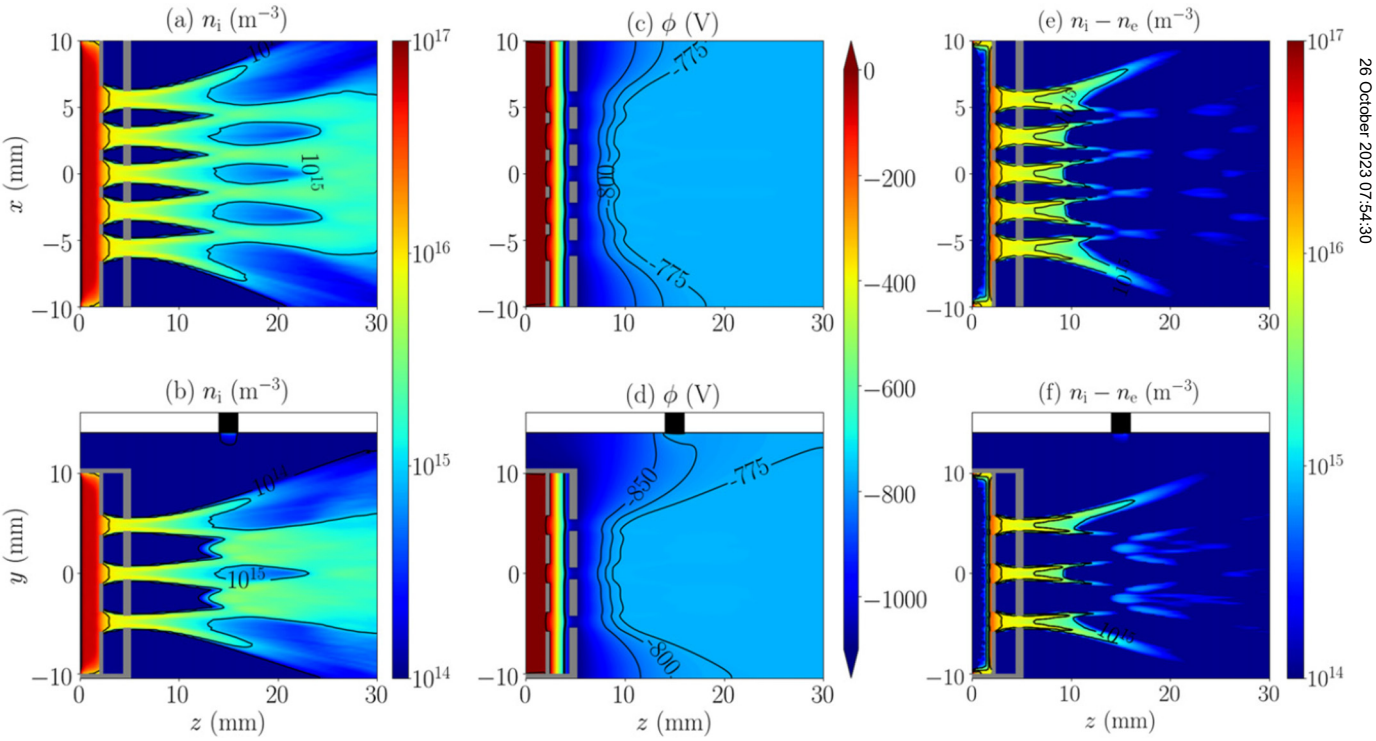

FIG. 2. Three dimensional simulation of beamlets extraction, acceleration and coalescence in a GIE with 19 apertures, obtained with a hybrid model. Subplots [(a), (c), and (e)] and [(b), (d), and (f)] refer to two orthogonal cross sections through the thruster center and, namely, to the x, z plane and to the y, z plane (refer to Fig. 7 of Ref. 93). The neutralizer, shown by a black rectangle in subplots (b), (d), and (f), is located on the y–z cross section. Reproduced with permission from Perales *et al.*, Plasma Sources Sci. Technol. **30**, 105023 (2021). Copyright 2021 IOP Publishing Ltd.

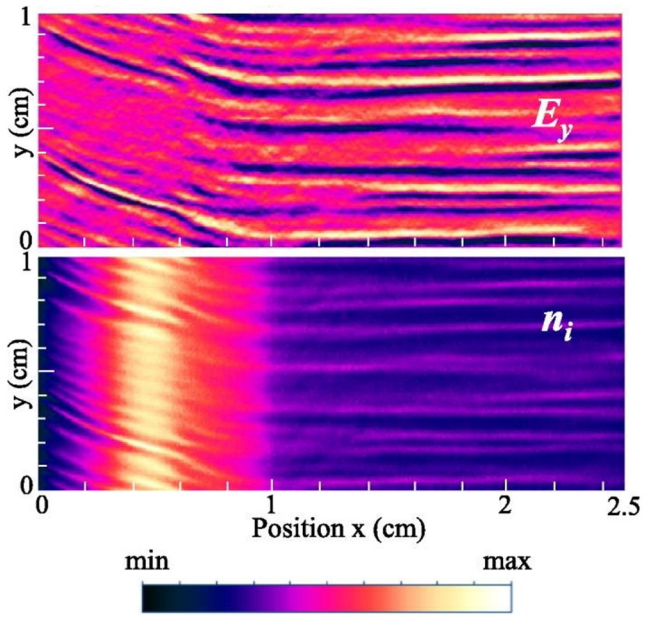

FIG. 3. Axial *x*–azimuthal *y* distributions of the azimuthal electric field E_y and of the ion density n_i at a given time step. The minimum and maximum values for E_y are -5×10^4 and 5×10^4 V/m, respectively, and for n_i are 0 and 5×10^{17} m^{-3}. Adapted with permission from Boeuf *et al.*, Phys. Plasmas **25**, 061204 (2018). Copyright 2018 AIP Publishing LLC.

characterized by a wavelength in the order of the millimeter and a frequency in the MHz range (as illustrated in Fig. 3). The saturation of the instability is visible in ES PIC simulations with the deformation and broadening of the electron and ion velocity distribution functions. The origin of the transition to the non-linear regime is still in debate (see Ref. 125 for more details). 2D radial-azimuthal simulations have also revealed the existence of a longer wavelength instability between the dielectric walls along the magnetic field line, called Modified Two-Stream Instability (MTSI), and belonging to the same family of ECDI in the limit of wavenumber parallel to the magnetic field. These 2D radial-azimuthal models have also included the secondary electron emission (SEE) induced by plasma electrons colliding with the walls to study the mutual coupling between the ECDI and SEE.[111,112] Recently, kinetic models have detected an ion–ion two stream instability (IITSI) due to multiply charged ions[126] and a current carrying ion-acoustic instability from the cathode.[127] Lastly, three-dimensional ES PIC simulations of a HT have been performed under simplified plasma conditions.[39,128–131] Preliminary analyses have shown the existence of the ECDI but its fluctuations amplitude is typically one order of magnitude smaller than in 2D simulations, close to the estimations measured by Thomson scattering diagnostics.[132]

Finally, the community has been interested in recent years in the verification aspect of the numerical techniques used for $\boldsymbol{E} \times \boldsymbol{B}$ thrusters, through the LANDMARK project.[133] This aspect is essential to demonstrate the accuracy of the simulations. These benchmarks, reproduced by seven research groups worldwide, have also allowed for a comparative evaluation of the PIC algorithms efficiency (type of parallelization, Poisson's solvers, explicit vs implicit algorithms, CPU compared to GPU architectures, etc.[107,122]). Figure 4 illustrates a comparison of the two-dimensional radial-azimuthal simulation results obtained by seven different ES PIC models, showing their remarkable agreement in capturing the time evolution of the MTSI and ECDI instabilities.

B. Electromagnetic PIC

Modeling of EM thruster discharges frequently needs to take into account electromagnetic effects. Above all, an adequate

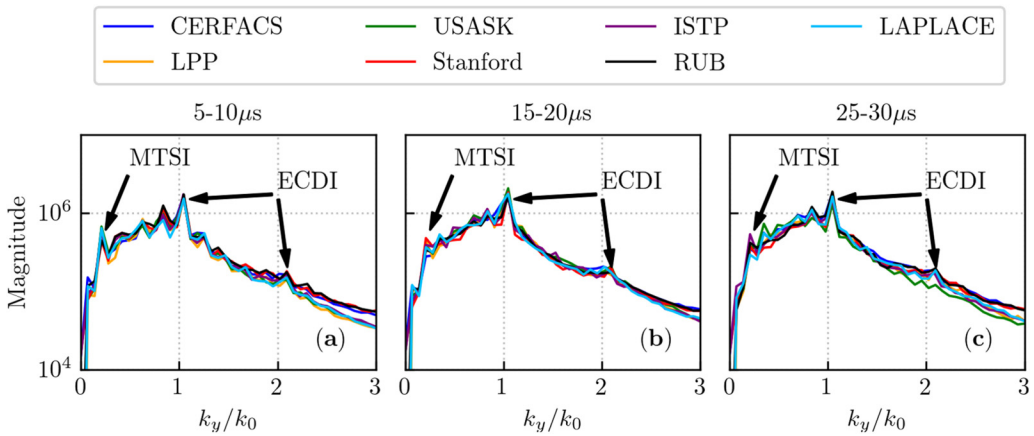

FIG. 4. 1D azimuthal FFT of the azimuthal electric field Ey, averaged over all radial positions and over three temporal intervals obtained by seven ES PIC models implemented by different research groups. MTSI and ECDI resonances are indicated by arrows. Reproduced with permission from Villafana *et al.*, Plasma Sources Sci. Technol. **30**, 075002 (2021). Copyright 2021 IOP Publishing Ltd.

self-consistent description of the plasma and EM field dynamics is vital for obtaining accurate power absorption profiles. It is also important to be capable of predicting the specific energy acquired per electron from the electric field in the context of electron energization, i.e., production of electrons with energy above the ionization threshold.[134–136] In order to compute the power absorption and capture the electron energization mechanisms, non-linear effects, such as the generation of higher harmonics, parametric decay instabilities, non-linear wave–particle interaction including particle trapping effects, and non-linear skin-effect (see, e.g., Refs. 137–142) can be important. The corresponding description requires evolving electromagnetic fields and particle orbits in the time domain, which is naturally contained in the PIC algorithm. The power absorption profiles are intimately related to the profiles of plasma density, electrostatic potential, electron temperature, and ionization rate, which affect other properties of the discharge of immediate relevance to propulsion applications, such as electron confinement and transport, plume dynamics, thrust, and many others. This necessitates fully self-consistent EM PIC simulations. However, it is notoriously difficult to conduct EM PIC simulations and thus to obtain the power absorption profiles self-consistently. This is why most of the modern thruster-related modeling studies resort to drastic simplifications. Although it is true that one can get insights into some of the thruster-related phenomena using such simplifying assumptions, a consistent and comprehensive understanding followed by quantitative estimates and optimizations can result only when the EM field evolution is appropriately treated.

While, as in any PIC, particle orbits obey Eq. (3), electromagnetic fields in EM PIC algorithms must be evolved in time using Maxwell's equations, which can be represented as follows:

$$\frac{\partial \boldsymbol{B}}{\partial t} = -\nabla \times \boldsymbol{E}, \tag{10}$$

$$\frac{\partial \boldsymbol{E}}{\partial t} = c^2 \nabla \times \boldsymbol{B} - \frac{1}{\varepsilon_0}(\boldsymbol{j}_{\text{ext}} + \boldsymbol{j}), \tag{11}$$

where c is the speed of light in vacuum and the current density flowing in external coils or antennas, $\boldsymbol{j}_{\text{ext}}$, is considered separately from the plasma current $\boldsymbol{j}$. When the charge conservation in its discrete form is ensured by the algorithm,[67,70,143,144] Gauss's law is an involution[68] and is satisfied automatically at later times if it held initially. Otherwise, the electric field has to be regularly adjusted to force its potential part to match Gauss's law,[145] in order to avoid spurious effects. From Eq. (10), one can see that the solenoidal nature of the magnetic field is another involution and that $\nabla \cdot \boldsymbol{B} = 0$ is satisfied always, if it was satisfied initially.

Most often, Eqs. (10) and (11) are discretized in time using the explicit leapfrog scheme, and in space using finite differencing, with fields arranged according to the Yee scheme.[146] This results in the classical Finite-Difference Time-Domain (FDTD) algorithm,[146–148] which is relatively simple to implement. Boundary conditions stem either from the physical properties of materials bounding the computatitonal domain (e.g., requiring the tangential electric field to vanish at a conducting surface) or from the "absorbing boundary condition" (ABC) emulating an open boundary. If there are materials (e.g., reflecting conducting walls) inside the computational domain, they can naturally govern the field behavior via macroscopic Maxwell's equations with the appropriate material properties (permittivity, permeability, and conductivity). The ABC should combine both the incident wave powering the discharge and the scattered electromagnetic fields leaving the discharge with the smallest reflection possible, which can be realized at the computational domain boundary using the Mur method[149] or using the "perfectly matched layer" (PML) technique, which artificially changes material properties in a thin layer close to the boundary so that the outgoing radiation is heavily damped there[150] and requires a specification of the incident wave before that layer. In contrast to the latter technique, in Mur's method one assumes that the scattered electromagnetic fields leaving the discharge can be approximated by a one-dimensional electromagnetic wave, so that the fields are governed by the corresponding outgoing wave equation. Noting that the scattered electromagnetic fields are equal to the difference between the total and incident wave fields with a prescribed temporal and spatial dependence, one obtains the sought boundary condition for the total electromagnetic fields. If the outgoing wave propagates in the radial direction of a cylindrical geometry, the wave is not planar, so that the corresponding boundary condition has to account for that.[151] Such a method has been used previously in electromagnetic fluid simulations[152,153] and more recently in electromagnetic PIC simulations.[70] Another way to model the EM power input to a plasma discharge is to prescribe a time-dependent external current inside the computational domain, which is common to ICP discharges modeling.[154]

As noted in Sec. II, the FDTD algorithm is stable only if the CFL criterion is satisfied. Since the phase velocity of the EM waves with short wavelengths asymptotes to c, for such waves, the CFL condition demands that the time needed by a vacuum light wave to cross a grid cell be greater than the time step, resulting in very long simulation times. Often, EM thrusters are also characterized by a relatively large plasma density ($n_e \geq 10^{18}\,\text{m}^{-3}$), which leads to small values of the plasma period $\tau_{p,e} = 2\pi/\omega_{p,e}$. Since EM waves with very long wavelengths propagating in the plasma are similar to the electrostatic plasma waves, another restriction on the time step is similar to the ES PIC and requires to resolve the plasma period in time. Therefore, a stable EM PIC simulation based on the explicit algorithm should have a time step satisfying both criteria. In contrast to the explicit ES PIC algorithm, where the cell size is restricted by the need to mitigate the finite-grid-instability (FGI)[155] that demands that the cell size be smaller than the Debye length, the corresponding instability is much less studied for the explicit EM PIC. The cases considered do not include warm plasma effects,[156] which can significantly change the FGI dispersion relation. Based on the similarity of the explicit FDTD EM PIC algorithm to the energy-conserving algorithm[157] in the limit of the vanishing time step, one may speculate that at least the electrostatic FGI present in the EM PIC should exhibit the same properties as the well-studied FGI in the energy-conserving ES PIC,[155] i.e., be stable in warm plasmas for the cell size well exceeding the Debye length. Nevertheless, some authors state that the cell size should not be greater than the Debye length for the stability reasons.[158,159] Another reason to resolve the Debye length is that it is the inherent spatial scale of important physical phenomena, such as plasma

sheath, double layer, or various short-wavelength instabilities. The mentioned numerical constraints can be very restrictive in simulations of dense plasmas, especially if multiple dimensions are desired. This is why only recently and for miniaturized configurations, some fully self-consistent EM PIC modeling attempts[160–164] based on the explicit algorithm have been reported in the low-temperature plasma community, of which only very few targeted thruster plasmas. In the majority of such cases, a conducive feature of the EM PIC method was exploited, i.e., the fact that the leapfrog algorithm evolving the EM fields did not involve matrix inversions and could be parallelized very efficiently.

In addition to using advanced HPC techniques (see V B for more details), there are other options for making PIC simulations of EM thruster discharges tractable, by using time integration algorithms less sensitive to the time step and/or to the cell size. Such algorithms can be classified as follows: (i) numerical algorithms with an instability criterion less restrictive compared to that of the explicit one, (ii) modification of the model itself (either through a dimensionality reduction by replacing the kinetic description with a fluid one or by removing fine spatial or temporal scales in the model with an applicable physics approximation), and (iii) artificial decoupling of the EM wave powering the discharge from the plasma via neglecting the plasma current in Ampère's law, which makes the electromagnetic field description lose its self-consistency.

An algorithm belonging to (i) is the semi-Lagrangian Constrained Interpolation Profile (CIP) algorithm[165] employed in Refs. 166 and 167. Being explicit, it is relatively simple to implement and does not incur a heavy computational burden. Additionally, it has good numerical dissipation and dispersion properties. Further examples are the energy-conserving implicit or semi-implicit PIC methods (see Sec. V C 2 for more details). Such methods seem to be surprisingly rarely employed in EM PIC modeling of plasma propulsion devices. However, the recently developed implicit energy-conserving PIC (ECPIC), or the semi-implicit PIC (ECSIM) methods demonstrate very attractive properties when applied to EM PIC modeling of technological plasmas featuring a large ratio between the system size and the Debye length.[70,154] Yet another variant of (i) is to remove the nonlinear coupling between the driving azimuthal electric field and the plasma by assuming a single harmonic for the electric field at the driving frequency. The electric field is provided then by the Helmholtz equation in the frequency domain, which is elliptic and does not produce numerical problems. Such a technique is typically used for ICP thrusters [see Sec. III B 1, Eq. (12)].

Methods in (ii) are also versatile and a common example is to replace the kinetic treatment with a fluid model for one[21,27] or all species,[168–171] resulting in a hybrid scheme. Examples of eliminating fast time scales are the use of the drift-diffusion approximation instead of the full momentum balance equation for the electrons, or obviating radiative phenomena through Darwin's approximation by dropping the solenoidal part of the displacement current in Ampère's law. The latter should be applicable to discharges driven at relatively low frequencies so that the EM wavelength is much larger than the device size, which holds for typical ICP and Helicon thrusters. By removing radiative phenomena, such an algorithm would also get rid of the corresponding CFL condition related to light waves (note that the one linked to particle motion still remains), but the conventional explicit Darwin's algorithm is unconditionally unstable[172] and must be used only in an implicit form.[68,173–175] It is suggested that Darwin's algorithm can also mitigate the problem of accumulated radiative noise,[157] which might potentially be dangerous for fully electromagnetic energy-conserving PIC algorithms.[68,175]

Finally, algorithms belonging to (iii) consist in solving for the electric and magnetic fields driven by an external source separately (usually, with the FDTD method), while neglecting the plasma-generated fields, which is justified if $\omega \gg \omega_{p,e}$. In this case, the power absorbed by the plasma is calculated from the change of the kinetic energy of plasma particles in response to the vacuum solution for the EM fields. The amplitude of the vacuum microwave electric field is then adjusted to match a prescribed value. This non-self-consistent approach is typically employed for PIC simulations of MW thrusters (see Sec. III B 3).

The following thruster types have been modeled most using EM PIC codes:

1. Inductively coupled thrusters

Thrusters based on inductively coupled plasma discharges are among the oldest EP technologies[176] remaining in active use nowadays.[8] They typically feature a planar coil with an RF current, which creates a time-dependent magnetic field with both radial and axial components, inducing an azimuthal electric field sustaining the plasma discharge. This "inductive heating" mode (also known as the H heating mode) occurs at relatively large powers, when the skin depth is smaller than the discharge size. At low powers, the discharge is operated in the "capacitive heating" mode (also known as the E heating mode), which is powered by the radial and axial capacitive electric fields produced by the coil. In the absence of a stationary magnetic field, the thrust is generated by ions extracted by electrostatic grids, e.g., as in radio frequency ion thrusters (RITs).

The azimuthal electric field drives a current, which, when combined with the magnetic field, generates the second harmonic of the radial and azimuthal current components via the Lorentz force.[139,177,178] The latter, in turn, produces the second harmonic of the azimuthal magnetic field. Such a non-linear coupling process can be significant at low RF frequencies and can generate ever higher harmonics of the magnetic field.[138] In general, the induced magnetic field can affect electron orbits, which is important when kinetic and non-local phenomena play out.[179,180] However, under typical conditions, only the second harmonic of the azimuthal magnetic field (as well as of the radial and azimuthal currents) matters, which justifies the common assumption that it is sufficient to describe only the azimuthal component of the electric field at the fundamental frequency. This fundamental harmonic of the inductively produced electric field dominates the power absorption. To avoid the stiff differential equation in the time domain, a popular workaround adopted in ICP discharges modeling for plasma processing applications[181] is to solve for the fundamental harmonic of the azimuthal electric field in the frequency domain using the Helmholtz's equation[23,182]

$$\left(\nabla^2 + \mu_0 \varepsilon_0 \omega^2\right) \tilde{E}_\theta = i\omega\mu_0 (\tilde{j}_{\mathrm{ext},\theta} + \tilde{j}_\theta), \tag{12}$$

where $\tilde{E}_\theta$ is the complex azimuthal component of the electric field, i is the imaginary unit, while $\tilde{j}_{\mathrm{ext},\theta}$ and $\tilde{j}_\theta$ are the azimuthal complex amplitudes of the external coil and plasma electron current densities (the ion contribution can be ignored owing to the low mobility of ions). Assuming that the fixed phase of $\tilde{j}_{\mathrm{ext},\theta}$ is zero (because this phase can be treated as a common phase offset), $\tilde{j}_\theta$ at the grid point g can be estimated as

$$\tilde{j}_{g,\theta} = \left| \frac{\sum_p q_p w_p \tilde{v}_{p,\theta} W_j(\boldsymbol{r}_g - \boldsymbol{r}_p)}{V_g} \right| e^{i\Delta\psi}, \tag{13}$$

where $\Delta\psi$ is the phase difference between $\tilde{j}_{\mathrm{ext},\theta}$ and $\tilde{j}_\theta$. $\Delta\psi$ can be calculated by performing the discrete Fourier transform of j_θ, and calculating the phase of the corresponding complex amplitude at the fundamental harmonic.

In case $\tilde{j}_{\mathrm{ext},\theta}$ is non-zero only at the boundary or outside of the computational domain, its effects are imposed as a boundary condition on $\tilde{E}_\theta$ as follows. In the considered case, $\tilde{E}_\theta(\boldsymbol{r}) = -i\omega\tilde{A}_\theta(\boldsymbol{r})$, where the vector potential can be calculated from Biot–Savart's law[19,20,183] (assuming that the electromagnetic radiation wavelength is much larger than the distance from the coil to the boundary of the computational domain),

$$\tilde{A}_\theta(\boldsymbol{r}) = \frac{\mu_0}{4\pi} \left[\int d^3r' \frac{(\tilde{\boldsymbol{j}}_{\mathrm{ext}}(\boldsymbol{r}') + \tilde{\boldsymbol{j}}(\boldsymbol{r}'))}{|\boldsymbol{r} - \boldsymbol{r}'|} \right]_\theta. \tag{14}$$

In the case of materials with magnetic properties, the corresponding internal magnetization currents need also to be included in the above equation. For a cylindrical geometry, the boundary condition for $\tilde{E}_\theta$ based on this integral can be evaluated using simplified analytical formulas given in Refs. 184 and 185. Although, in general, the integral is computationally expensive, it must be computed only at the boundary. Note also that $\tilde{E}_\theta(\boldsymbol{r})$ must be updated only once per RF period.[20] Once $E_\theta(\boldsymbol{r}, t)$ has been computed, the induced magnetic field can be directly obtained from Faraday's law, Eq. (10). Finally, the radial and axial electric field components governing the ambipolar plasma transport on the ion time scale are obtained electrostatically from Poisson's equation. The described approach takes into account only the fundamental harmonic of the azimuthal electric field, and the corresponding amplitude is updated every time interval of the order of the RF period,[20] which is much bigger than the time step and might exclude fast transient time effects. However, if no such effects are expected, the method is robust and includes important kinetic and non-local dynamics, which are significant at the low pressure regimes of these thrusters.[19] That is why the described method has been used in numerous modeling studies.[19,20,182,183,186,187] In particular, Refs. 20 and 183 reported a massive parallelization of such a model on CPUs, which allowed for 3D simulations of RIT thrusters with complex geometries.

Finally, it is worth mentioning that there is a number of numerical studies for the negative ion source-related ICP discharges simulating them with fully electromagnetic PIC algorithms, either of the explicit[188–191] or of the implicit energy-conserving[154] kind. The latter holds great promise for modeling high-density plasmas (see Sec. VC 2), which are abundant in the field of electric propulsion.

2. Helicon plasma thrusters

Helicon discharges have a number of features, which make them attractive for EP applications.[24,192] They have high ionization[193] and power conversion efficiencies,[194] the latter ensured by the absorption of the helicon and the Trivelpiece-Gould (TG) modes excited in a plasma with a relatively small magnetic field,[195,196] sustained by either a solenoid or a permanent magnet. The excitation frequency lies in the range $\omega_{c,i} \ll \omega \ll \omega_{c,e}$, which translates to MHz and, therefore, does not require complex power generators. Conceptually, a helicon discharge can be viewed as an ICP discharge enhanced with a DC magnetic field. Therefore, they share some of the features inherent to ICPs, such as the electrodeless configuration and the E–H heating mode transition with increasing power. However, they also feature unique physics when the power is further increased, the helicon and TG modes are excited, and the discharge goes into the W heating mode dominated by electrons absorbing power from the corresponding modes.[197] The thrust in such systems can be generated either with a system of electrostatic extracting grids or with a magnetic nozzle (where ions are accelerated by the ambipolar field sustained by the plasma and by a double layer-related potential drop).

Modeling the corresponding physics would require EM PIC simulations (or simulations with a Darwin PIC code, considering that helicon discharges are operated at low frequencies). The excitation of helicon and TG modes, their absorption in the plasma, and the related non-linear physics, such as the mode conversion, parametric instabilities, and non-linear Landau damping are of particular interest in this context.[141,197–201] The power absorption and plasma ionization profiles are intertwined with many other important phenomena taking place in helicon plasmas, such as the formation of the plasma density profiles,[202] as well as the triggering and non-linear evolution of various instabilities, leading to the anomalous electron transport across the magnetic field lines.[197] Due to the low collisionality, the Electron Energy Distribution Function (EEDF) is often non-Maxwellian, and the mean free path can be comparable to the system size. Hence, the corresponding simulations must be self-consistent, kinetic, and non-local so that PIC simulations suit ideally. Unfortunately, due to the high plasma density generated in helicon plasmas in this regime (up to $10^{19}\,\mathrm{m}^{-3}$),[203] the corresponding Debye length is small, and due to the limitation on the cell size and the time step for the conventional explicit PIC algorithm, the corresponding computational cost is high. This is why fully self-consistent EM PIC simulations of helicon discharges are extremely scarce in the literature.[163,164] Reference 163 considered the H–W heating mode transition as both the magnetic field and power were varied. The results indicated that the common assumption that in the W regime the power absorption is dominated by the TG modes was not correct for the considered discharge. Instead, the power was absorbed by electrons predominantly in the plasma bulk where the helicon modes reside. This unexpected finding stressed the importance of using self-consistent EM PIC models. Reference 164 also suggested that the helicon modes can influence power absorption. Virtually all other PIC studies of helicon discharges available in the literature consider the low-power regimes, where plasma density is not very large (up to $10^{17}\,\mathrm{m}^{-3}$) so that the power absorption dynamics is similar to the H regime in ICP devices and can be

modeled following the approach of Sec. III B 1, focusing on other aspects of the discharge physics demanding a kinetic and non-local description in the presence of a DC magnetic field (e.g., Refs. 202 and 204–206).

3. MW-driven ECR plasma thrusters

The microwave (MW) heating mechanism for electric thrusters is most often associated with the electron cyclotron resonance (ECR) configuration having a DC magnetic field to increase the energy transfer efficiency from the wave to the plasma. The reason is that, at low pressures, the plasma resonance in an unmagnetized plasma[208] is too weak. In contrast, a magnetic field leads to the possibility of having a resonance at the cyclotron frequency or its harmonics and can confine electrons (typically, in combination with the electrostatic potential) so that they pass through that resonance many times, gaining more energy from the electric field and increasing the power absorption efficiency. Due to the thermal motion of the electrons, the resonance condition acquires a Doppler shift. For a population of electrons having a distribution in velocity space, the resonance location becomes Doppler-broadened.[209] The energy absorption via ECR heating occurs orthogonally to the magnetic field, which results in a strongly anisotropic EEDF. In addition, close to the resonance, the electric field amplitude becomes large, and in a warm plasma, Langmuir and/or Bernstein waves can be excited.[210] These waves carry the energy from the resonance and can deposit it somewhere else in the plasma through their own damping mechanisms. Such a mode conversion process can be linear when the secondary waves are excited at the same frequency as that of the driving wave, or it can be non-linear when different harmonics are generated, which can result in turbulence. Similar to helicon thrusters discussed in Sec. III B 2, the thrust in MW-driven ECR thrusters is typically produced using a system of electrostatic grids or with a magnetic nozzle. Evidently, most of the mentioned phenomena should be treated in EM PIC simulations self-consistently, kinetically and non-locally.

The first works, which modeled MW-ECR ion sources with one-dimensional[160] and three-dimensional[161] explicit fully EM PIC simulations, date back to the 1990s. They considered the propagation of the pumping wave and the power absorption profiles in 1D[160] and 3D,[161] respectively. The latter was possible, thanks to the HPC techniques available at that time. The corresponding PIC models described the self-consistent evolution of the plasma and EM fields in the time domain. Self-consistent coupled integration of the particle and field equations in the time domain in the propulsion-related PIC simulations of ECR discharges have recently started to emerge,[165–167,211] where the CIP algorithm was used. This novel explicit semi-Lagrangian algorithm, potentially enabling large time steps, has been exploited to conduct 1D and 2D simulations for an ECR thruster with a magnetic nozzle. In particular, in Ref. 167, it was explicitly demonstrated that the electron power absorption indeed occurs in the Doppler-broadened resonance zone, where electrons gain perpendicular energy. Surprisingly, a second absorption peak far away from the ECR region, was observed in the electron mean perpendicular energy. This was attributed to the existence of a large population of electrons trapped by the mirror effect on the back-plate side and by the electrostatic potential on the downstream side of the ECR region. Also, it was found that the EEDF is anisotropic in velocity space[167] (which could be potentially important for certain instabilities), with the resulting high energy electron population playing a major role in ionization, despite its relatively low number density. It was finally noted that the magnetic field can influence significantly the ion properties.

Another set of works[26,207,212–219] focused on numerical modeling of ECR discharges with a grid extraction system. The aforementioned simplified and non-self-consistent approach was considered, with the MW fields computed from Eqs. (10) and (11), but without taking into account the plasma contribution, i.e., with $\boldsymbol{j} = 0$. The power absorption profile is calculated by integrating the plasma motion in the EM fields of the wave thus obtaining $\boldsymbol{j} \cdot \boldsymbol{E}$. The wave amplitude is adjusted according to the power absorbed by the plasma on the wave path, but the wave structure remains the same as in vacuum. From the power absorption, an ionization rate profile is obtained, which determines where and how many new electron–ion pairs have to be seeded in an electrostatic PIC (i.e., solving only for Poisson's equation). Such an approach is not justified for dense or over-dense plasmas, where plasma frequency is comparable to or larger than the driving frequency, so that by dropping the plasma influence one can miss important cutoff or resonance locations. For example, Fig. 5 shows the results for such a modeling approach, as described in Ref. 207 for an ECR discharge driven at 4.25 GHz. Although the electron density is smaller than the critical density, which is approximately $2.24 \times 10^{17}\ \mathrm{m}^{-3}$ for this frequency, in some locations, the electron density becomes comparable to it. However, if the study focuses on other effects not related to the EM wave propagation, power absorption, and related electron heating, then such an approximation may be reasonable. It can be seen in Fig. 5 that both the electron temperature and the ionization rate peak close to the ECR contour indicated by the dashed curve, a fact expected for the considered simplification, which could not hold true if a more general model is used (accounting for the plasma contribution). Finally, the electron density profile is much broader than that of the ionization rate, which indicates some diffusion across the magnetic field; its arc-shaped boundary, nevertheless, suggests that electrons are well confined by the magnetic field.

C. Plasma–wall interaction

Plasma–wall interaction is a fundamental process in almost all the EP devices characterized by a high surface-to-volume ratio. Both electrons and ions can heat the walls inducing very high wall temperatures in certain regions of the discharge. Many experimental evidence[220–223] has shown how the thruster wall material has a great impact on thruster performances and discharge parameters. Particle models are well suited for simulating the non-neutral character of the plasma–wall transition region. The different topics related to plasma–wall interaction and captured by particle-based models can be classified in the following categories: (i) electron deviation from a Maxwellian distribution due to sheath effects, (ii) electron-induced secondary electron emission, (iii) ion sputtering, (iv) ion recombination at the walls, and (v) gas–wall interaction. All these aspects are presented below.

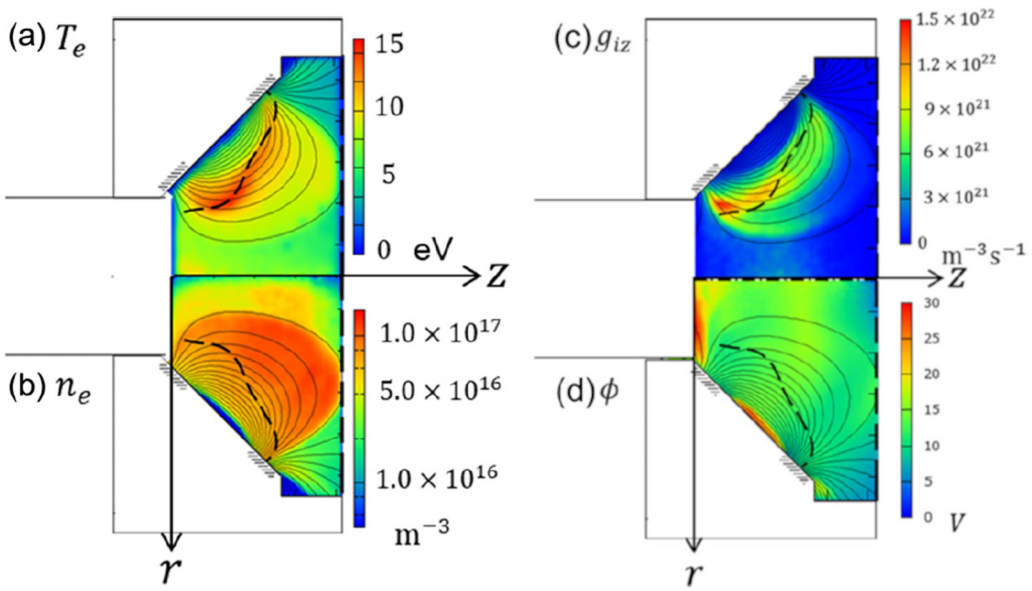

FIG. 5. The (r, z) profiles of electron temperature, electron density, ionization rate, and electrostatic potential in the μ10 ECR thruster. Reproduced with permission from Yamashita *et al.*, Phys. Plasmas **26**, 073510 (2019), Copyright 2019 AIP Publishing LLC.

1. Sheath models

Recently, a renewed interest in the study of electron kinetics has been highlighted with a series of papers[224–227] studying the dynamics perpendicular to the lateral walls in HT discharges by means of a revised version of the PIC model of Taccogna *et al.*[228,229] Since the low collisionality is insufficient to replenish the high-velocity electrons collected at the walls, a significant depletion of the parallel-to-magnetic field electron velocity distribution function (VDF) is detected that has several important implications on some global quantities: sheath potential drop, wall collision frequency, and particle and power wall losses.[230] In particular, the VDF depletion permits to have quite lower electron particle and energy fluxes reaching the wall, compared to the Maxwellian population, reducing the impact of the near-wall conductivity on the total anomalous electron cross field transport. Moreover, the low electron collisionality introduces an anisotropy between perpendicular and parallel to B field electron temperatures, and asymmetries between the inner and outer walls in HT discharges. However, it has been shown that the magnetic field inclination relative to the lateral walls affects the transfer between radial and axial electron velocity components and reduces these effects.

2. Secondary electron emission models

The secondary electron emission (SEE) is mainly caused by electron impacts (with a negligible influence of ion impacts) when the lateral surfaces of the thruster are made of a dielectric material, which is a quite common case. Ion-induced SEE[231] may be more important for metallic surface. Electron-induced SEE has an important effect on the lateral potential sheath drop, the wall energy losses, the absorption power and the electron cross field transport (near-wall conductivity) and it is generally coupled with instabilities.[232] Due to the typical fast timescale characterizing the electron-material process (10^{-13} s), the electron wall emission implementation in PIC models can be done by a phenomenological approach. In recent years, different SEE algorithms have been proposed that are characterized by the electron emission yield (EEY) $\sigma(E_p, \theta_p)$ and the spectrum of emission energy $f_E(E_p, \theta_p)$ and angle $f_\theta(E_p, \theta_p)$ of secondary electrons, all functions of the impact energy E_p and angle θ_p of the primary electron: the linear and power law,[221,233] the modified power law,[234] the modified Vaughan model,[235] the Sombrin model,[236] the Furman–Pivi model[237] and models using expressions obtained from machine learning software.[238] However, there is still lack of data related to the EEY, and especially in the low-energy range $E_p < 30$ eV (corresponding to the impact energy of a large fraction of primary electrons due to the decelerating effect of the sheath electric field), owing to experimental difficulties to measure it. The most accurate measurements[239–242] (see Fig. 6) and theoretical works[243] suggest a non-zero EEY at zero impact energy $\sigma(E_p = 0) > 0.3$–0.4 with even an increasing EEY for decreasing energy E_p lower than 10 eV for most common dielectric materials relevant to EP. This behavior is not reproducible with linear, power or Vaughan laws and can be ascribed to the different behavior of the EEY of the three populations of emitted secondary electrons: elastically and inelastically backscattered, and true secondaries (electrons belonging to the wall material). Some numerical works[244] have shown how the macroscopic behavior can change according to the value assumed by the EEY at $E_p = 0$. Finally, backscattering electrons have a memory effect of the impact energy and angle:[245,246] while true secondaries

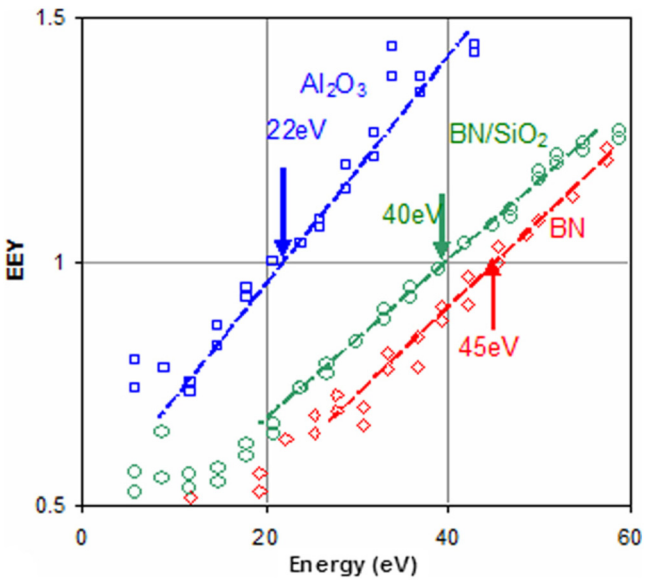

FIG. 6. Electron-emission yield for pristine Al_2O_3, BN, and $BNSiO_2$. The lines corresponds to linear laws. The arrows show the first crossover energy. Reproduced with permission from Tondu *et al.*, J. Appl. Phys. **110**, 093301 (2011). Copyright 2011 American Institute of Physics.

have an isotropic emission (cosine-Lambertian distribution[247,248]), backscattered electrons show a double-lobe angular emission[42,246,249] corresponding to the almost incident and specular angles (see Fig. 7). This can have important consequences on the non-local character (electrons emitted from one wall are often those impacting on the opposite wall) and on the realistic estimation of the near-wall contribution on the electron anomalous mobility.

3. Ion-wall interaction models

The lifetime of different electric thrusters is limited by the large erosion of the chamber walls due to ion sputtering: in magnetic unshielded configurations, the integrated ion flux to the walls can represent up to 40% of the total ion production (integrated ionization source term over the thruster volume). Therefore, a reliable and precise simulation of the discharge wall erosion would be beneficial to reduce long and expensive life tests in vacuum chambers. These simulations require to know both the ion velocity distribution function at wall impact (this can be obtained using a particle model at least for ions) and the sputtering yield function of the wall material in terms of impact energy and angle (for a given impacting ion species). Computational efforts have successfully reproduced general erosion rate trends,[250] but models are not yet fully predictive or capable of reproducing experimentally observed surface features. In particular, the low ion energy sputtering yield is very challenging to measure precisely, the connection between erosion and performance degradation requires further study, and an explanation of the ubiquitous presence of the so-called "anomalous" erosion ridges in HT configurations remains elusive.[251] High-fidelity plasma models have yet to be integrated with sophisticated material and sputtering models. Finally, a complete assessment of the erosion effects requires to simulate the re-deposition rates and, therefore, to follow the sputtered atoms trajectories. This is generally less expensive computationally than assessing the ion sputtering profiles, as these neutrals trajectories are weakly coupled with the plasma and can be studied using simplified approaches, like the view factor models.[252]

When ions hit the thruster walls, apart from possibly causing the emission of sputtered atoms, they most likely lose their kinetic

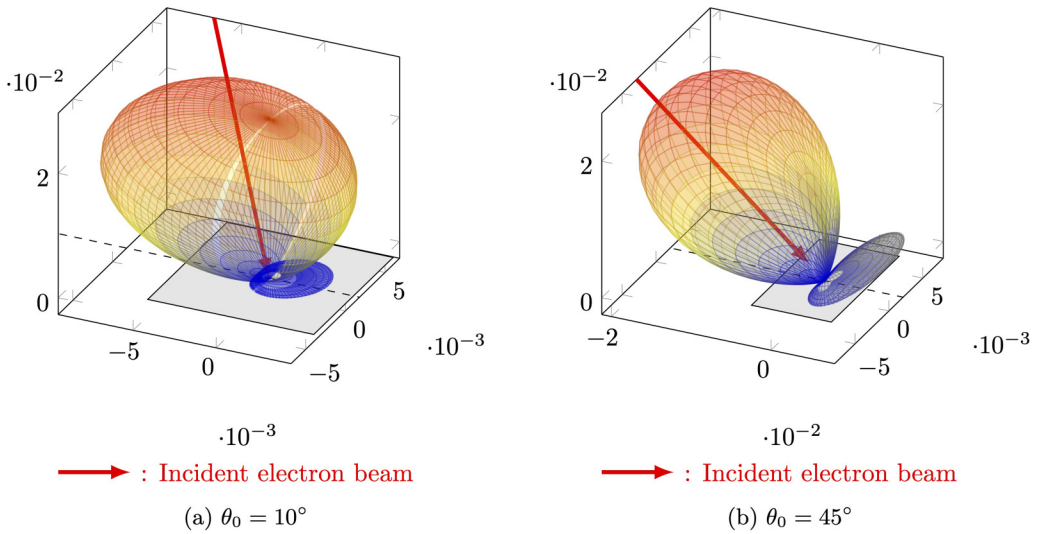

FIG. 7. Elastic backscattering lobes for the Al surface with an incident electron energy $E_p = 40$ eV and two different incident angle: (a) $\theta_p = 10°$ and (b) $\theta_p = 45°$. Reproduced with permission from Villemant *et al.*, IEPC-2017-366 (2017). Copyright 2017 Electric Rocket Propulsion Society.

energy and tend to recombine with wall electrons. This process is known as " ion recombination," and, for a saturated wall, nearly all impacting ions eventually return to the plasma as neutrals. Actually, impacting ions can also be reflected by the wall,[253] especially at grazing incidence angles and for very low mass ratios between the ion and the wall atoms, being the reflection probability negligible above a mass ratio of 2. Since ions for plasma propulsion are relatively heavy and significantly accelerated toward the wall inside the plasma sheath (hence they feature a close-to-normal incidence angle), ions reflection is typically neglected in most particle codes for plasma thruster simulations. Ions can finally be implanted into the surface, although this is extremely unlikely for heavy ions to occur, with recent studies showing that for Xe ions against an Al target, the implantation probability is around 0.2%–0.5% at normal incidence and energies above 300 eV.[254] When the ion is neither reflected nor implanted, recombination takes place (vast majority of cases), and the resulting neutral atom can either be adsorbed by the surface (to recombine into a neutral molecule, if this is possible), or be emitted back into the plasma. The probability for molecular recombination in the case of relevant alternative ion propellants such as N and O (see Sec. V A), is respectively 7% and 17%.[78] While recombined molecules are re-emitted in thermal equilibrium with the wall (i.e., with a mean emission energy equal to $2T_w$, where T_w is the wall temperature in energy units), and with an angular profile correctly represented by a Lambertian-cosine distribution, recombined atoms can be emitted with an average kinetic energy $< E_{emi} >$ that also depends on the impacting ion energy E_{imp}, as dictated by the energy accommodation coefficient α_w,

$$< E_{emi} > = (1 - \alpha_w)E_{imp} + 2\alpha_w T_w. \quad (15)$$

This coefficient generally depends on several factors, such as the mass ratio between ions and wall atoms, the surface cleanliness and roughness, and both the impacting particle energy and direction. However, in the absence of experimental data (which is generally available for light species at high energy levels[255–257]), numerical simulations generally assume values close to unity, as suggested also by a recent experimental evidence.[258] A large influence on plasma discharge properties, such as the propellant utilization efficiency η_m, has been observed in recent parametric studies.[259–261] In particular, a lower value of α_w produces a more energetic neutrals population, which is less easily ionized inside the thruster, thus reducing η_m. Regarding the angular distribution of the emitted recombined atoms, this can deviate from a Lambertian-cosine distribution, especially at grazing ion incidence angles, although the near totality of simulation codes neglect this for the sake of simplicity and for the lack of reliable angular data at the impact energies of interest. Finally, another source of confusion to take into account is that the energy accommodation coefficients and angle distributions reported in the literature generally capture the behavior of all reflected particles, including both reflected ions and recombined neutrals and are, therefore, incompatible with a simultaneous use of an ion reflection coefficient (to model direct ion reflection without recombination).

4. Gas–wall interaction models

Closely related to the ions–wall interaction, the gas–wall interaction is finally another topic of great interest for the simulation of electric thrusters and intake for atmospheric breathing electric propulsion. Although neutrals are not affected by electric and magnetic fields, their density profiles are strongly coupled with those of the plasma, as they determine the ionization source term, and both the momentum and energy loss terms for ions and electrons. In fact, the neutral propellant density can be up to 10 times larger than the plasma density, so that its accurate prediction is very relevant. Propellant neutrals generally feature a kinetic energy of fractions of eV, and, at these energy levels, there is a lack of available data regarding both the energy accommodation of wall-reflected neutrals[42] [also modeled with Eq. (15)] and their angular distributions. In particular, both experimental data and theoretical models do not cover the low-energy interval of interest. Regarding the former, it is extremely challenging to obtain a mono-energetic beam of slow neutrals, while regarding the latter, at low energies, the particle-wave nature of the impacting particle starts to emerge and classical mechanics models, like the hard cube or soft cube models,[262] start to fail. In any case, just like for ions, both the surface roughness and the impact angle affect both the energy accommodation coefficient and the angular distribution of the reflected neutrals. The most commonly used models for the simulation of neutrals reflection are the Maxwell's model, which considers a fixed probability for specular and purely diffused reflections, and Schamberg's model,[261,263] which depends on additional tuning coefficients to reproduce an intermediate reflection scenario affected by the impact angle. Reference 261 reports a study on the effect of the neutrals reflection model in an plasma discharge within a cylindrical chamber, assuming elastic (i.e., energy-conserving) collisions with the wall. Figure 8 shows how this model affects the trajectories and hence the residence time of neutrals inside the chamber, which is clearly overestimated by assuming a purely diffuse reflection. The considered model is observed to significantly affect both the minimum mass flow required for a sustained plasma discharge, and the propellant utilization efficiency η_m, at low values of this efficiency (less than 70%). In fact, at higher η_m, neutrals get nearly completely ionized inside the chamber regardless of the reflection model.

The gas–wall interaction is also particularly important for the optimization of the propellant injection location and of the air breathing electric propulsion (ABEP) intake performances. The first study has been recently conducted with a Direct-Simulation Monte Carlo (DSMC) model of the Xe gas propellant in a HT.[264] The work indicates that a reversed injection (propellant injected from the exit plane backward toward the anode) yields an increase of the propellant utilization efficiency η_m by a maximum of 30% with respect to the direct injection from the anode. The latter has been investigated by different DSMC models[265,266] that show the effect of flow misalignment and energy accommodation coefficient α_W on the intake performance. The importance of chemical reactions and recombination of atomic oxygen into O_2 molecules on the wall has also been highlighted in order to model the variation of the gas composition throughout the intake.[266]

IV. PIC MODELS OF PLASMA PLUME EXPANSION AND INTERACTION WITH THE SPACECRAFT

All electric thrusters produce plasma plumes that expand into free space and can interact with sensitive spacecraft surfaces and with

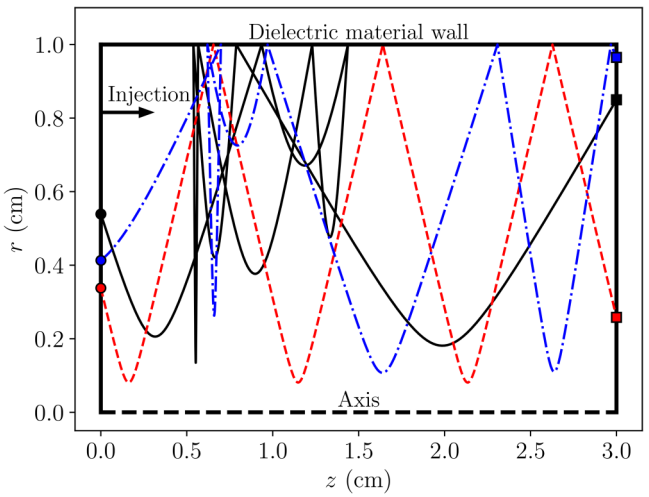

FIG. 8. Trajectories of neutrals inside a cylindrical discharge chamber. Propellant atoms are injected from the left boundary and get ionized by an isothermal electrons fluid. The dashed red line refers to the trajectory of a specularly reflected neutral, the black solid line to a purely diffused neutral, and the blue dashed-dotted line to a neutral reflected according to Schamberg's model. Reproduced with permission from Domínguez-Vázquez *et al.*, Plasma Sources Sci. Technol. **30**, 085004 (2021). Copyright 2021 IOP Publishing Ltd.

the onboard telecommunications system. Regarding the former, since not all propellant is ionized inside the thruster, the fast emitted ions interact with slow neutral particles through "charge exchange" collisions, which have the effect of producing slow ions whose trajectories are subject to the local electric fields. These collisions can, therefore, produce the so-called "ion backflow" toward satellite surfaces such as the solar arrays or optical sensors, whose performance can be significantly degraded by the induced sputtering and contamination/deposition. Concerning the interference of the electric propulsion subsystem with the telecommunications subsystem, this can be produced by either the thruster antennas/coils (e.g., the RF coil or the Helicon antenna in the corresponding thrusters) or by the plasma plumes themselves, which are not transparent to radio-waves with a frequency below the plasma frequency, a fact that generally occurs in the most dense plasma regions, close to the thruster.

For the above considerations, the system engineer of the hosting satellite must carefully select the installation position of the electric thruster, with the help of accurate plasma plume simulations, which should predict the plasma properties in the surroundings of both the thruster and the spacecraft, thus covering distances up to several meters. Currently, there exist three main simulation approaches to tackle this challenging task: the full-fluid,[267–269] the hybrid PIC-fluid, and the full-PIC approaches. In Subsections IV A–IV D, being this a Perspective paper on particle-based models, we shall focus on the last two approaches.

A. Hybrid models and their limitations

In order to simulate the plasma plume interaction with a generic spacecraft of arbitrary geometry, the simulation model must necessarily be 3D, with the consequent computational burden. Hybrid models[33–35,270–276] have, therefore, emerged in this context, as they represent the best compromise in terms of accuracy and computational cost for modeling the plasma thruster plume expansion and its interaction with the spacecraft. In fact, they feature a kinetic treatment of the ion species (and in some cases of the neutrals as well) so that charge exchange (CEX) collisions are correctly captured, and a fluid modeling of the fastest species, the electrons, which are subject to conservation equations. These features permit to avoid both time and spatial constraints of a full-PIC simulation: the electron CFL condition or the plasma and cyclotron frequency constraints for the time step, and the Debye length constraint in quasi-neutral plume regions for the cell size. The complexity of the electron fluid model depends on the considered closure for the electron conservation equations, which can be either a pressure tensor closure,[33,34,275,276] for models retaining the electron momentum balance equation, or a heat flux vector closure,[35,273] for models including also an electron energy balance equation.

In the first case, a commonly made choice is to assume polytropic electrons, whose temperature is a function of the electron density: $T_e(n_e) \propto n_e^{\gamma-1}$. Hybrid models belonging to this category can be further distinguished on the basis of the considered terms in the momentum balance equation. The simplest approach is to neglect all inertial, collisional, and magnetic field effects in the electron momentum balance equation[267,270,272,275] and obtain the electric potential from Boltzmann's relation as

$$\begin{cases} \phi = \frac{T_{e0}}{e}\ln\left(\frac{n_e}{n_{e0}}\right) & \text{for } \gamma = 1, \\ \phi = \frac{\gamma T_{e0}}{e(\gamma-1)}\left[\left(\frac{n_e}{n_{e0}}\right)^{\gamma-1} - 1\right] & \text{for } \gamma \geq 1, \end{cases} \tag{16}$$

where T_{e0}, n_{e0} are the reference electron temperature and density at a point where $\phi = 0$, respectively. The asymptotic electric potential (i.e., the potential limit for $n_e \to 0$) is, therefore, $-\infty$ for isothermal models ($\gamma = 1$), a clearly unphysical prediction, and a more realistic $-\gamma T_{e0}/[e(\gamma-1)]$ for $\gamma > 1$. Other more complex models obtain ϕ (or a related thermalized potential Φ) by solving the electron momentum balance equation, accounting for collisional effects,[33] which permit to obtain the electron current density, electron inertia effects,[93] relevant in certain regions characterized by large plasma gradients in the very near field plume, and magnetic field effects,[277,278] which are omnipresent in plasma plumes expanding in low Earth orbit (due to the geomagnetic field) or very relevant in the near-field plume region of HTs and most EM thrusters. The main drawback of these models based on polytropic electrons, however, is that they fail to reproduce correctly the electron temperature in magnetized plumes, like in a HT,[279] but also in unmagnetized scenarios, as shown later.

In the second case, the heat flux closure, the electron temperature is obtained by solving an electron energy-conservation equation.[35,273] Different types of closures have been considered: diffusive Fourier-like laws, with $\boldsymbol{q}_e \propto -\nabla T_e$, but also hybrid diffusive-convective closures, in which the electron heat flux vector has a component that is proportional to the electron fluid velocity. In this respect, it has been shown[280] that a purely convective law for the

heat flux vector, $\boldsymbol{q}_e = \alpha n_e T_e \boldsymbol{u}_e$ is equivalent to a polytropic electron model, provided that $\gamma = (5 + 2\alpha)/(3 + 2\alpha)$.

Hybrid models can also retain some charge non-neutrality effects, which are very relevant close to the spacecraft surfaces or in the peripheral plume regions, by accounting for Poisson's equation. In models featuring a pressure tensor closure, this can be added as a non-linear Poisson's equation to correct both the electric potential and the electron density in regions where the quasi-neutrality condition, $\epsilon_0 \nabla^2 \phi^* \ll e n_e^*$, is violated. Here, ϕ^*, n_e^* are the electric potential and electron density obtained by assuming quasi-neutrality. In such regions, it is possible to express the electron density as a function of the electric potential, $n_e = n_e(\phi)$,[33,34,281] thus yielding a non-linear partial differential equation. The simulation results from a hybrid model assuming polytropic electrons and charge non-neutrality are shown in Fig. 9, where the inclusion of non-neutral regions close to the spacecraft is clearly visible (the potential adapts to the satellite ground potential) and has the effect of increasing the ion back flow current by approx. 20% (compared to a fully quasi-neutral solution). Unfortunately, to the authors' knowledge, no benchmarking between non-neutral hybrid models and full-PIC simulation has been reported so far in the literature.

The above described non-neutral approach is not considered by models featuring a heat flux closure, where Poisson's equation is rather coupled with the other conservation equations as a correction of the electron density:[282] $n_e = n_e^* + (\epsilon_0/e)\nabla\phi^2$. Here, ϕ is the electric potential retrieved from the momentum balance equation, where charge non-neutrality has been assumed.

Hybrid plume models, however, present very relevant limitations, mostly related to the fact that their closures (at the level of either the pressure tensor or heat flux vector) miss important kinetic effects. As mentioned above, the polytropic electron thermodynamics (by far, the most common assumption in hybrid plume models) misses very important physics even in unmagnetized plasma plume expansions, as shown by recent studies assuming kinetic electrons.[283–287] Merino *et al.*[283] have shown, with a kinetic model based on Vlasov's equation, that plume electrons belong to three main groups: "free electrons" that have enough energy to go from the plasma source to infinity, "reflected electrons" that eventually get back to the source, and "doubly trapped electrons." The contributions of these populations change across the plume expansion, with the reflected and doubly trapped electrons vanishing downstream. As a result, the electron velocity distribution is anisotropic and different cooling rates (varying with the expansion) exist for the electron temperature parallel to the plume axis, and perpendicular to it. While the parallel temperature tends to an asymptotic value, hence with a cooling rate $\gamma_\parallel \to 1$, the perpendicular electron temperature tends to 0, with a cooling rate $\gamma_\perp \to \gamma_{\perp,\infty} > 1$. Recent full-PIC studies[284–286] on mesothermal and collisionless plasma plume expansions into vacuum, have also observed a clear anisotropy in the electron parallel and perpendicular temperatures of a planar plume expansion. Figure 10 shows the evolution of the electron parallel and perpendicular temperatures [subplot (a)], and the corresponding cooling rates [subplot (b)]. The parallel electron temperature seems to be nearly constant (at least for the already charged-neutralized plume considered),

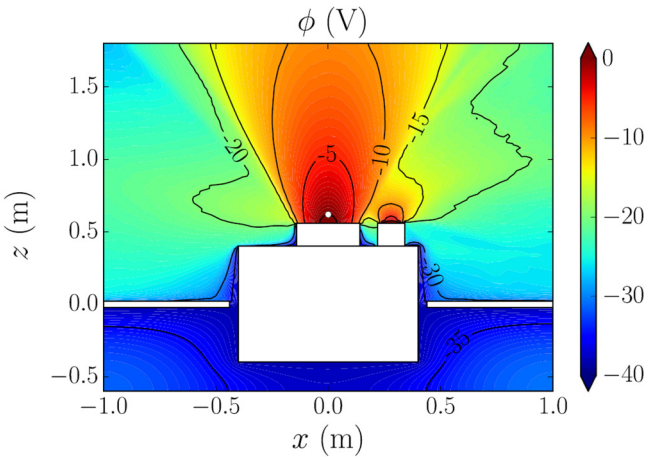

FIG. 9. Electric potential in the surrounding of a cubic satellite, predicted by a hybrid model, with polytropic electrons modeled with $\gamma = 1.1$ and non-neutral regions taken into account. Charge-exchange collisions for ions are included. Adapted with permission from Cichocki *et al.*, Plasma Sources Sci. Technol. **26**, 125008 (2017). Copyright 2017 IOP Publishing Ltd.

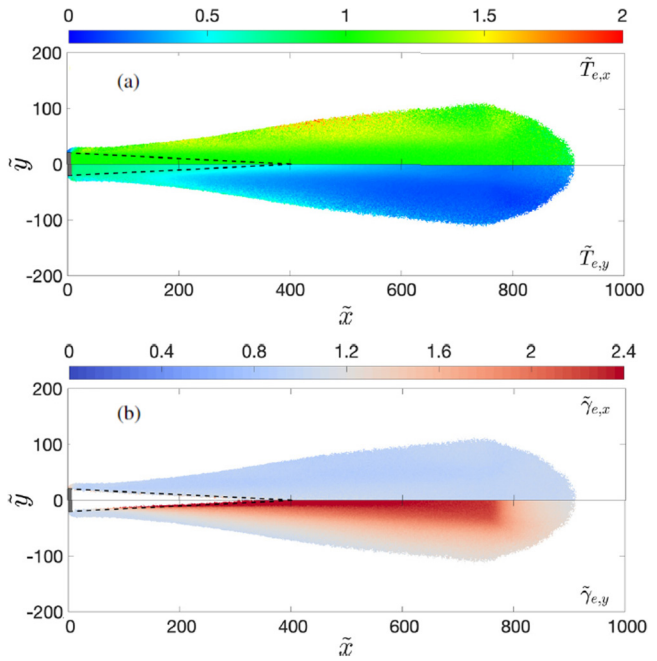

FIG. 10. Full-PIC simulation results showing (a) the electron temperature parallel to the plume axis $T_{e,x}$ (top) and perpendicular to it, $T_{e,y}$ (bottom) and (b) the local polytropic cooling rate for the parallel (top) and perpendicular (bottom) electron temperature. A current-free and quasi-neutral injection from $\tilde{x} = 0$ is considered (simulation B of Ref. 286). The plasma plume is considered collisionless, while the geometry is planar, with the plume extending infinitely in the direction normal to the page. Adapted with permission from Wang *et al.*, Phys. Plasmas **26**, 103502 (2019). Copyright 2019, AIP Publishing LLC.

with a corresponding cooling rate close to 1 and dimly dependent on the distance from the symmetry plane (in this case the plane $y = 0$). Instead, the perpendicular electron temperature shows a very quick decay, with a cooling rate that now depends on the symmetry plane distance and that approaches (and even surpasses) the adiabatic limit for the considered planar expansion (with a limit at 2).

It is, therefore, not surprising that a polytropic electron model based on a single coefficient γ cannot capture correctly the above physics and introduces errors even in macroscopic quantities such as the electric potential and the ion density, especially in the plume peripheral and backflow regions. Recent studies[285–287] have explicitly shown the shortcomings of a simple quasi-neutral Boltzmann's electrons model. While part of these differences can also be ascribed to the quasi-neutral assumption considered for the hybrid model, the kinetic effects described above are clearly missed by the latter and have a non-negligible effect on macroscopic plasma plume properties. Figure 11 shows the relative differences in ion and electron densities between a quasi-neutral Boltzmann's electron model (with $\gamma = 1$) and the same full-PIC simulation of Fig. 10: while the density is correctly captured within the plume core, relevant errors are found in the peripheral regions, for both ions and electrons. Finally, Nuwal *et al.*[287] compared full-PIC and Boltzmann/polytropic electron models, in a spacecraft interaction scenario for a collisional plume with CEX collisions. This study highlighted important differences in the predicted slow ions population (due to CEX), which is mainly responsible for spacecraft sputtering, charging, and contamination.

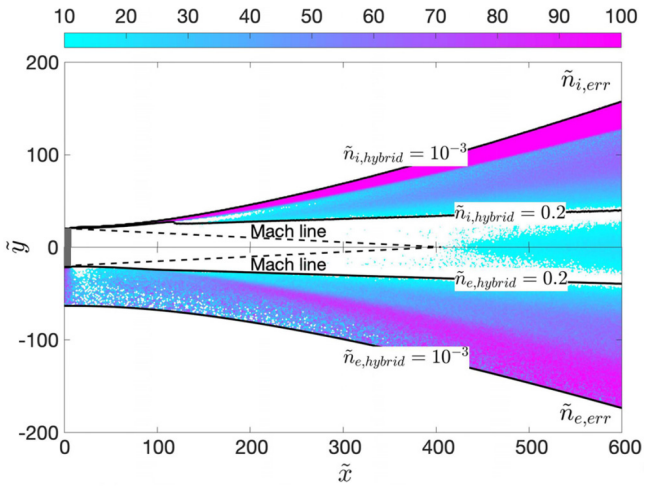

FIG. 11. Ion (top) and electron (bottom) relative density differences between a quasi-neutral hybrid PIC simulation with isothermal Boltzmann's electrons and a full-PIC simulation (simulation B of Ref. 286). The same simulation settings and plasma plume conditions of Fig. 10 apply (collisionless mesothermal expansion in planar geometry, with injection at $\tilde{x} = 0$). Adapted with permission from Wang *et al.*, Phys. Plasmas **26**, 103502 (2019). Copyright 2019 AIP Publishing LLC.

B. PIC models

In full-PIC plasma plume simulations, two critical topics are worth further discussion: the particles loading, and the boundary conditions for both particles and fields.

Ions and electrons can be loaded into the simulation domain from (i) a quasi-neutral and ambipolar injection surface,[286,288] (ii) from a non-neutral ambipolar injection surface,[286,287] in which a neutralization sheath that accelerates the electrons downstream is simulated, or (iii) from different non co-located surfaces for ions and electrons,[289] for studies on neutralizer–ion beam coupling. Achieving current ambipolarity is straightforward by loading the same number of electrons and ions from the emission surface and refluxing particles that return to the latter[290] (e.g., re-injecting them with the same loading distribution). For a locally current free surface and typical values of the ion Mach number (10–30), the number of electrons crossing the emission surface toward the simulated domain per unit time (due to both loaded and refluxed electrons) may be quite larger than that of the ions due to the very different thermal fluxes. Guaranteeing a quasi-neutral emission surface, on the other hand, is more subtle. One possibility is to either load ions and electrons with the same drift velocity into a volumetric source region,[285,286] which features a fixed plasma potential and adapts in time to guarantee the emission of a quasi-neutral and current-free plume, or by controlling the amount of emitted electrons at each time step, depending on the observed local charge.[288] Regarding the particle loading distributions, ions are generally injected according to a drifting Maxwellian distribution, with a small temperature and a hypersonic fluid velocity ($u_{\parallel,i} \gg c_s$, where c_s is the ion acoustic speed), representative of the considered thruster and, in some cases, accounting for a local plume divergence angle.[288] The electrons, on the other hand, are loaded with a Maxwellian distribution in the plane perpendicular to the plume axis, and with either a half Maxwellian[287–289] or a half Maxwellian-flux distribution[286] in the direction of the plume axis, that is,

$$\begin{cases} f_{\text{inj}}(v_\parallel, v_\perp) \propto |v_\parallel| \exp\left(-\frac{mv^2}{2T}\right) & \text{for } v_\parallel > 0, \\ f_{\text{inj}}(v_\parallel, v_\perp) = 0 & \text{for } v_\parallel \leq 0, \end{cases} \tag{17}$$

where $v^2 = v_\parallel^2 + v_\perp^2$. As shown in Ref. 290, it is this latter distribution that correctly reproduces a half-Maxwellian distribution function at the injection surface. For a globally current free plume, the full-Maxwellian electron distribution at the source is recovered due to the emitted electrons that are reflected back toward the source, with the exception of an empty region at high negative velocities (i.e., returning to the source) due to free electrons lost downstream.[288]

Coming now to the boundary conditions for the electric potential, a Dirichlet condition is generally applied at the injection boundary, and homogeneous Neumann conditions are imposed at the remaining open simulation boundaries. Things are more tricky for macro-particles: while ions crossing the simulation boundaries are simply removed from the simulation, electrons are either removed[285,286] or selectively reflected.[288,289] The first approach suffers from more restrictive computational constraints since boundary effects are more relevant and larger simulation boxes are required. This is clear in Fig. 10 where results have been analyzed

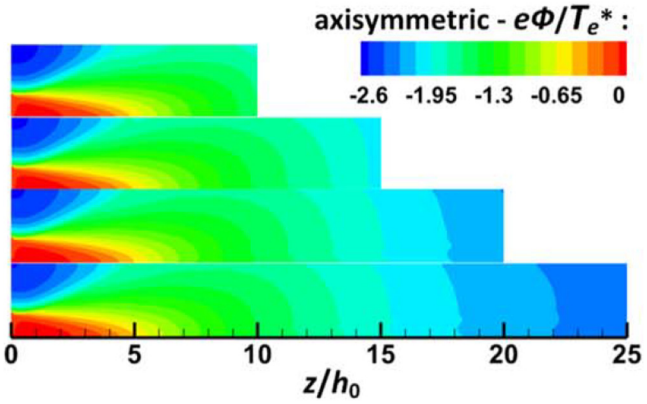

FIG. 12. Normalized electric potential in a 2D axisymmetric plasma plume simulation for four different domain extensions along the plume axis and using open boundary conditions for electrons. Reproduced with permission from Li *et al.*, Plasma Sources Sci. Technol. **28**, 034004 (2019). Copyright 2019 IOP Publishing Ltd.

before the quasi-neutral plume reaches the downstream boundary. The second approach, on the other hand, is capable of reducing downstream boundary effects by reflecting a fraction of outer boundary-crossing electrons, based on their mechanical energy,[289] or on the global net current exiting the domain in the last PIC steps.[288] The goal of these approaches is to mimic the partial reflection of electrons taking place further downstream, outside of the simulated domain and, therefore, to reduce the influence of the boundaries on the achieved results, as shown in Fig. 12. Here, the steady state electric potential of an axisymmetric and collisionless plume expanding into vacuum (from left to right) is plotted for four different domain extensions (along the plume axis), showing very limited effects of the downstream boundary.

C. Circuital characterization of plasma–spacecraft interaction

In order to fully characterize the plasma–spacecraft (S/C) interaction, the plasma plume model must be appropriately coupled with a representative circuital model of the satellite surfaces. In fact, the latter affect the plasma, as they impose given electric potentials and/or plasma currents and represent ion recombination sources (into neutrals) and electrons sinks, while the plasma affect the S/C surfaces through both direct sputtering damage and electric currents that can yield to a charge buildup and eventually electrical components breakdown. Past studies have tried to couple a plasma plume model to a circuit model of the spacecraft, or at least to assess the plume induced erosion on the most relevant surfaces.[291] In all cases, given the extremely large computational domain and the intrinsic multi-scale character of the plasma–satellite interaction, the plasma plume model considered has been of the hybrid type (typically with polytropic fluid electrons). The circuital representation of the S/C components in contact with the plasma can either consider lumped elements[33,281] (i.e., the different macro-surfaces are treated as single nodes) or distributed elements with macro-surfaces discretized with a large number of elements or circuit nodes to handle very complex satellite geometries, with the use of unstructured meshes with tetrahedral volume elements (see Fig. 13).[34,275] In all cases, the potential and the currents flowing through these circuit nodes are solved through Kirkhoff's laws.[33,34] Two main types of surface elements are generally considered in the model: (i) dielectric surfaces which, depending on the model, either force an equal ion/electron current from the plasma[33] or are charged up by the net plasma current without transferring this accumulated charge elsewhere,[34] and (ii) conductive/partially conductive surfaces which can exchange electric currents with other elements and are eventually connected to the spacecraft bus. When transients are requested and the electrical capacitance of the metallic surfaces is well known, implicit schemes to solve Kirkhoff's laws are employed to improve the stability of the modeled circuit, using time steps for the charge propagation that can be lower than the time step considered by the hybrid plasma plume model. Finally, while the electric currents to the surfaces are straightforward to compute from a full-PIC plume model, this is not the case when using a hybrid model. In this case, the electron contribution to the collected current is computed by either assuming the electron thermal flux j_{e0} (when the plasma potential ϕ is lower or equal to the surface potential ϕ_w) or by calculating the electron net flux crossing a thin plasma sheath (when quasi-neutrality holds and the sheath is not resolved in the model), i.e.,

$$j_{w,e} = j_{e0} \exp\left(-\frac{e(\phi - \phi_w)}{T_e}\right). \quad (18)$$

D. Plume-electromagnetic compatibility

The impact of electrical thrusters on the telecommunications system of the satellite is a critical point when thrusters are firing. To be electromagnetically compatible, the radiations emitted by the propulsion sub-system must be under a certain level to avoid interference with the satellite. The emission of the radiated electric field has been measured on a wide range of frequency, from tens of MHz to tens of GHz frequencies corresponding to the antenna emission band, using semi-anechoic chambers (to prevent the thruster from the electromagnetic environment) juxtaposed to standard vacuum chambers where the thrusters operate.[8,292] Specific electrical sensors that can be directly mounted in the vacuum facility simplifying the measurement system have also been recently proposed in the context of HTs[293] and VATs.[293]

Furthermore, the charged particles that compose the thruster plume can alter the operation of the antenna by modifying the telecommunications or telemetry signal. This issue has been addressed in a recent modeling study in the context of a HT mounted on a small size satellite simplified mockup.[294] A 2D hybrid-PIC plume model called JET2D[295] has been adapted and validated against the ion angular current distribution measurements of a miniature HT[296] to determine the profile of the electron plasma frequency (from the predicted density profile). Assuming a constant electron-neutral collision frequency, the profile of the electric permittivity (under the Drude's approximation[297]) can be computed and used as input data for an electromagnetic solver (Ansys

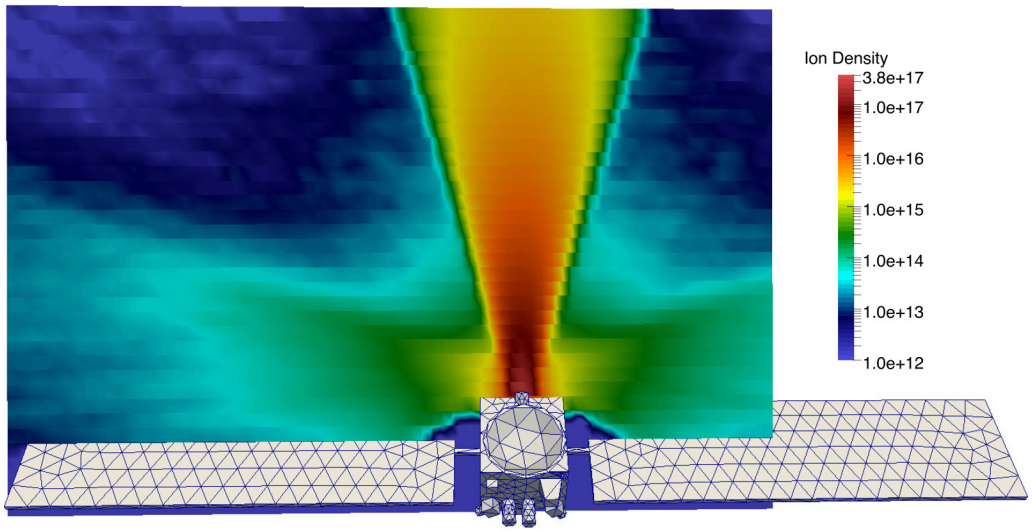

FIG. 13. Ion density predicted with a hybrid plume model with polytropic electrons (inertialess, unmagnetized, and collisionless) and $\gamma = 1.3$, in a complex geometry scenario, corresponding to the DAWN spacecraft. Charge exchange collisions for ions are included. Courtesy from S. J. Araki, IEEE Trans. Plasma Sci. **47**, 4898–4908 (2019).

HFSS[298]). De Mejanes *et al.*[294] have applied this versatile approach to a dipole antenna at 436 MHz on a 6U nanosatellite. Figure 14 shows the antenna gain radiation pattern when the thruster operates (case indicated as ON) or not (case indicated as OFF). This gain can be defined as the ratio between the radiation intensity in a given direction and the one that would be produced if the power accepted by the antenna were radiated isotropically. Two planes are presented, one in the antenna emission plane ($\varphi = 90°$), the other in the plane perpendicular to the emission ($\varphi = 0°$). In Fig. 14, the angle θ in the bottom part of the cycle corresponds to the plume region. For example, when $\theta = 180°$ and $\varphi = 0°$, the gain is only reduced by 1 dB when the thruster is firing. The plume thus only distorts the radiation pattern. The work of De Mejanes *et al.*[294] highlights the capability of the combined approaches to capture the interactions between the antenna and the plume for real scenarios.

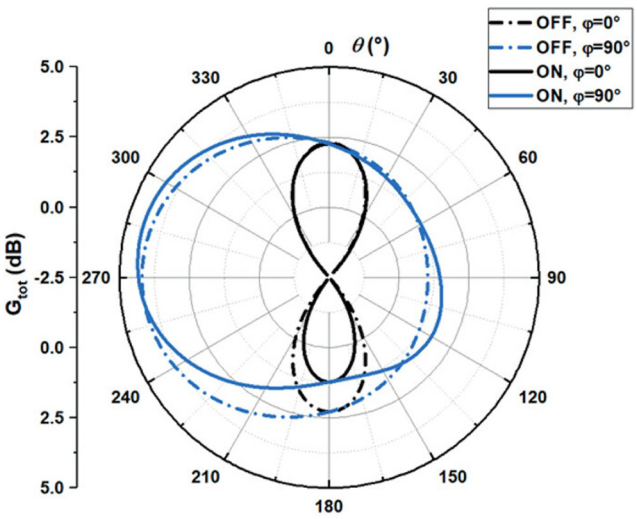

FIG. 14. Antenna gain radiation pattern for two scenarios, in the antenna emission plane ($\varphi = 90°$) and in the plane perpendicular to the emission ($\varphi = 0°$) with (ON) and without (OFF) plasma. Reproduced with permission from De Mejanes *et al.*, J. Appl. Phys. **131**, 243303 (2022). Copyright 2022 AIP Publishing LLC.

V. FUTURE CHALLENGES

In this section, the most relevant challenges that concern the improvement of numerical simulations dedicated to EP are addressed in detail. Some promising recent lines of research development for EP particle-based simulations are presented. In particular, regarding the simulations faithfulness and reliability, we refer to the progressive inclusion of complex bulk and surface plasma chemistry and to the self-consistent simulation of the plasma–gas coupling. Concerning the simulations computational feasibility, various topics are treated, such as high performance computing techniques, cost reduction techniques, and deep-learning based methods.

A. Collisional database and alternative propellants

Particle-based models allow for an accurate description of electron and ion collisions with neutrals, that represent crucial processes to correctly simulate the transport and assess the global efficiency parameters of the diverse thruster configurations. Therefore, a predictive particle model not only requires a proper implementation of the numerical solution techniques but also depends on the

availability of reliable input data, such as electron-scattering and ion-scattering cross-sections with neutrals. Even if nowadays the number of experimental/theoretical groups measuring/calculating cross sections is rapidly diminishing, large data sets (presented as look-up table with non-uniform energy intervals) are collected[299,300] (often for total and rarely for differential cross sections) and available on different web platforms.[301–305] For this reason, different approximations are used for the calculation of the anisotropic scattering angle valid for some electron-neutral[306,307] and ion-neutral[42,308] collisions in Monte Carlo simulations.

Simulation results are highly sensitive to the model used for neutral dynamics. It has been recently[309,310] demonstrated that different numerical treatments of the neutrals change the spatiotemporal evolution of a HT discharge. Ion-wall recycling, neutral-wall reflection, and energy accommodation coefficients, and ion-neutral collisions cause a significant variation in the neutrals density and temperature maps. The plasma–neutral coupling is very difficult to implement due to the large disparity in their respective spatial and temporal characteristic scales and density. An attempt[78] has been made by developing a particle-based code with two different alternating modules for the plasma species (PIC/MCC) and for the neutral gas species (Test Particle Monte Carlo—TPMC), which are iterated and coupled until convergence. The two modules use their own proper grid and time steps to evolve their corresponding Boltzmann's equation. The resulting simulation loop scheme is reproduced in Fig. 15.

The plasma–gas coupling becomes fundamental to estimate thruster performances in case of molecular propellants. For air species (N_2–O_2 mixture relevant for the air-breathing concept[78,311–313]), iodine I_2,[314,315] water vapor H_2O[316,317] and carbon dioxide CO_2[318] (relevant for Venus and Mars atmospheres), the large variety of electron-molecule processes, the gas–wall interaction (tackled in Sec. III C) and the molecular vibrational kinetics must be included for a realistic estimation of the ionization efficiency. In particular, the energy partition between atomic by-products in the electron-induced molecular dissociation is very important for determining the possible impact of the subsequent ionization of hot atoms.

In this regard, in order to measure the ionization efficiency of a particular propellant, it is often useful to calculate the electron energy used for ionization compared with the energy dissipated in all inelastic processes. The global energy cost to create an electron–ion pair in the thruster discharge[319] is defined as

$$W = \sum_{s=1}^{N_s} \chi_s W_s, \tag{19}$$

where the index s refers to the different gas species (atomic and molecular) of the propellant mixture, χ_s is the neutral fraction of the sth neutral species and W_s represents the corresponding cost to create an electron–ion pair defined as

$$W_s = \frac{\sum_{p=1}^{N_p} \varepsilon_p k_p}{k_{\text{ion}}}. \tag{20}$$

Here, the numerator represents the total inelastic power losses, that is, the total energy loss due to all inelastic processes (including the ionization) involving the electron and the neutral species s. k_p and ε_p are the inelastic rate coefficients and the energy thresholds for the inelastic process p, respectively. In the denominator, k_{ion} is the ionization rate coefficient of the process $e + S \rightarrow 2e + S^+$. Figure 16 reports W_s for different species: Ar, Xe, air species, and iodine.

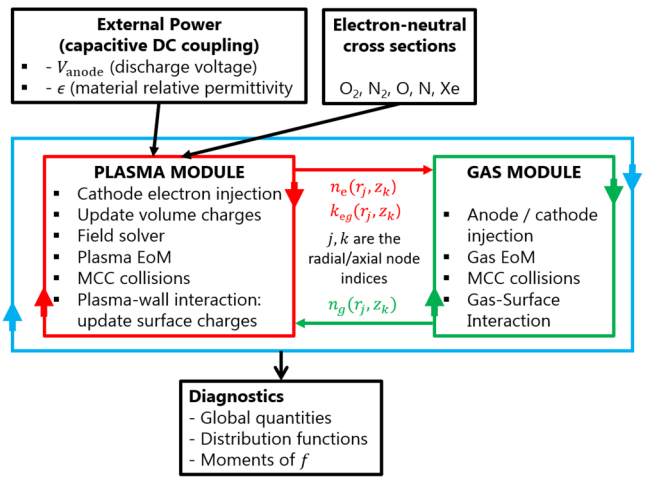

FIG. 15. Scheme of a coupled PIC–MCC/TPMC simulation for a HT discharge simulation. The plasma (gas) modules see, respectively, the neutral gas (plasma) as fixed non-uniform backgrounds with density n_g (n_e), Reproduced with permission from Taccogna *et al.*, Front. Phys. **10**, 989 (2022). Copyright 2022 Frontiers Media SA.

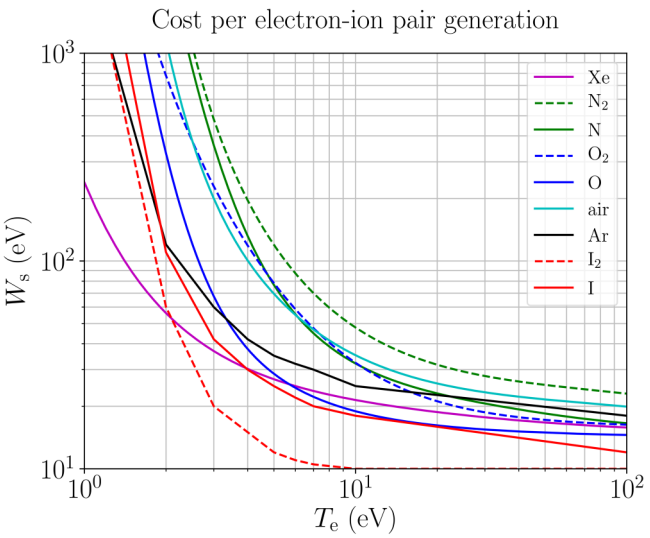

FIG. 16. Collisional energy loss per electron–ion pair created, W_s (eV), vs the electron temperature T_e (eV) in Xe and air relevant species (N, N_2, O, O_2 and an air mixture 0.5 N_2/0.5 O)[78] and in atomic (I) and molecular (I_2) iodine.[314] Atomic species are shown by solid lines, while molecular species by dashed lines.

Usually, all the atomic and molecular species are assumed to be in their electronic ground state since, in the low-pressure regime typical of electric thruster discharges, the radiative excited states decay to the ground state much faster ($\tau_{rad} \approx 10^{-9}$ s) than the electron collisional time. Therefore, the ionization process is always taken from the electronic ground state, a fact that does not hold true if metastable states exist. Recent studies[320–323] are starting to investigate the role of metastables (for Ar, Xe, and O_2) and of vibrational kinetics (for molecular propellant) with particular emphasis on the impact of stepwise ionization. In this regard, often, state-selective (dependant on the initial vibrational state of the molecule) and ionization of metastables cross sections are often missing in the literature. Figure 17 reports, for Xe, the excitation rate coefficients from ground to any excited state (exc. tot.) and from ground to the two metastable states ($1s_5$ and $1s_3$, in Paschen notation). Additionally, the ionization rates of the ground state and of these two metastable states are also reported, showing that, at low electron temperatures, the contribution of metastable states to the total ionization rate can be relevant. A particle description of the vibrational and electronic neutral gas kinetics (i.e., differentiating neutral macro-particles in terms of their vibrational and electronic states) will permit to assess the impact of metastable and vibrationally excited states on thruster performances.

Finally, when large differences in number density exist among the different species, it is natural to introduce different macro-particle weights for them. This is convenient in particle simulations because equal statistical fluctuations for instantaneous weighted properties require equal numbers of macro-particles per cell. However, this comes at the cost of important variations to the classic collisional algorithms, in order to conserve mass, momentum and energy.[60] As an illustrative example for a DSMC collision scenario, if a "small" ion macro-particle undergoes a charge-exchange collision with a "big" neutral macro-particle, only a fraction of the latter must suffer the effects of the collision.[33]

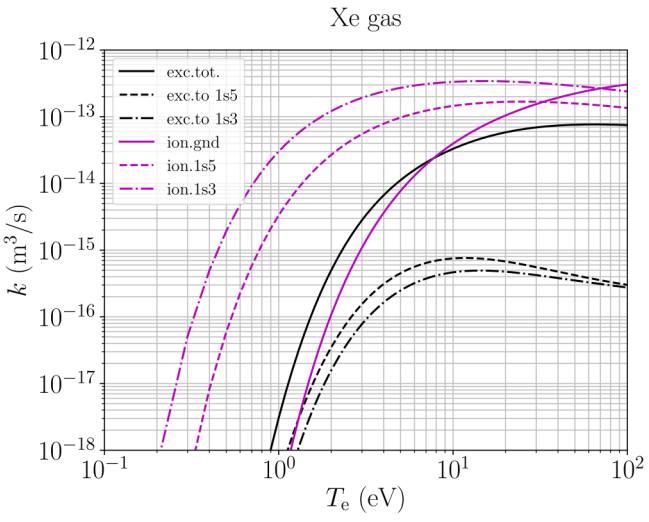

FIG. 17. Xe excitation rate coefficients[324] from ground to any excited state (exc.tot.) and from ground to metastable states (exc.to 1s5, exc.to 1s3), and Xe ionization rate coefficients of the ground state[324] (ion.gnd) and of the two metastable states[325] (ion.1s5, ion.1s3). Paschen notation is considered here.

B. HPC techniques

The multiscale nature and large computational domains required in EP particle simulations have fostered the adaptation of existing codes to relatively new and highly efficient parallelization techniques.[326] As an illustrative example, a 3D SPT-100 channel features a length of around 3 cm, and inner and outer channel radii of, respectively, 3.5 and 5 cm. For an average plasma density of 10^{18} m^{-3} and an electron temperature in the order of 10 eV, the Debye length is approx. 20 μm, which means that a 3D simulation would require around 10 billion cells, and, therefore, hundreds of billions of particles (for a reasonable noise level). The corresponding memory to store information on these numbers of macro-particles is in the order of 10 TB of RAM memory, which clearly requires a distribution of the computational task over a large number of physically separated computational nodes. Large sizes of the numerical model also affect the Poisson's equation solver. In fact, both the required RAM memory and convergence times may not be tractable, unless some parallelization technique is used. In this respect, domain decomposition with MPI can produce a theoretical maximum speedup that scales linearly with the number of MPI processes. In certain circumstances super-linear scaling may be observed if the entire grid can be maintained within a higher level of cache.

1. Hybrid MPI-OpenMP parallelization

The most classical massive parallelization technique employs a particle and mesh decomposition through the combined "Message Passing Interface" (MPI) and "Open Multi-Processing" (OpenMP) parallelization techniques.

The MPI parallelization technique has been developed in 1990s[327] and consists in running simultaneously the code on several computational nodes (or processes), which can exchange information with the others through communication over a network protocol. When using MPI, the simulation domain is generally split between these processes, and the number of neighbors of such a domain decomposition depends on the dimensionality of the problem: two neighbors in 1D, eight neighbors in 2D, and 26 neighbors in 3D. A subdivision of the global domain between MPI processes permits to overcome the RAM memory issue introduced above, since each node now sees only a fraction of the global simulation data. Moreover, the maximum number of available cores for the computational task is no more limited to that of a single physical CPU (nowadays, limited to 48–56 physical cores), so that an extremely large speed-up can be achieved (examples in EP simulations already exist showing speed-ups in the order of 1000[328]).

The drawback of using MPI is related to the overhead for network communication between processes, which depends on the amount of communicated data, on the amount of blocking communication (non-blocking communication, on the other hand, can significantly reduce the overhead), and on the latency and bandwidth of the network type. In particular, gigabit and InfiniBand are the most common network protocols, with the latter enabling

larger transfer rates but being generally more pricey.[329] Of course, particles are subdivided between MPI processes just like the simulated domain, and a dedicated communication function must be envisaged to exchange particle data whenever a particle leaves an MPI process sub-domain and enters that of a different process. In this respect, in order to reach the best performance, it is paramount to have a homogeneously distributed computational effort between the different processes, a fact that has led to the development of new MPI codes with dynamic load balancing.[330]

MPI domain decomposition is normally coupled with OpenMP,[128] a HPC technique for shared memory systems that is compatible with MPI and consists of multi-threading, i.e., in dividing the computational task of a single MPI process between several threads, whose number should not exceed the number of available physical cores for that specific process, unless hyper-threading is efficiently exploited. Many codes in the literature for plasma thrusters and their plumes are actually parallelized with OpenMP alone, since its implementation is much easier than with MPI. In the case of OpenMP, care must be used to avoid the existence of race conditions, or simultaneous access by different threads to the same RAM memory variable. These race conditions can produce bugs and memory errors and are normally handled with several approaches, such as reduction operations (consisting of making thread-private copies of certain variables), or atomic/critical commands, that however significantly slow down the code execution.

Another very relevant HPC technique that should be pursued is the efficient use of the L2 cache memory. Modern CPUs are capable of performing very efficient operations and optimizing the access to the slow RAM memory. In order to take advantage of the CPU efficiency, operations such as charge deposition and field gathering should be vectorized, while for optimizing the RAM access, the computational data should be stored compactly. This can be achieved by further dividing the macro-particles of a given MPI process into smaller physical sub-domains, called tiles,[331] and/or through particle sorting algorithms,[332,333] which order the particles in terms of their occupied cells. However, when RAM memory is compacted, the probability of incurring race conditions between OpenMP threads during the charge deposition phase can also increase, unless charge deposition algorithms that avoid such conditions[331] are used. The use of OpenMP atomic procedures, on the other hand, is discouraged as it reduces the overall parallel performance.

Finally, especially in multi-scale simulations, in which the plasma density changes by several orders of magnitude across the domain, the overall computational cost can be reduced with "Adaptive Mesh Refinement" (AMR) techniques,[334] based on octrees.

2. Massive parallelization on GPU

Graphics processing units (GPUs) represent very powerful hardware having a throughput-oriented architecture, with raw arithmetical performance and memory bandwidth far exceeding those of conventional central processing units (CPUs). However, GPUs can realize their potential only for a special class of problems, which can be partitioned into a large number of sub-problems on two levels. On the coarse level, the sub-problems should be independent of one another for the sake of scalability and are to be processed by blocks of threads, while, on the fine level, the sub-problems are to be concurrently processed by threads communicating via different means within the block. Due to the much larger number of resident threads compared to the number of physical execution units on GPUs and a very small overhead of switching between the threads, it is possible to hide the latency by quickly finding threads ready for execution and dispatching them to the physical units. The number of physical execution units on a single GPU is still very large and can be more than a thousand. The reason is that GPUs do not need sophisticated control units predicting the execution path for each separate thread to reduce the overall latency as it is done on CPUs, relying instead on using a GPU analog of the "single instruction multiple data" parallel computing paradigm.[335] The available transistors not dedicated to the control units can thus be utilized for the execution units. With GPUs having a shorter history of development compared to that of CPUs, GPU global memory controllers are not strongly bound by the requirements to be compatible with old protocols, which allows GPU engineers to experiment more with novel concepts resulting in significant boost of the global memory bandwidth, e.g., via the advanced HBM (high bandwidth memory) interface. In turn, the traffic to the global memory on GPUs can be decreased through the data reuse employing different additional programmable fast memory types if the PIC algorithm exhibits a sufficient degree of locality, reducing the need for a complicated and bulky system of automatically managed cache memory typically present on CPUs.

On the node level, one can combine both CPU and GPU types of hardware by identifying parts of the algorithm which have a lot of branching points, hard-to-resolve data dependencies, and/or an inherently non-local global data access pattern. These parts would fit better for CPUs, whereas algorithmic parts with a large number of sub-problems requiring a similar instruction and data access pattern to solve, are better off placed for execution on GPUs. On a coarser level, the problem can be upscaled by harnessing multiple CPU threads (e.g., via OpenMP) or multiple GPUs on a single node and/or multiple nodes using the MPI set of instructions.

The PIC/MCC algorithms are well parallelizable on GPUs, either in whole or just for the particle-related parts (the particle pusher, particle sorting, collisions, charge or current density assignment), which typically require most of the computational time. The latter option can also have certain advantages: due to the reduced size of the transferred data (in the charge and/or current density) and the relatively large CPU–GPU bandwidth on modern computers, the cumulative time penalty of calculating the fields on CPU is not high and can be hidden by overlapping with the execution of some other task (for example, the processing of MCC algorithms), which would keep CPU and GPU busy simultaneously.

Parallelization of the particle-related parts of the PIC algorithm on GPUs is typically based on two different approaches. The first approach relies on particle sorting with respect to their positions (e.g., Ref. 336), which enables to minimize the race conditions when calculating particle moments serving as the field sources, binary collision-based models, and adaptive particle management. In addition, it strongly improves the data locality, which is beneficial for data reuse utilizing the automatic cache or the manually controlled shared memory. The second approach spares the particle sorting but needs to use the atomic addition functions for the calculation of field

sources (e.g., Ref. 337). Due to the improved performance of atomic functions on modern GPUs, this can be a viable option if no additional algorithms demanding particle sorting are required.

An example of GPU parallelization of codes used for EP modeling can be found in Ref. 338 for a single GPU and in Refs. 334, 339 and 340 for multiple GPUs. In addition to that, one can find discussions of GPU parallelization techniques used in commercial codes.[341,342] Popular frameworks for GPU parallelization are the NVIDIA-specific "Compute Unified Device Architecture" (CUDA[335,343]), and the vendor-independent OpenCL,[344] Kokkos,[345] RAJA[346] and "Open Accelerators" (OpenACC[347]). The latter has been recently used to parallelize the LTP-PIC code developed by the PPPL group and utilized previously for the benchmark in Ref. 107. The massive GPU parallelization using CUDA was employed in the implicit energy-conserving ECCOPIC2S-M code used by the RUB team in the HT-related benchmark described in Ref. 107. However, because of the benchmark requirements, the code was run using the same time and cell size as the other explicit PIC codes so that the benefits of the GPU parallelization became visible only in a different benchmark.[122] A GPU-parallelized explicit version of the same code used by the RUB team showed a performance comparable to the best CPU-based code. Whereas it is hard to make direct performance comparisons, since the final performance depends on the number of GPUs and CPUs used, one can consider a heterogeneous CPU-based system enhanced with GPUs as a competitive cost-, size-, and energy-efficient alternative to large clusters based on CPUs only. Note also that GPUs offer numerous opportunities of utilizing additional computation units performing computations with a reduced precision, which can be combined with more accurate calculations in critical parts of an algorithm without noticeable net precision losses.

C. New numerical techniques for computational cost reduction

In this section, we present some ideas implemented in a classical PIC scheme to increase computational performances. In particular, the techniques used and verified in the modeling of electric thrusters will be shown.

1. Sparse-grid method

The sparse grid (SG) method is a specific discretization technique used for the interpolation of functions and resolution of partial differential equations.[348] The SG method is based on the construction of a system of sub-grids with a coarser resolution that will be used for the calculations. The solution of the problem can be reconstructed by the combination of the solution on each of the sub-grids with a minimizing error by using the so-called combination technique.[349] Recent studies have combined SG and ES PIC approaches with the combination technique. Ricketson *et al.*[350] have demonstrated the proof-of-concept by studying Landau damping in 2D and 3D, and the diocotron instability in 2D, assuming a collisionless plasma where ions remain at rest and using purely periodic boundary conditions. Garrigues *et al.*[351,352] have extended the method to low temperature plasma discharges including collisions, charged particles motion, and Dirichlet boundary conditions.

In PIC models, the main source of error is the numerical noise or statistical error due to the particle sampling method.[5,48] For the standard PIC approach, the total number of cells is $O(N^d)$, where N is the number of grid points per direction and d is the number of dimensions. The SG method employs $O(N(\log N)^{d-1})$ grid cells, which is much lower than in the standard PIC algorithm. Using the same total number of particles leads to a reduction in the statistical error using SG techniques, but more interestingly, for the same statistical error, the total number of particles employed in the SG approach can be much less.[353,354] By diminishing the total number of particles, both the resources for memory storage and computational time are reduced (see Refs. 355 and 356 for efficient parallelization of SG PIC algorithms on CPU and GPU shared memory architectures, respectively).

Figure 18 shows a comparison between the standard and SG ES PIC models in the context of the ECDI in a HT.[352]

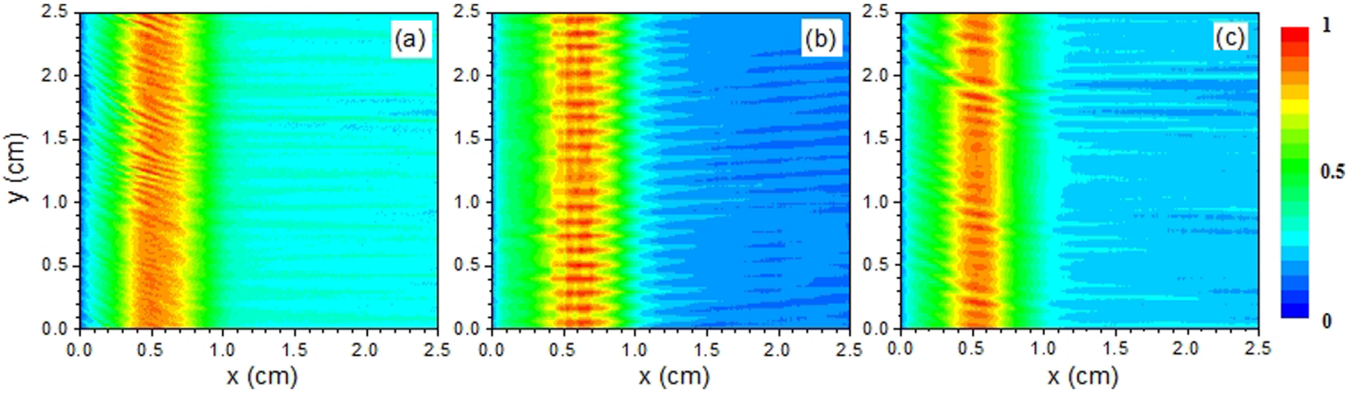

FIG. 18. Axial x–azimuthal y simulations of the HT ECDI for a computational domain of 512 × 512 grid cells. 2D profiles of ion density at a given timestep, with (a) standard ES PIC, (b) sparse grid ES PIC, and (c) sparse grid oversampled ES PIC. The maximum ion density is 2×10^{17}, 2.2×10^{17}, and 2.1×10^{17} m^{-3} from left to right figures, respectively. The number of particles-per-cell is the same (400), and the total number of particles is 10^8, 5.2×10^6, and 2×10^7, from left to right, respectively. Adapted with permission from Garrigues *et al.*, J. Appl. Phys. **129**, 153304 (2021). Copyright 2021 AIP Publishing LLC.

The conditions are the same as in Fig. 4 except that the computational domain is now a square. Comparing Figs. 18(a) and 18(b), we see that the SG ES PIC algorithm is capable of reproducing the ion density profile and the ECDI instability but with a certain error that can be reduced using more sub-grids (but accompanied by a reduction of the computational gain). This is due to the numerical error associated to the mesh size of sub-grids and reconstruction using the combination technique that is not able to cancel out the non-mixture derivatives for non-smooth solution profiles. By applying a recently proposed oversampled sparse PIC scheme able to reduce the grid-based error detailed in Ref. 353, a better agreement between standard and sparse PIC algorithms is visible [comparing Figs. 18(a) and 18(c)]. The acceleration factors are 6.5 and 4 between standard and SG ES PIC and SG oversampled ES PIC models for identical computer resources, respectively. Work is underway to extend this method to 3D HT models.[357]

2. Implicit PIC models

The explicit PIC method (see Sec. II) evolves particle positions and velocities based on the information available from the previous time steps, which minimizes the number of calculations needed to make the update to the next time level. In particular, note that in the fully EM case, one calculates field components at the next discretized time instant from the corresponding time derivative, with all other quantities taken from the current one, which makes an algebraic matrix inversion unnecessary, provided the leapfrog algorithm is used. The drawback of this approach is the corresponding decoupling of the particle, electric, and field evolution during the time step. If the latter exceeds a characteristic time scale intrinsic to the discretized field-plasma system, such as the plasma period or the time it takes an EM wave to cross a grid cell, the PIC algorithm becomes unstable due to the stiffness of the underlying differential equations. Another problem of the conventional explicit algorithm used in most cases is that the same function for the charge density assignment to the grid vertices and the reciprocal field interpolation leads to the "finite-grid instability" (FGI), causing numerical heating compromising or breaking down the simulation if the cell size becomes greater than the Debye length. For modeling discharges with large plasma densities or large dimensions, this can be a big problem since the required large computational grid will translate into a long computation time, especially for multi-dimensional simulations.

To circumvent these limitations, it was proposed to use implicit methods, which are based on time integration algorithms that evolve particles and fields in a coupled way. Although such methods typically require many more computations compared to the explicit PIC, their stability does not depend on having to resolve the Debye length, the time it takes for an EM wave to cross a grid cell, or the plasma period. As a result, the overall cost of an implicit PIC simulation modeling a dense plasma can be much smaller than that of an explicit PIC simulation (although the resolution might still be constrained by the physics under investigation, e.g., the Debye length in the sheath, which can, however, be dealt with using non-uniform grids). Two early implicit PIC approaches were proposed in the literature: the direct-implicit method (DIM)[358,359] and the implicit moment method (IMM).[360,361] Although originally these methods were formulated in a fully implicit form that required an iterative procedure to converge, due to the low computational power of computers of the past, the methods were most frequently used in a semi-implicit form requiring just a single iteration, as in the case of the explicit method.

The DIM linearizes equations describing the time evolution of the discretized field-plasma system with respect to the fields at the new time instant, which allows expressing the charge and current densities as a sum of two parts, of which the first one is calculated using the previously known quantities and the second one is proportional to the new electric field. The latter can be combined with the other terms in the discretized Maxwell's equations, which contain the new electric field. The equations determining the time evolution of fields and particle orbits are usually discretized in DIM using the leapfrog algorithm.

In contrast to this, the IMM estimates the new electric field from the momentum equation linearized with respect to the new electric field, albeit with the stress tensor calculated from the PIC data of the current time instant. The electric field estimate for the new time instant calculated in this way would differ from the new electric field obtained from Maxwell's equations, but if the time step is not very large, the discrepancy can be tolerated. The time integration scheme exploited in the IMM is based on the Crank–Nicolson's algorithm. Even in the semi-implicit form, these algorithms break the curse of the time step limitation and allow using relatively large time steps. However, they suffer from the numerical heating/cooling related to the FGI and caused by the lack of energy conservation. Although this problem appears to be less acute compared to the explicit PIC and the implicit methods allow adjusting the amount of numerical error in the energy conservation (by varying the θ parameter used to mix the old and the new electric field values in the equations of motion and field equations), the FGI still plagues self-consistent simulations of large plasmas with high densities, where the cell size can become significantly larger than the Debye length. Nevertheless, the DIM was used in the codes EDIPIC,[142] LSP,[362] and Warp[363] employed for simulations relevant to EP,[364–366] and in other codes (e.g., Ref. 367). The IMM was used in Ref. 368 to model an SPT-type HT.

Recently, it was realized that if the IMM equations are implemented in their original form exactly (without the linearization), and if the functions used for the current density assignment and the electric field interpolation are the same, then for $\theta = 0.5$ they can conserve energy exactly, i.e., to a desired accuracy in a controllable way[67,157] (see also a discussion of the algorithm usage for the modeling of technological plasmas featuring electrodes and reactor walls, external networks, and collisions in Ref. 69). Key ingredients for the energy conservation were the electric field update with Ampère's law even in the case of electrostatic simulations[67,69] and employing the same interpolation function for the electric field and current density calculations. It turned out that such energy-conserving PIC (ECPIC) algorithms have a different domain of parameters where the FGI is triggered compared to the momentum-conserving schemes.[155] Whereas the latter trigger the FGI if the Debye length is not resolved by the cell size, the former suffer from the FGI only if the average electron drift exceeds the electron thermal velocity (note, however, that such a study was never conducted for magnetized plasmas). The FGI manifests itself differently

in the energy- and momentum-conserving PIC codes. Due to the corresponding conservation properties, it can lead to the non-physical conversion of the momentum of a directed motion in the former[369] and the excessive numerical heating in the latter.[370] When the FGI is not excited, the momentum (energy) is typically conserved to a tolerable accuracy in the energy-(momentum-) conserving PIC algorithm. Furthermore, such accuracy can be improved with subcycling in the orbit integration, which is also required to ensure the charge conservation in case the latter is needed.[67] The absence of numerical heating and the FGI stability properties of the energy-conserving PIC implicit schemes enables them to be a very efficient tool in combination with non-uniform mapped grids[371] or with unstructured finite elements.[372] If the energy-conserving schemes are not used for these cases, one needs to ensure that the FGI stability criterion is fulfilled, which might be difficult in a simulation with cell sizes sometimes varying over a few orders of magnitude. If the energy-conserving schemes are employed, there are no strict limitations on the cell size, and it should be chosen so that the desired spatial scales of interest are resolved in the corresponding areas. In this way, one can use more grid points where fine-scale phenomena are expected (e.g., in the plasma sheaths, which can be very small in high-density plasmas) and fewer points where essential physics occurs on larger scales (e.g., in the plasma bulk). The resulting computational grid would be much smaller compared to that required by the explicit PIC algorithm, whereas all important phenomena would be captured. The speed-up provided by such a technique can be large (more so in multi-dimensional simulations) and can be decisive in making the corresponding simulations tractable. This effect is enhanced by the absence of a time step stability limit in the implicit algorithms as well. It might seem problematic to use large time steps when the resolution of electron cyclotron rotation in the presence of a magnetic field is not needed, but the corresponding orbit integration algorithms have also been developed.[391]

The fully implicit methods need an iterative procedure to make the field and the particle updates consistent over the time step. The system solved has the dimensionality defined by the field grid, since the current density can be calculated from the updated particle positions and velocities if the current iteration for the new electric field values at the grid is known. This is referred to as the "particle enslavement."[67,157] A modern option for the iterative procedure is the Jacobian-free Newton–Krylov method,[67] which is economical in terms of memory space and can be accelerated by using physics-based preconditioners.[175] Alternatively, one can use the semi-implicit energy-conserving (ECSIM) algorithm recently proposed in Ref. 373 (see also Ref. 374). If time steps comparable to the plasma period are desired, another option might be to use the explicit Lewis's algorithm[375] based on the variational principle and conserving energy in the limit of a vanishing time step. According to Ref. 155, this scheme should have FGI-related properties similar to the implicit or semi-implicit energy-conserving schemes. However, so far, there have been no explicit demonstrations in the literature of this scheme capability to simulate high density plasmas.

In modeling the plasma processing discharges, implicit energy-conserving PIC methods were already used to simulate ICP,[154] RF magnetron,[135,136,376] and VHF CCP[70] plasmas and demonstrated good numerical properties. The ECCOPIC code employed in Refs. 70, 135, 136 and 376 was verified in an international HT-related benchmark involving several codes[107] and validated with experimental data,[70,376] demonstrating the method's functionality. Another work in this perspective direction indicating a plan to target specifically the EP applications is presented in Ref. 372.

3. Reduced dimensional order method

A novel approach[377,378] has been recently introduced for ES PIC. It consists in approximating (with the limit of an absence of mathematical justification) the 2D potential field $\phi(x, y)$ in terms of a superimposition of 1D potential fields along the x and y directions

$$\phi(x, y) = \chi(x) + \eta(y). \tag{21}$$

This allows substituting the solution of the 2D Poisson's equation with a system of two decoupled 1D Ordinary Differential Equations (ODEs) for the functions $\chi(x)$ and $\eta(y)$. It effectively corresponds to solve in-parallel two 1D PIC simulations along the x and y coordinates with the simulations sharing the same macro-particles. Therefore, the total number of required macro-particles is essentially in the same order as in a 1D simulation and hence the computational cost, allowing to reduce the number of cells and the required total number of macro-particles from $O(N^d)$ to $O(dN)$, with N being the number of cells along each direction, and d the number of dimensions.

This is done by decomposing into multiple rectangular (represented in Fig. 19 for a 2D case) or cubic (for 3D simulations) "regions," which can be thought of as the discretization of the domain using a "coarse grid." Next, within any specific region, each simulation dimension is separately discretized using 1D "elongated" cells with the size criterion (applying to the smaller side of the rectangle) being the same as that in a conventional 1D PIC (i.e., smaller than the Debye length). This fine-discretization step yields a decoupling between the different coordinates in each region, allowing to reduce the number of cells and, hence, the required total number of macroparticles as anticipated above.

The accuracy and the computational cost of a reduced-order simulation depend on the fineness of the coarse grid, i.e., the number of regions to be used, which is problem-dependant. The pseudo-2D PIC scheme was shown to capture the multi-dimensional plasma phenomena in all 2D configurations relevant to a HT, i.e., axial–azimuthal, azimuthal–radial, and axial–radial[377–381] with relatively few regions used, showing a computational speed-up with respect to a 2D simulation up to 50. The method can be promising to reduce the full 3D picture into a 2D model making the full dimensional kinetic representation of HTs affordable. In fact, the expected speed-up for a quasi-3D simulation with respect to the corresponding classical full-3D one is about 2500.

D. Deep learning-based particle-in-cell method

The next generation of PIC models can be integrated with Machine-Learning (ML) and Deep-Learning (DL) algorithms to assist in calculating the electric and magnetic fields from the charged particle phase space, thus bypassing the Maxwell's equations solvers (Poisson's solver for the ES case).

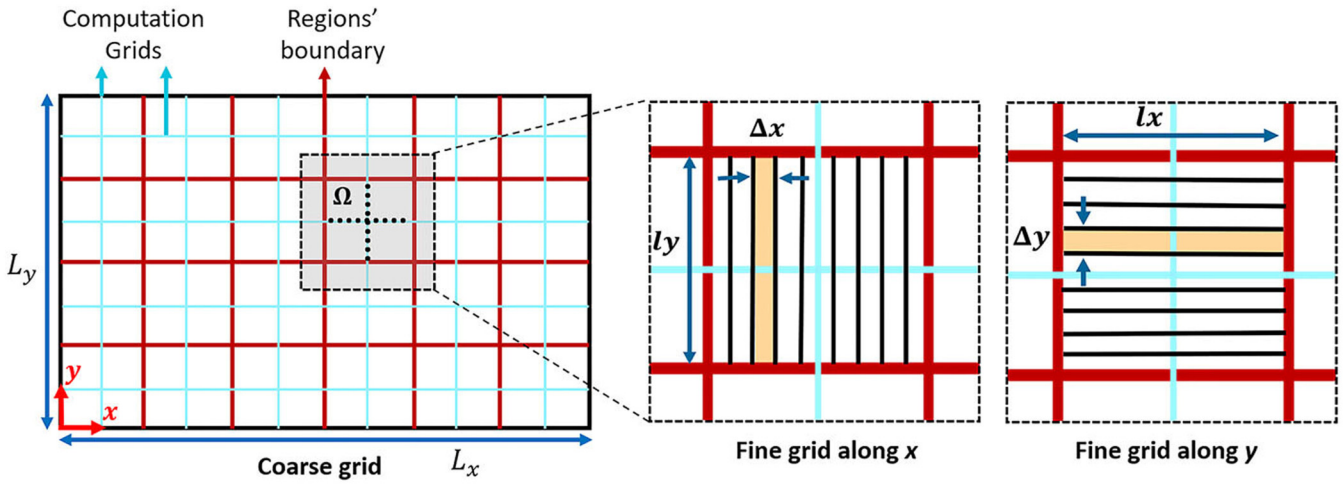

FIG. 19. Schematic of the domain decomposition corresponding to the reduced-order PIC scheme: (left) decomposition into multiple "regions" using a coarse grid; (right) 1D computational cells for the discretization of each region along the *x* and *y* directions. The red lines indicate the boundaries of the regions, and the blue lines represent the computational grids along the *x* and *y* directions in each region. Reproduced with permission from Faraji *et al.*, AIP Adv. **13**, 025315 (2023). Copyright 2023 AIP Publishing LLC.

In fact, ML and DL methods have emerged as valuable tools for data analysis and to replace or complement more traditional computational approaches. An example of such efforts is the development of DL-based pre-conditioners and linear solvers,[382] heterogeneous linear solvers for Partial Differential Equations,[383] use of DL-based methods in Computational Fluid Dynamics (CFD) solvers,[384] or weather forecasting.[385]

Recently,[386] a methodology to embed a DL electric field solver into an explicit PIC method has been developed and applied to the two-stream instability. The DL electric field solver is trained using the particle phase space information and its associated electric field. The DL-based PIC method replaces then the interpolation step for the charge calculations and electric field solver of the traditional PIC method with two new steps: an interpolation of particle velocity and position into a phase space grid and a DL electric field solver that is the result of a DL neural network training. In this regard, several choices are possible: Multilayer Perceptron (MLP), Convolutional Neural Network (CNN), or Residual Network (ResNet), among others. In order to train the DL electric field solver, a training data set, formed by the phase space grid and the associated electric field has been produced by running highly accurate traditional PIC simulations.

An ML algorithm[387,388] has been developed to fit the anomalous electron collisional frequency in HT to be used in the generalized Ohm's law for creating predictive hybrid models. Particle simulations could be used to train these models. The DL algorithm ultimately yields the following functional forms for the anomalous frequency

$$\nu_{ano} \propto \omega_{c,e}\left(\frac{u_i}{v_{d,e}}\right)^2, \tag{22}$$

demonstrating the importance of the electron $\boldsymbol{E} \times \boldsymbol{B}$ drift $v_{d,e}$ as the driving source for the onset of the turbulence and the ion drift speed u_i as its main saturation mechanism.

Finally, data-driven techniques have been applied to the analysis of numerical model[389] and experimental[390] results of HTs enabling the isolation of different mode oscillations.

VI. CONCLUSIONS

This Perspective paper has outlined the efforts in developing particle-based models for the different electric propulsion concepts with the latest sophisticated multi-dimensional simulations. The different electrostatic and electromagnetic schemes of the PIC/Monte Carlo method have been presented. The modular nature of the PIC method has enabled the introduction of a vast variety of physical phenomena, thus contributing to a realistic representation of an electric thruster: the interaction between the electromagnetic/electrostatic fields and the charged particles leading to electron heating and ion acceleration, the plasma–gas coupling, which is crucial in low pressure devices characterized by a high ionization degree, and, finally, the different surface processes representing not only a particle energy loss term but also a source/recycling term. These mechanisms have all been discussed and the different dedicated algorithms presented. Moreover, an outline of the current particle simulations methodology for plasma plume expansion and interaction with the satellite has been provided covering different topics such as hybrid vs full-PIC simulation approaches, circuit models for plasma–satellite interaction, and methods to assess the plume-electromagnetic compatibility.

An overview of the challenges, whose solutions will help push forward the boundaries of particle simulations in electric propulsion, has finally been presented. One of them is the availability of a collisional database for complex plasma chemistry (alternative propellants, more complete representation of molecular vibrational

and metastable kinetics) and the associated issue of a self-consistent simulation of the neutral gas phase in a affordable manner. The constantly increasing cost of high fidelity simulations then urges the adaptation of all codes to HPC techniques, such as the hybrid OpenMP-MPI parallelization for CPU-based architectures, and massive GPU parallelization, possibly combined with MPI to further boost performance. Apart from HPC techniques, the feasibility of simulations will also depend on new methods to reduce their computational cost, such as the sparse-grid method, the novel implicit/semi-implicit energy-conserving PIC models, or the reduced dimensional order methods. To conclude, the possibility of integrating future PIC simulations with Machine-Learning algorithms has also been thoroughly discussed.

In addition to presenting the state of the art of simulations and their related algorithms, this Perspectives paper has also addressed the main open research points and criticalities, related to the different treated topics.

Regarding ES electro-spray thrusters, a major point to be addressed in future work is the droplet formation, which can enable more precise injection conditions for PIC models of the extraction and acceleration process. Electrostatic gridded ion engines, on the other hand, still lack a comprehensive simulation of both the internal discharge chamber and the ion beamlet formation/coalescence process, a possible solution being to combine a full-PIC simulation of the former and a hybrid simulation of the latter. In $\boldsymbol{E} \times \boldsymbol{B}$ thrusters, the main open point is that of the full characterization of the anomalous transport, through instabilities such as the electron cyclotron drift, modified two-stream, ion transit time, or gradient drift (modified Simon–Hoh, lower-hybrid, or ion-sound) instability, sometimes also leading to the emergence of large-scale self-organized structures such as rotating spokes, or through complex near-wall conductivity effects, coupled with secondary electron emission processes.

Concerning EM thrusters, a full simulation retaining all terms in the coupled Maxwell–Newton system evolved in the time domain remains elusive for high plasma density devices with realistic sizes, although it is rapidly becoming feasible with modern high performance super-computing clusters featuring heterogeneous CPU/GPU nodes and algorithms tolerating large time step and cell size. Above all, it would allow to secure a self-consistent description of the complicated power absorption mechanisms, which are essential to capture the entire discharge physics. Such mechanisms may involve nonlinear particle–wave interaction, mode conversion, parametric, and other instabilities, which are yet to be investigated. Although other aspects of EM thrusters, such as the physics of the plasma expansion in a magnetic nozzle, are less dependent on the fully electromagnetic treatment, an appropriate evaluation of the power absorption and ionization profiles is fundamental for making reliable quantitative assessments of the overall thruster efficiency.

Concerning the plasma plume expansion and interaction with the spacecraft, full-PIC simulations have started to emerge and highlight the deficiencies and limitations of hybrid particle models, most of the time based on the quasi-neutral assumption coupled with polytropic electron thermodynamics. This approach is clearly incapable of capturing both the complex electron cooling phenomena and the peripheral plasma behavior, which can strongly affect the production of slow charge-exchange ions constituting most of the ion backflow. Nevertheless, a complete full-PIC simulation coupled with a complex circuit model of the satellite is still a prerogative of hybrid models, and will require a great improvement of the existing code parallelization.

Regarding the omnipresent topic of the gas–wall and plasma–wall interaction, the main open issue here is the lack of accurate data at low impact energies for both the secondary electron emission and the ion sputtering yields, as well as the energy and angle distributions of the emitted particles (e.g., backscattered/true secondary electrons and sputtered atoms). In addition, it is also essential to characterize with dedicated experiments both the neutral reflection and ion recombination energy accommodation coefficients, which have demonstrated to have a non-negligible influence on the propellant utilization efficiency of certain thrusters, and, more in general, on the distribution of plasma and gas bulk properties.

Continuing on the line of elementary processes data, it is necessary to acquire more detailed data, such as differential cross sections (for the scattering angle in elastic collisions and for the energy of secondary electrons in ionization events), vibrational state selective (for molecular propellants) and ionization state selective (e.g., for metastable states) cross sections. The existence of metastable states, in fact, might represent an important contribution to the overall ionization process.

In order to tackle the problem of the ever-growing computational cost of electric propulsion simulations, HPC techniques have begun to emerge that take advantage of heterogeneous multi-core CPU/GPU hardware on computing nodes of the most modern HPC clusters. The fast development of GPU hardware and software offers a lot of new perspectives concerning code parallelization. The development of novel algorithms benefiting from the large intra- and inter-GPU memory bandwidth and employing various reduced-precision units in mixed-precision algorithms is an interesting direction to go.

Additionally, one can cut computational costs by employing novel numerical techniques. One of the corresponding options is to use algorithms tolerating large time steps and/or large cell sizes. In this respect, the energy-conserving implicit or semi-implicit methods appear to be particularly promising, especially for multi-dimensional simulations. Another interesting technique is the Sparse PIC approach, which offers unquestionable advantages in terms of footprint memory, thanks to the smaller number of macro-particles for the same statistical error as in standard PIC methods, as well as a reduced size of mesh-related arrays. Finally, very recent works have demonstrated the capabilities of a new technique, known as "reduced dimensional order" method, which decouples the local field solution along the coordinate directions, and could yield total speed-ups in the order of 10^3 in the most time consuming 3D scenarios.

The combination of plasma propulsion and particle-based models has already proven to be very effective, representing an excellent example in which computational physics can fully express its potential. Thus, we expect that, in the next few years, PIC/MCC models will open up new scenarios in understanding physics-based questions related to electric propulsion and, as a consequence, in the development of more efficient thrusters, with a particular

attention to the study of lower and higher power levels and to the use of alternative propellants. Our opinion is that the wide variety of available algorithms and models in the PIC/MCC technique, the availability of new and more detailed data on volume and surface elementary processes, and the growing performance of computational platforms will together pave the way for the full numerical optimization and design of plasma thrusters.

ACKNOWLEDGMENTS

This material was based upon work supported by the Italian Ministry of University and Research (MUR) under the project PON "CLOSE to the Earth," No. ARS01–00141; F.T. and F.C. acknowledge fruitful discussions with P. Minelli, D. Bruno, V. Laporta, and J. Zhou. Part of F.C.'s work was completed while he was affiliated with ISTP-CNR. D.E. appreciates fruitful discussions with P. Parodi and R. Rakhimov. G.F and L.G acknowledge the access to the HPC resources of the CALMIP supercomputing center under the allocation 2013-P1125; G.F and L.G are very grateful to their colleagues J. P. Boeuf, G. Hagelaar, S. Tsikata, and S. Mazouffre for intense and fruitful discussions.

AUTHOR DECLARATIONS

Conflict of Interest

The authors have no conflicts to disclose.

Author Contributions

All authors have contributed to both original draft writing and review of this Perspectives paper.

F. Taccogna: Conceptualization (lead); Data curation (equal); Formal analysis (equal); Investigation (equal); Methodology (equal); Software (equal); Supervision (lead); Validation (equal); Visualization (equal); Writing – original draft (equal); Writing – review & editing (equal). **F. Cichocki:** Conceptualization (equal); Data curation (equal); Formal analysis (equal); Investigation (equal); Methodology (equal); Software (equal); Validation (equal); Visualization (equal); Writing – original draft (equal); Writing – review & editing (equal). **D. Eremin:** Data curation (equal); Formal analysis (equal); Investigation (equal); Methodology (equal); Software (equal); Validation (equal); Visualization (equal); Writing – original draft (equal); Writing – review & editing (equal). **G. Fubiani:** Data curation (equal); Formal analysis (equal); Investigation (equal); Methodology (equal); Software (equal); Validation (equal); Visualization (equal); Writing – original draft (equal); Writing – review & editing (equal). **L. Garrigues:** Data curation (equal); Formal analysis (equal); Investigation (equal); Methodology (equal); Software (equal); Validation (equal); Visualization (equal); Writing – original draft (equal); Writing – review & editing (equal).

DATA AVAILABILITY

The data that support the findings of this study are available from the corresponding author upon reasonable request.

REFERENCES

[1]E. Ahedo, "Plasmas for space propulsion," Plasma Phys. Control. Fusion **53**, 124037 (2011).
[2]S. Mazouffre, "Electric propulsion for satellites and spacecraft: Established technologies and novel approaches," Plasma Sources Sci. Technol. **25**, 033002 (2016).
[3]D. Lev, R. M. Myers, K. M. Lemmer, J. Kolbeck, H. Koizumi, and K. Polzin, "The technological and commercial expansion of electric propulsion," Acta Astronaut. **159**, 213–227 (2019).
[4]B. Jorns and T. Lafleur, "Foundations of plasmas as ion sources," Plasma Sources Sci. Technol. **32**, 014001 (2023).
[5]C. K. Birdsall and A. B. Langdon, *Plasma Physics via Computer Simulation* (Taylor and Francis, New York, 2005).
[6]G. A. Bird, *The DSMC Method* (CreateSpace Independent Publishing Platform, New York, 2013).
[7]M. Andrenucci, L. Biagioni, S. Marcuccio, and F. Paganucci, "Fundamental scaling laws for electric propulsion concepts," in *28th International Electric Propulsion Conference, IEPC 2003-1721* (Electric Rocket Propulsion Society, 2003).
[8]K. Holste, P. Dietz, S. Scharmann, K. Keil, T. Henning, D. Zschätzsch, M. Reitemeyer, B. Nauschütt, F. Kiefer, F. Kunze, J. Zorn, C. Heiliger, N. Joshi, U. Probst, R. Thüringer, C. Volkmar, D. Packan, S. Peterschmitt, K. T. Brinkmann, H.-G. Zaunick, M. H. Thoma, M. Kretschmer, H. J. Leiter, S. Schippers, K. Hannemann, and P. J. Klar, "Ion thrusters for electric propulsion: Scientific issues developing a niche technology into a game changer," Rev. Sci. Instrum. **91**, 061101 (2020).
[9]V. V. Zhurin, H. R. Kaufman, and R. S. Robinson, "Physics of closed drift thrusters," Plasma Sources Sci. Technol. **8**, R1 (1999).
[10]D. Goebel and I. Katz, "Hall thrusters," in *Fundamentals of Electric Propulsion* (John Wiley & Sons Ltd., 2008), pp. 325–392.
[11]J.-P. Boeuf, "Tutorial: Physics and modeling of Hall thrusters," J. Appl. Phys. **121**, 011101 (2017).
[12]Y. Raitses and N. J. Fisch, "Parametric investigations of a nonconventional Hall thruster," Phys. Plasmas **8**, 2579–2586 (2001).
[13]G. Kornfeld, N. Koch, and G. Coustou, "The highly efficient multistage plasma (HEMP) thruster, a new electric propulsion concept derived from tube technology," in *4th IEEE International Conference on Vacuum Electronics, 2003* (IEEE, 2003), pp. 3–4.
[14]N. A. MacDonald, M. A. Cappelli, S. R. Gildea, M. Martinez-Sanchez, and W. A. Hargus, "Laser-induced fluorescence velocity measurements of a diverging cusped-field thruster," J. Phys. D: Appl. Phys. **44**, 295203 (2011).
[15]D. Lev, R. Eytan, G. Alon, A. Warshavsky, L. Appel, A. Kapulkin, and M. Rubanovych, "The development of CAM200—Low power Hall thruster," Trans. Jpn. Soc. Aeronaut. Space Sci. Aerosp. Technol. Jpn. **14**, 217–223 (2016).
[16]C. Huang, J. Li, and M. Li, "Performance measurement and evaluation of an ionic liquid electrospray thruster," Chin. J. Aeronaut. **36**, 1–15 (2021).
[17]M. Keidar and I. I. Beilis, "Plasma in space propulsion," in *Plasma Engineering*, 2nd ed., edited by M. Keidar and I. I. Beilis (Academic Press, 2018), Chap. 5, pp. 213–363.
[18]D. O'Reilly, G. Herdrich, and D. F. Kavanagh, "Electric propulsion methods for small satellites: A review," Aerospace **8**, 22 (2021).
[19]Y. Takao, N. Kusaba, K. Eriguchi, and K. Ono, "Two-dimensional particle-in-cell Monte Carlo simulation of a miniature inductively coupled plasma source," J. Appl. Phys. **108**, 093309 (2010).
[20]R. Henrich, "Development of a plasma simulation tool for radio frequency ion thrusters," Ph.D. dissertation (Department of French, Physikalisches Institut Justus-Liebig-Universität Giessen, 2013).
[21]L. Dubois, F. Gaboriau, L. Liard, D. Harribey, C. Henaux, L. Garrigues, G. J. M. Hagelaar, S. Mazouffre, C. Boniface, and J. P. Boeuf, "ID-HALL, a new double stage Hall thruster design. I. Principle and hybrid model of ID-HALL," Phys. Plasmas **25**, 093503 (2018).
[22]K. Polzin, A. Martin, J. Little, C. Promislow, B. Jorns, and J. Woods, "State-of-the-art and advancement paths for inductive pulsed plasma thrusters," Aerospace **7**, 105 (2020).

[23]K. Emoto, K. Takahashi, and Y. Takao, "Density profile transition and high-energy electron transport in a magnetically expanding radio frequency plasma," Phys. Plasmas **30**, 013509 (2023).
[24]K. Takahashi, "Helicon-type radiofrequency plasma thrusters and magnetic plasma nozzles," Rev. Mod. Plasma Phys. **3**, 2367–3192 (2019).
[25]F. Cannat, T. Lafleur, J. Jarrige, P. Chabert, P.-Q. Elias, and D. Packan, "Optimization of a coaxial electron cyclotron resonance plasma thruster with an analytical model," Phys. Plasmas **22**, 053503 (2015).
[26]Y. Takao, H. Koizumi, K. Komurasaki, K. Eriguchi, and K. Ono, "Three-dimensional particle-in-cell simulation of a miniature plasma source for a microwave discharge ion thruster," Plasma Sources Sci. Technol. **23**, 06400 (2014).
[27]A. Sánchez-Villar, J. Zhou, E. Ahedo, and M. Merino, "Coupled plasma transport and electromagnetic wave simulation of an ECR thruster," Plasma Sources Sci. Technol. **30**, 045005 (2021).
[28]C. S. Olsen, M. G. Ballenger, M. D. Carter, F. R. C. Díaz, M. Giambusso, T. W. Glover, A. V. Ilin, J. P. Squire, B. W. Longmier, E. A. Bering, and P. A. Cloutier, "Investigation of plasma detachment from a magnetic nozzle in the plume of the VX-200 magnetoplasma thruster," IEEE Trans. Plasma Sci. **43**, 252–268 (2015).
[29]G. Krulle, M. Auweter-Kurtz, and A. Sasoh, "Technology and application aspects of applied field magnetoplasmadynamic propulsion," J. Propul. Power **14**, 754–763 (1998).
[30]J. Li, Y. Zhang, J. Wu, Y. Cheng, and X. Du, "Particle simulation model for self-field magnetoplasmadynamic thruster," Energies **12**, 1579 (2019).
[31]J. S. Snyder, G. Lenguito, J. D. Frieman, T. W. Haag, and J. A. Mackey, "Effects of background pressure on SPT-140 Hall thruster performance," J. Propul. Power **36**, 668–676 (2020).
[32]T. Andreussi, E. Ferrato, and V. Giannetti, "A review of air-breathing electric propulsion: From mission studies to technology verification," J. Electr. Propul. **1**, 31 (2022).
[33]F. Cichocki, A. Domínguez-Vázquez, M. Merino, and E. Ahedo, "Hybrid 3D model for the interaction of plasma thruster plumes with nearby objects," Plasma Sources Sci. Technol. **26**, 125008 (2017).
[34]S. J. Araki, "Multiscale coupling of spacecraft charging model with electric propulsion plume simulation," IEEE Trans. Plasma Sci. **47**, 4898–4908 (2019).
[35]E. Ahedo, "Using electron fluid models to analyze plasma thruster discharges," J. Electr. Propul. **2**, 2 (2023).
[36]H. Vincenti, M. Lobet, R. Lehe, J.-L. Vay, and J. Deslippe, "IC codes on the road to exascale architectures," in *Exascale Scientific Applications*, 1st ed., edited by T. J. W. Tjerk, P. Straatsma, and K. B. Antypas (Chapman and Hall/CRC, 2017), Chap. 7, p. 34.
[37]H. Liu, B. Wu, D. Yu, Y. Cao, and P. Duan, "Particle-in-cell simulation of a Hall thruster," J. Phys. D: Appl. Phys. **43**, 165202 (2010).
[38]J. Szabo, N. Warner, M. Martinez-Sanchez, and O. Batishchev, "Full particle-in-cell simulation methodology for axisymmetric Hall effect thrusters," J. Propul. Power **30**, 197–208 (2014).
[39]F. Taccogna and P. Minelli, "Three-dimensional particle-in-cell model of Hall thruster: The discharge channel," Phys. Plasmas **25**, 061208 (2018).
[40]T. S. Qingkai Kong and A. M. Bayen, *Python Programming and Numerical Methods. A Guide for Engineers and Scientists* (Elsevier Academic Press, 2021).
[41]E. Carbone, W. Graef, G. Hagelaar, D. Boer, M. M. Hopkins, J. C. Stephens, B. T. Yee, S. Pancheshnyi, J. van Dijk, and L. Pitchford, "Data needs for modeling low-temperature non-equilibrium plasmas: The LXCat project, history, perspectives and a tutorial," Atoms **9**, 16 (2021).
[42]R. Gueroult, G. Fubiani, and L. Garrigues, "Pitfalls in modeling walls and neutrals physics in gas discharges using parallel particle-in-cell Monte Carlo collision algorithms," Front. Phys. **6**, 128 (2018).
[43]*Plasma Modeling*, 2nd ed., edited by G. Colonna and A. D'Angola (IOP Publishing, 2022), pp. 2053–2563.
[44]M. M. Turner, "Kinetic properties of particle-in-cell simulations compromised by Monte Carlo collisions," Phys. Plasmas **13**, 033506 (2006).
[45]F. Riva, C. F. Beadle, and P. Ricci, "A methodology for the rigorous verification of particle-in-cell simulations," Phys. Plasmas **24**, 055703 (2017).
[46]A. Tavassoli, O. Chapurin, M. Jimenez, M. Papahn Zadeh, T. Zintel, M. Sengupta, L. Couëdel, R. J. Spiteri, M. Shoucri, and A. Smolyakov, "The role of noise in PIC and Vlasov simulations of the Buneman instability," Phys. Plasmas **28**, 122105 (2021).
[47]M. Vass, P. Palla, and P. Hartmann, "Revisiting the numerical stability/accuracy conditions of explicit PIC/MCC simulations of low-temperature gas discharges," Plasma Sources Sci. Technol. **31**, 064001 (2022).
[48]R. W. Hockney and J. W. Eastwood, *Computer Simulation Using Particles* (Hilger, Bristol, 1988).
[49]D. Tskhakaya, K. Matyash, R. Schneider, and F. Taccogna, "The particle-in-cell method," Contrib. Plasma Phys. **47**, 563–594 (2007).
[50]L. Brieda, *Plasma Simulations by Example* (CRC Press, Boca Raton, FL, 2010).
[51]Z. Donkó, A. Derzsi, M. Vass, B. Horváth, S. Wilczek, B. Hartmann, and P. Hartmann, "eduPIC: An introductory particle based code for radio-frequency plasma simulation," Plasma Sources Sci. Technol. **30**, 095017 (2021).
[52]O. Buneman, "Dissipation of currents in ionized media," Phys. Rev. **115**, 503–517 (1959).
[53]J. Dawson, "One–dimensional plasma model," Phys. Fluids **5**, 445–459 (1962).
[54]H. R. Skullerud, "The stochastic computer simulation of ion motion in a gas subjected to a constant electric field," J. Phys. D: Appl. Phys. **1**, 1567 (1968).
[55]S. L. Lin and J. N. Bardsley, "Monte Carlo simulation of ion motion in drift tubes," J. Chem. Phys. **66**, 435–445 (1977).
[56]Y. Sakai, H. Tagashira, and S. Sakamoto, "The development of electron avalanches in argon at high E/N values. I. Monte Carlo simulation," J. Phys. D: Appl. Phys. **10**, 1035 (1977).
[57]L. C. Pitchford and A. V. Phelps, "Comparative calculations of electron-swarm properties in N_2 at moderate $\frac{E}{N}$ values," Phys. Rev. A **25**, 540–554 (1982).
[58]J. P. Boeuf and E. Marode, "A Monte Carlo analysis of an electron swarm in a nonuniform field: The cathode region of a glow discharge in helium," J. Phys. D: Appl. Phys. **15**, 2169 (1982).
[59]C. Birdsall, "Particle-in-cell charged-particle simulations, plus Monte Carlo collisions with neutral atoms, PIC-MCC," IEEE Trans. Plasma Sci. **19**, 65–85 (1991).
[60]K. Nanbu, "Probability theory of electron-molecule, ion-molecule, molecule-molecule, and Coulomb collisions for particle modeling of materials processing plasmas and cases," IEEE Trans. Plasma Sci. **28**, 971–990 (2000).
[61]K. Komurasaki and Y. Arakawa, "Two-dimensional numerical model of plasma flow in a Hall thruster," J. Propul. Power **11**, 1317–1323 (1995).
[62]C. Lenz and M. Martinez-Sanchez, "Transient one dimensional numerical simulation of Hall thrusters," AIAA Paper No. 93-2491, 1993.
[63]J. Fife, "Hybrid-PIC modeling and electrostatic probe survey of Hall thrusters," Ph.D. thesis (Massachusetts Institute of Technology, 1998).
[64]L. Garrigues, A. Heron, J. C. Adam, and J. P. Boeuf, "Hybrid and particle-in-cell models of a stationary plasma thruster," Plasma Sources Sci. Technol. **9**, 219 (2000).
[65]K. Nanbu, "Direct simulation scheme derived from the Boltzmann equation. I. Monocomponent gases," J. Phys. Soc. Jpn. **49**, 2042–2049 (1980).
[66]V. Serikov, S. Kawamoto, and K. Nanbu, "Particle-in-cell plus direct simulation Monte Carlo (PIC-DSMC) approach for self-consistent plasma-gas simulations," IEEE Trans. Plasma Sci. **27**, 1389–1398 (1999).
[67]G. Chen, L. Chacón, and D. C. Barnes, "An energy- and charge-conserving, implicit, electrostatic particle-in-cell algorithm," J. Comput. Phys. **230**, 7018 (2011).
[68]G. Chen and L. Chacón, "A multi-dimensional, energy- and charge-conserving, nonlinearly implicit, electromagnetic Vlasov–Darwin particle-in-cell algorithm," Comput. Phys. Commun. **197**, 73 (2015).
[69]D. Eremin, "An energy- and charge-conserving electrostatic implicit particle-in-cell algorithm for simulations of collisional bounded plasmas," J. Comput. Phys. **452**, 110934 (2022).
[70]D. Eremin, E. Kemaneci, M. Matsukuma, T. Mussenbrock, and R. P. Brinkmann, "Modeling of very high frequency large-electrode capacitively

coupled plasmas with a fully electromagnetic particle-in-cell code," Plasma Sources Sci. Technol. **32**, 044007 (2023).
[71]V. Vahedi and M. Surendra, "A Monte Carlo collision model for the particle-in-cell method: Applications to argon and oxygen discharges," Comput. Phys. Commun. **87**, 179–198 (1995).
[72]L. Garrigues, S. Mazouffre, and G. Bourgeois, "Computed versus measured ion velocity distribution functions in a Hall effect thruster," J. Appl. Phys. **111**, 113301 (2012).
[73]P. R. Amestoy, I. S. Duff, J.-Y. L'Excellent, and J. Koster, "Mumps: A general purpose distributed memory sparse solver," in *Applied Parallel Computing. New Paradigms for HPC in Industry and Academia: 5th International Workshop, PARA 2000 Bergen, Norway, June 18–20, 2000* (Springer, 2001), pp. 121–130.
[74]O. Schenk and K. Gärtner, "Solving unsymmetric sparse systems of linear equations with PARDISO," Future Gener. Comput. Syst. **20**, 475–487 (2004).
[75]S. Balay, S. Abhyankar, M. Adams, J. Brown, P. R. Brune, K. Buschelman, L. Dalcin, A. Dener, V. Eijkhout, W. D. Gropp, D. Karpeyev, D. Kaushik, M. G. Knepley, D. A. May, L. C. McInnes, R. T. Mills, T. Munson, K. Rupp, P. Sanan, B. F. Smith, S. Zampini, H. Zhang, and H. Zhang, "PETSc users manual (revision 3.15)," Argonne National Laboratory, Technical Report ANL-21/39 - Revision 3.20, 2023.
[76]X. S. Li, "An overview of SuperLU: Algorithms, implementation, and user interface," ACM Trans. Math. Software **31**, 302–325 (2005).
[77]See https://computing.llnl.gov/projects/hypre-scalable-linear-solvers-multigrid-methods for "Hypre: Scalable Linear Solvers and Multigrid Methods" (2023) (last accessed June 30, 2023).
[78]F. Taccogna, F. Cichocki, and P. Minelli, "Coupling plasma physics and chemistry in the PIC model of electric propulsion: Application to an air-breathing, low-power Hall thruster," Front. Phys. **10**, 989 (2022).
[79]J. R. Nagel, "Numerical solutions to poisson equations using the finite-difference method [education column]," IEEE Antennas Propag. Mag. **56**, 209–224 (2014).
[80]F. Taccogna, S. Longo, M. Capitelli, and R. Schneider, "Self-similarity in Hall plasma discharges: Applications to particle models," Phys. Plasmas **12**, 053502 (2005).
[81]P. Coche and L. Garrigues, "A two-dimensional (azimuthal-axial) particle-in-cell model of a Hall thruster," Phys. Plasmas **21**, 023503 (2014).
[82]Y. J. Zhao, H. Liu, D. R. Yu, P. Hu, and H. Wu, "Particle-in-cell simulations for the effect of magnetic field strength on a cusped field thruster," J. Phys. D: Appl. Phys. **47**, 045201 (2013).
[83]D. Yongjie, P. Wuji, W. Liqiu, S. Guoshun, L. Hong, and Y. Daren, "Computer simulations of Hall thrusters without wall losses designed using two permanent magnetic rings," J. Phys. D: Appl. Phys. **49**, 465001 (2016).
[84]D. Kahnfeld, R. Heidemann, J. Duras, P. Matthias, G. Bandelow, K. Lüskow, S. Kemnitz, K. Matyash, and R. Schneider, "Breathing modes in HEMP thrusters," Plasma Sources Sci. Technol. **27**, 124002 (2018).
[85]K. Matyash, R. Schneider, S. Mazouffre, S. Tsikata, and L. Grimaud, "Rotating spoke instabilities in a wall-less Hall thruster: Simulations," Plasma Sources Sci. Technol. **28**, 044002 (2019).
[86]K. F. Lüskow, P. R. C. Neumann, G. Bandelow, J. Duras, D. Kahnfeld, S. Kemnitz, P. Matthias, K. Matyash, and R. Schneider, "Particle-in-cell simulation of the cathodic arc thruster," Phys. Plasmas **25**, 013508 (2018).
[87]W. Yang, Q. Sun, and Q. Zhou, "Particle modeling of vacuum arc discharges," J. Appl. Phys. **128**, 060905 (2020).
[88]Q. Liu, L. Yang, Y. Huang, X. Zhao, and Z. Zheng, "PIC simulation of plasma properties in the discharge channel of a pulsed plasma thruster with flared electrodes," Plasma Sci. Technol. **21**, 074005 (2019).
[89]P. Wang, A. Borner, Z. Li, and D. A. Levin, "Simulations of electrospray in a colloid thruster with a high resolution three-dimensional Particle-in-Cell model," AIAA Paper No. 2013-2629, 2013.
[90]T. Enomoto, S. M. Parmar, R. Yamada, R. E. Wirz, and Y. Takao, "Molecular dynamics simulations of ion extraction from nanodroplets for ionic liquid electrospray thrusters," J. Electr. Propul. **1**, 13 (2022).
[91]R. K. Narayanan and K. Madduri, "Parallel particle-in-cell performance optimization: A case study of electrospray simulation," in *2017 IEEE International Parallel and Distributed Processing Symposium Workshops (IPDPSW)* (IEEE, 2017), pp. 1158–1167.
[92]Y. Zhao and J. J. Wang, "A particle-particle simulation model for droplet acceleration in colloid thrusters," in *The 36th International Electric Propulsion Conference, University of Vienna, Austria, IEPC-2019-526* (Electric Rocket Propulsion Society, 2019).
[93]J. Perales-Díaz, F. Cichocki, M. Merino, and E. Ahedo, "Formation and neutralization of electric charge and current of an ion thruster plume," Plasma Sources Sci. Technol. **30**, 105023 (2021).
[94]F. Taccogna, P. Minelli, S. Longo, M. Capitelli, and R. Schneider, "Modeling of a negative ion source. III. Two-dimensional structure of the extraction region," Phys. Plasmas **17**, 063502 (2010).
[95]F. Taccogna, P. Minelli, P. Diomede, S. Longo, M. Capitelli, and R. Schneider, "Particle modelling of the hybrid negative ion source," Plasma Sources Sci. Technol. **20**, 024009 (2011).
[96]F. Taccogna, P. Minelli, and S. Longo, "Three-dimensional structure of the extraction region of a hybrid negative ion source," Plasma Sources Sci. Technol. **22**, 045019 (2013).
[97]F. Taccogna and P. Minelli, "PIC modeling of negative ion sources for fusion," New J. Phys. **19**, 015012 (2017).
[98]G. Fubiani, L. Garrigues, G. Hagelaar, N. Kohen, and J. P. Boeuf, "Modeling of plasma transport and negative ion extraction in a magnetized radio-frequency plasma source," New J. Phys. **19**, 015002 (2017).
[99]L. Garrigues and G. Fubiani, "Tutorial: Modeling of the extraction and acceleration of negative ions from plasma sources using particle-based methods," J. Appl. Phys. **133**, 041102 (2023).
[100]Y. Yamashita, R. Tsukizaki, Y. Yamamoto, D. Koda, K. Nishiyama, and H. Kuninaka, "Azimuthal ion drift of a gridded ion thruster," Plasma Sources Sci. Technol. **27**, 105006 (2018).
[101]H. Jian, Y. Chu, H. Cao, Y. Cao, X. He, and G. Xia, "Three-dimensional ife-pic numerical simulation of background pressure's effect on accelerator grid impingement current for ion optics," Vacuum **116**, 130–138 (2015).
[102]T. Binder, M. Pfeiffer, and S. Fasoulas, "Validation of grid current simulations using the particle-in-cell method for a miniaturized ion thruster," AIP Conf. Proc. **2132**, 040003 (2019).
[103]J. Polk, V. Chaplin, J. Anderson, J. Yim, G. Soulas, G. Williams, and R. Shastry, "Modeling grid erosion in the next ion thruster using the CEX2D and CEX3D codes," J. Electr. Propul. **2**, 14 (2023).
[104]G. J. M. Hagelaar, J. Bareilles, L. Garrigues, and J. P. Boeuf, "Two-dimensional model of a stationary plasma thruster," J. Appl. Phys. **91**, 5592–5598 (2002).
[105]M. Panelli, D. Morfei, B. Milo, F. A. D'Aniello, and F. Battista, "Axisymmetric hybrid plasma model for Hall effect thrusters," Particles **4**, 296–324 (2021).
[106]J. Perales-Díaz, A. Domínguez-Vázquez, P. Fajardo, E. Ahedo, F. Faraji, M. Reza, and T. Andreussi, "Hybrid plasma simulations of a magnetically shielded Hall thruster," J. Appl. Phys. **131**, 103302 (2022).
[107]T. Charoy, J. P. Boeuf, A. Bourdon, J. A. Carlsson, P. Chabert, B. Cuenot, D. Eremin, L. Garrigues, K. Hara, I. D. Kaganovich, A. T. Powis, A. Smolyakov, D. Sydorenko, A. Tavant, O. Vermorel, and W. Villafana, "2D axial-azimuthal particle-in-cell benchmark for low-temperature partially magnetized plasmas," Plasma Sources Sci. Technol. **28**, 105010 (2019).
[108]T. Charoy, T. Lafleur, A. A. Laguna, A. Bourdon, and P. Chabert, "The interaction between ion transit-time and electron drift instabilities and their effect on anomalous electron transport in Hall thrusters," Plasma Sources Sci. Technol. **30**, 065017 (2021).
[109]F. Petronio, T. Charoy, A. A. Laguna, A. Bourdon, and P. Chabert, "Two-dimensional effects on electrostatic instabilities in Hall thrusters. I. Insights from particle-in-cell simulations and two-point power spectral density reconstruction techniques," Phys. Plasmas **30**, 012103 (2023).
[110]V. Croes, T. Lafleur, Z. Bonaventura, A. Bourdon, and P. Chabert, "2D particle-in-cell simulations of the electron drift instability and associated anomalous electron transport in Hall-effect thrusters," Plasma Sources Sci. Technol. **26**, 034001 (2017).

[111]F. Taccogna, P. Minelli, Z. Asadi, and G. Bogopolsky, "Numerical studies of the E × B electron drift instability in Hall thrusters," Plasma Sources Sci. Technol. **28**, 064002 (2019).
[112]A. Tavant, V. Croes, R. Lucken, T. Lafleur, A. Bourdon, and P. Chabert, "The effects of secondary electron emission on plasma sheath characteristics and electron transport in an discharge via kinetic simulations," Plasma Sources Sci. Technol. **27**, 124001 (2018).
[113]J. P. Boeuf and L. Garrigues, "E × B electron drift instability in Hall thrusters: Particle-in-cell simulations vs theory," Phys. Plasmas **25**, 061204 (2018).
[114]T. Lafleur, R. Martorelli, P. Chabert, and A. Bourdon, "Anomalous electron transport in Hall-effect thrusters: Comparison between quasi-linear kinetic theory and particle-in-cell simulations," Phys. Plasmas **25**, 061202 (2018).
[115]J.-P. Boeuf, "Rotating structures in low temperature magnetized plasmas—Insight from particle simulations," Front. Phys. **2**, 74 (2014).
[116]T. Lafleur, S. D. Baalrud, and P. Chabert, "Theory for the anomalous electron transport in Hall effect thrusters. I. Insights from particle-in-cell simulations," Phys. Plasmas **23**, 053502 (2016).
[117]S. Janhunen, A. Smolyakov, O. Chapurin, D. Sydorenko, I. Kaganovich, and Y. Raitses, "Nonlinear structures and anomalous transport in partially magnetized E × B plasmas," Phys. Plasmas **25**, 011608 (2018).
[118]I. Katz, V. H. Chaplin, and A. Lopez Ortega, "Particle-in-cell simulations of Hall thruster acceleration and near plume regions," Phys. Plasmas **25**, 123504 (2018).
[119]Z. Asadi, F. Taccogna, and M. Sharifian, "Numerical study of electron cyclotron drift instability: Application to Hall thruster," Front. Phys. **7**, 140 (2019).
[120]T. Charoy, T. Lafleur, A. Tavant, P. Chabert, and A. Bourdon, "A comparison between kinetic theory and particle-in-cell simulations of anomalous electron transport in E × B plasma discharges," Phys. Plasmas **27**, 063510 (2020).
[121]S. Janhunen, A. Smolyakov, D. Sydorenko, M. Jimenez, I. Kaganovich, and Y. Raitses, "Evolution of the electron cyclotron drift instability in two-dimensions," Phys. Plasmas **25**, 082308 (2018).
[122]W. Villafana, F. Petronio, A. C. Denig, M. J. Jimenez, D. Eremin, L. Garrigues, F. Taccogna, A. Alvarez-Laguna, J. P. Boeuf, A. Bourdon, P. Chabert, T. Charoy, B. Cuenot, K. Hara, F. Pechereau, A. Smolyakov, D. Sydorenko, A. Tavant, and O. Vermorel, "2D radial-azimuthal particle-in-cell benchmark for E × B discharges," Plasma Sources Sci. Technol. **30**, 075002 (2021).
[123]F. Petronio, A. Tavant, T. Charoy, A. Alvarez Laguna, A. Bourdon, and P. Chabert, "Conditions of appearance and dynamics of the modified two-stream instability in E × B discharges," Phys. Plasmas **28**, 043504 (2021).
[124]M. Sengupta and A. Smolyakov, "Mode transitions in nonlinear evolution of the electron drift instability in a 2D annular E × B system," Phys. Plasmas **27**, 022309 (2020).
[125]F. Taccogna and L. Garrigues, "Latest progress in Hall thrusters plasma modelling," Rev. Mod. Plasma Phys. **3**, 12 (2019).
[126]K. Hara and S. Tsikata, "Cross-field electron diffusion due to the coupling of drift-driven microinstabilities," Phys. Rev. E **102**, 023202 (2020).
[127]K. Hara and C. Treece, "Ion kinetics and nonlinear saturation of current-driven instabilities relevant to hollow cathode plasmas," Plasma Sources Sci. Technol. **28**, 055013 (2019).
[128]P. Minelli and F. Taccogna, "How to build PIC-MCC models for Hall microthrusters," IEEE Trans. Plasma Sci. **46**, 219–224 (2017).
[129]I. D. Kaganovich, A. Smolyakov, Y. Raitses, E. Ahedo, I. G. Mikellides, B. Jorns, F. Taccogna, R. Gueroult, S. Tsikata, A. Bourdon, J.-P. Boeuf, M. Keidar, A. T. Powis, M. Merino, M. Cappelli, K. Hara, J. A. Carlsson, N. J. Fisch, P. Chabert, I. Schweigert, T. Lafleur, K. Matyash, A. V. Khrabrov, R. W. Boswell, and A. Fruchtman, "Physics of ExB discharges relevant to plasma propulsion and similar technologies," Phys. Plasmas **27**, 120601 (2020).
[130]W. Villafana, "Numerical particle-in-cell studies of Hall thrusters using unstructured grids," Ph.D. thesis (Université de Toulouse, 2021), unpublished thesis.
[131]W. Villafana, G. Fubiani, L. Garrigues, G. Vigot, B. Cuenot, and O. Vermorel, "3D particle-in-cell modeling of anomalous electron transport driven by the electron drift instability in Hall thrusters," in *The 37th International Electric Propulsion Conference, Massachusetts Institute of Technology, Cambridge, MA, USA, IEPC-2022-375* (Electric Rocket Propulsion Society, 2022).
[132]S. Tsikata, C. Honoré, N. Lemoine, and D. M. Grésillon, "Three-dimensional structure of electron density fluctuations in the Hall thruster plasma: E × B mode," Phys. Plasmas **17**, 112110 (2010).
[133]LANDMARK, see https://www.landmark-plasma.com/ for "Low Temperature Magnetized Plasma Benchmarks" (2017) (last accessed January 27, 2023).
[134]A. Anders, "Localized heating of electrons in ionization zones: Going beyond the Penning-Thornton paradigm in magnetron sputtering," Appl. Phys. Lett. **105**, 244104 (2014).
[135]D. Eremin, D. Engel, D. Krüger, S. Wilczek, B. Berger, M. Oberberg, C. Wölfel, A. I. Smolyakov, J. Lunze, and P. Awakowicz, "Electron dynamics in planar radio frequency magnetron plasmas: I. The mechanism of Hall heating and the μ-mode," Plasma Sources Sci. Technol. **32**, 045007 (2023).
[136]D. Eremin, B. Berger, D. Engel, J. Kallähn, K. Köhn, D. Krüger, L. Xu, M. Oberberg, C. Wölfel, J. Lunze, P. Awakowicz, J. Schulze, and R. P. Brinkmann, "Electron dynamics in planar radio frequency magnetron plasmas: II. Heating and energization mechanisms studied via a 2d3v particle-in-cell/Monte Carlo code," Plasma Sources Sci. Technol. **32**, 045008 (2023).
[137]N. S. Erokhin and S. S. Moiseev, "Problems of the theory of linear and nonlinear transformation of waves in inhomogeneous media," Sov. Phys. Usp. **16**, 64 (1973).
[138]A. Smolyakov, V. Godyak, and A. Duffy, "On nonlinear effects in inductively coupled plasmas," Phys. Plasmas **7**, 4755 (2000).
[139]K. Ostrikov, E. Tsakadze, S. Xu, S. V. Vladimirov, and R. Storer, "Nonlinear electromagnetic fields in 0.5 MHz inductively coupled plasmas," Phys. Plasmas **10**, 1146 (2003).
[140]J. L. Kline and E. E. Scime, "Parametric decay instabilities in the HELIX helicon plasma source," Phys. Plasmas **10**, 135 (2003).
[141]F. F. Chen, "Nonlinear effects and anomalous transport in RF plasmas," IEEE Trans. Plasma Sci. **34**, 718 (2006).
[142]D. Sydorenko, "Particle-in-cell simulations of electron dynamics in low pressure discharges with magnetic fields," Ph.D. thesis (University of Saskatchewan Saskatoon, 2006).
[143]J. Villasenor and O. Buneman, "Rigorous charge conservation for local electromagnetic field solvers," Comput. Phys. Commun. **69**, 306 (1992).
[144]T. Zh. Esirkepov, "Exact charge conservation scheme for particle-in-cell simulation with an arbitrary form-factor," Comput. Phys. Commun. **135**, 144 (2001).
[145]A. B. Langdon, "On enforcing Gauss' law in electromagnetic particle-in-cell codes," Comput. Phys. Commun. **70**, 447 (1992).
[146]K. Yee, "Numerical solution of initial boundary value problems involving Maxwell's equations in isotropic media," IEEE Trans. Antennas Propag. **14**, 302–307 (1966).
[147]J. Verboncoeur, A. Langdon, and N. Gladd, "An object-oriented electromagnetic PIC code," Comput. Phys. Commun. **87**, 199–211 (1995).
[148]A. Taflove and S. C. Hagness, *Computational Electrodynamics: The Finite-Difference Time-Domain Method* (Artech House Inc., 2005).
[149]G. Mur, "Absorbing boundary conditions for the finite-difference approximation of the time-domain electromagnetic-field equations," IEEE Trans. Electromagn. Compat. **23**, 377 (1981).
[150]J. P. Berenger, *Perfectly Matched Layer (PML) for Computational Electromagnetics* (Morgan & Claypool Publishers, 2007).
[151]A. Bayliss and E. Turkel, "Radiation boundary conditions for wavelike equations," Commun. Pure Appl. Math. **33**, 707 (1980).
[152]R. Alvarez and L. L. Alves, "Two-dimensional electromagnetic model of a microwave plasma reactor operated by an axial injection torch," J. Appl. Phys. **101**, 103303 (2007).
[153]S. Rahimi, M. Jimenez-Diaz, S. Hübner, E. H. Kemaneci, J. J. A. M. van der Mullen, and J. van Dijk, "A two-dimensional modelling study of a coaxial plasma waveguide," J. Phys. D: Appl. Phys. **47**, 125204 (2014).

[154]S. Mattei, K. Nishida, M. Onai, J. Lettry, M. Q. Tran, and A. Hatayama, "A fully-implicit particle-in-cell Monte Carlo collision code for the simulation of inductively coupled plasmas," J. Comput. Phys. **350**, 891 (2017).
[155]D. C. Barnes and L. Chacón, "Finite spatial-grid effects in energy-conserving particle-in-cell algorithms," Comput. Phys. Commun. **258**, 107560 (2021).
[156]M. D. Meyers, C.-K. Huanga, Y. Zenga, S. A. Yi, and B. J. Albright, "On the numerical dispersion of electromagnetic particle-in-cell code: Finite grid instability," J. Comput. Phys. **297**, 565 (2015).
[157]S. Markidis and G. Lapenta, "The energy conserving particle-in-cell method," J. Comput. Phys. **230**, 7037 (2011).
[158]K. Germaschewski, W. Fox, S. Abbott, N. Ahmadi, K. Maynard, L. Wang, H. Ruhl, and A. Bhattacharjee, "The plasma simulation code: A modern particle-in-cell code with patch-based load-balancing," J. Comput. Phys. **318**, 305 (2016).
[159]A. Pukhov, "Particle-in-cell codes for plasma-based particle acceleration," CERN Yellow Rep. **1**, 181 (2016).
[160]W. H. Koh, N. H. Choi, D. I. Choi, and Y. H. Oh, "Electromagnetic particle simulation of electron cyclotron resonance microwave discharge," J. Appl. Phys. **73**, 4205–4211 (1993).
[161]V. Gopinath and T. Grotjohn, "Three-dimensional electromagnetic PIC model of a compact ECR plasma source," IEEE Trans. Plasma Sci. **23**, 602–608 (1995).
[162]D. Pavarin, F. Ferri, M. Manente, D. Curreli, D. Melazzi, and D. Rondini, "Development of plasma codes for the design of mini-helicon thrusters," in *32nd International Electric Propulsion Conference, Wiesbaden, Germany, IEPC-2011-240* (Electric Rocket Propulsion Society, 2011).
[163]V. Olshansky, "Energy dissipation in helicon plasma at the near field of an antenna," Probl. At. Sci. Technol. **6**, 86 (2018).
[164]R. Jaafarian, A. Ganjovi, and G. Etaati, "Study of the operating parameters of a helicon plasma discharge source using PIC-MCC simulation technique," Phys. Plasmas **25**, 013510 (2018).
[165]J. Porto and P.-Q. Elias, "Axisymmetric electromagnetic wave propagation computation using the constrained interpolation profile scheme with large time steps," IEEE Trans. Antennas Propag. **69**, 4049 (2021).
[166]J. Porto and P.-Q. Elias, "Two-dimensional kinetic modeling of the power deposition in a coaxial ECR thruster," in *The 37th International Electric Propulsion Conference, Massachusetts Institute of Technology, Cambridge, MA, USA, IEPC-2022-503* (Electric Rocket Propulsion Society, 2022).
[167]J. Porto, P.-Q. Elias, and A. Ciardi, "Anisotropic electron heating in an electron cyclotron resonance thruster with magnetic nozzle," IEEE Trans. Antennas Propag. **69**, 4049 (2023).
[168]Y. Takao and K. Ono, "A miniature electrothermal thruster using microwave-excited plasmas: A numerical design consideration," Plasma Sources Sci. Technol. **15**, 211 (2006).
[169]T. Takahashi, Y. Takao, K. Eriguchi, and K. Ono, "Numerical and experimental study of microwave-excited microplasma and micronozzle flow for a microplasma thruster," Phys. Plasmas **16**, 083505 (2009).
[170]M. Magarotto, D. Melazzi, and D. Pavarin, "3D-VIRTUS: Equilibrium condition solver of radio-frequency magnetized plasma discharges for space applications," Comput. Phys. Commun. **247**, 106953 (2020).
[171]M. Magarotto, S. Di Fede, N. Souhair, S. Andrews, and F. Ponti, "Numerical suite for cathodeless plasma thrusters," Acta Astronaut. **197**, 126–138 (2022).
[172]C. W. Nielson and H. R. Lewis, "Particle-code models in the nonradiative limit," Methods Comput. Phys. **16**, 367 (1976).
[173]M. R. Gibbons and D. W. Hewett, "The Darwin direct implicit particle-in-cell (DADIPIC) method for simulation of low frequency plasma phenomena," J. Comput. Phys. **120**, 231 (1995).
[174]M. R. Gibbons and D. W. Hewett, "Characteization of the Darwin direct implicit particle-in-cell method and resulting guidelines for operation," J. Comput. Phys. **130**, 54 (1997).
[175]G. Chen, L. Chacón, C. A. Leibs, D. A. Knoll, and W. Taitano, "Fluid preconditioning for Newton–Krylov-based, fully implicit, electrostatic particle-in-cell simulations," J. Comput. Phys. **258**, 555 (2014).
[176]H. W. Loeb, K.-H. Schartner, B. K. Meyer, D. Feili, S. Weis, and D. Kirmse, "Forty years of Giessen EP-activities and the recent RIT-microthruster development," in *29th International Electric Propulsion Conference, Princeton University, IEPC-2005-031* (Electric Rocket Propulsion Society, 2005).
[177]V. A. Godyak, R. B. Piejak, and B. M. Alexandrovich, "Observation of second harmonic currents in inductively coupled plasmas," Phys. Rev. Lett. **83**, 1610 (1999).
[178]V. A. Godyak, R. B. Piejak, and B. M. Alexandrovich, "Hot plasma and nonlinear effects in inductive discharges," Phys. Plasmas **6**, 1804 (1999).
[179]D. Y. Sydorenko, A. I. Smolyakov, and Y. O. Tyshetskiy, "Simulations of ponderomotive effects in inductively coupled plasmas," Phys. Plasmas **12**, 033503 (2005).
[180]A. I. Smolyakov, D. Sydorenko, and A. Froese, "Non-local ponderomotive force in finite temperature inductive plasmas," Plasma Phys. Control. Fusion **49**, A221 (2007).
[181]H. Takekida and K. Nanbu, "Self-consistent particle modeling of inductively coupled cf_4 discharges and radical flow," IEEE Trans. Plasma Sci. **34**, 973 (2006).
[182]Y. Takao, K. Eriguchi, and K. Ono, "Two-dimensional particle-in-cell simulation of a micro RF ion thruster," in *The 32nd International Electric Propulsion Conference, Wiesbaden, Germany, IEPC-2011-076* (Electric Rocket Propulsion Society, 2011).
[183]R. Henrich, M. Becker, and C. Heiliger, "Investigation of the plasma in a RIT using PIC modelling," in *the 35th International Electric Propulsion Conference Georgia Institute of Technology, Atlanta, GA, USA, IEPC-2017-518* (Electric Rocket Propulsion Society, 2017).
[184]B. W. Yu and S. L. Girshick, "Modeling inductively coupled plasmas: The coil current boundary condition," J. Appl. Phys. **69**, 656 (1991).
[185]X. Chen and E. Pfender, "Modeling of rf plasma torch with a metallic tube inserted for reactant injection," Plasma Chem. Plasma Process. **11**, 103 (1991).
[186]Y. Takao, K. Eriguchi, and K. Ono, "Effect of capacitive coupling in a miniature inductively coupled plasma source," J. Appl. Phys. **112**, 093306 (2012).
[187]Y. Takao and K. Takahashi, "Numerical validation of axial plasma momentum lost to a lateral wall induced by neutral depletion," Phys. Plasmas **22**, 113509 (2015).
[188]T. Hayami, S. Yoshinari, R. Terasaki, A. Hatayama, and A. Fukano, "Analysis of discharge initiation in a rf hydrogen negative ion source," AIP Conf. Proc. **1390**, 339 (2011).
[189]S. Mattei, M. Ohta, M. Yasumoto, A. Hatayama, J. Lettry, and A. Grudiev, "Plasma ignition and steady state simulations of the Linac4 H^- ion source," Rev. Sci. Instrum. **85**, 02B115 (2014).
[190]S. Mattei, K. Nishida, S. Mochizuki, A. Grudiev, J. Lettry, M. Tran, and A. Hatayama, "Kinetic simulations and photometry measurements of the E-H transition in cylindrical inductively coupled plasmas," Plasma Sources Sci. Technol. **25**, 065001 (2016).
[191]K. Nishida, S. Mattei, S. Mochizuki, J. Lettry, and A. Hatayama, "Kinetic modeling of E-to-H mode transition in inductively coupled hydrogen plasmas," J. Appl. Phys. **119**, 233302 (2016).
[192]K. Takahashi, C. Charles, R. W. Boswell, Y. Takao, A. Fruchtman, J. Navarro-Cavallé, and M. Merino, "Commentary: On helicon thrusters: Will they ever fly?," Front. Phys. **8**, 277 (2020).
[193]R. W. Boswell, "Very efficient plasma generation by whistler waves near the lower hybrid frequency," Plasma Phys. Control. Fusion **26**, 1147 (1984).
[194]K. Takahashi, "Thirty percent conversion efficiency from radiofrequency power to thrust energy in a magnetic nozzle plasma thruster," Sci. Rep. **12**, 18618 (2022).
[195]F. F. Chen, "Plasma ionization by helicon waves," Plasma Phys. Control. Fusion **33**, 339 (1991).
[196]F. F. Chen, "Helicon discharges and sources: A review," Plasma Sources Sci. Technol. **24**, 014001 (2015).
[197]T. Isayama, S. Shinohara, and T. Hada, "Review of helicon high-density plasma: Production mechanism and plasma/wave characteristics," Plasma Fusion Res. **13**, 1101014 (2018).

[198]S. Shinohara, *High-Density Helicon Plasma Science* (Springer Nature Singapore Pte Ltd., 2022).
[199]K. P. Shamrai, V. P. Pavlenko, and V. B. Taranov, "Excitation, conversion and damping of waves in a helicon plasma source driven by an $m = 0$ antenna," Plasma Phys. Control. Fusion **39**, 505 (1997).
[200]V. F. Virko, G. S. Kirichenko, and K. P. Shamrai, "Parametric ion-acoustic turbulence in a helicon discharge," Plasma Sources Sci. Technol. **12**, 217 (2003).
[201]K. Niemi and M. Krämer, "Helicon mode formation and radio frequency power deposition in a helicon-produced plasma," Phys. Plasmas **15**, 073503 (2008).
[202]K. Emoto, K. Takahashi, and Y. Takao, "Density profile transition and high-energy electron transport in a magnetically expanding radio frequency plasma," Phys. Plasmas **30**, 013509 (2023).
[203]S. Shinohara, H. Nishida, T. Tanikawa, T. Hada, I. Funaki, and K. P. Shamrai, "Development of electrodeless plasma thrusters with high-density helicon plasma sources," IEEE Trans. Plasma Sci. **42**, 1245 (2014).
[204]K. Takase, K. Takahashi, and Y. Takao, "Effects of neutral distribution and external magnetic field on plasma momentum in electrodeless plasma thrusters," Phys. Plasmas **25**, 023507 (2018).
[205]K. Emoto, K. Takahashi, and Y. Takao, "Axial momentum gains of ions and electrons in magnetic nozzle acceleration," Plasma Sources Sci. Technol. **30**, 115016 (2021).
[206]K. Emoto, K. Takahashi, and Y. Takao, "Numerical investigation of internal plasma currents in a magnetic nozzle," Phys. Plasmas **28**, 093506 (2021).
[207]Y. Yamashita, Y. Tani, R. Tsukizaki, D. Koda, and K. Nishiyama, "Numerical investigation of plasma properties for the microwave discharge ion thruster μ 10 using PIC-MCC simulation," Phys. Plasmas **26**, 073510 (2019).
[208]N. G. Denisov, "On a singularity of the field of an electromagnetic wave propagated in an lnhomogeneous plasma," Sov. Phys. JETP **4**, 544 (1957).
[209]M. C. Williamson, A. J. Lichtenberg, and M. A. Lieberman, "Self-consistent electron cyclotron resonance absorption in a plasma with varying parameters," J. Appl. Phys. **72**, 3924 (1992).
[210]R. Geller, *Electron Cyclotron Resonance Ion Sources and ECR Plasmas* (Taylor and Francis Ltd, 1996).
[211]J. Porto and P.-Q. Elias, "Full-PIC simulation of an ECR plasma thruster with magnetic nozzle," in *The 36th International Electric Propulsion Conference University of Vienna, Austria, IEPC-2019-232* (Electric Rocket Propulsion Society, 2019).
[212]Y. Takao, K. Hiramoto, Y. Nakagawa, Y. Kasagi, H. Koizumi, and K. Komurasaki, "Electron extraction mechanisms of a micro-ECR neutralizer," Jpn. J. Appl. Phys. **55**, 07LD09 (2016).
[213]K. Hiramoto, Y. Nakagawa, H. Koizumi, and Y. Takao, "Effects of E × B drift on electron transport across the magnetic field in a miniature microwave discharge neutralizer," Phys. Plasmas **24**, 064504 (2017).
[214]K. Nakamura, Y. Nakagawa, H. Koizumi, and Y. Takao, "Numerical analysis of a miniature microwave-discharge ion thruster using water as the propellant," Trans. Jpn. Soc. Aeronaut. Space Sci. **61**, 152 (2018).
[215]K. Nakamura, H. Koizumi, M. Nakano, and Y. Takao, "Effects of negative ions on discharge characteristics of water plasma source for a miniature microwave discharge ion thruster," Phys. Plasmas **26**, 043508 (2019).
[216]Y. Sato, H. Koizumi, M. Nakano, and Y. Takao, "Electron extraction enhancement via the magnetic field in a miniature microwave discharge neutralizer," J. Appl. Phys. **126**, 243302 (2019).
[217]Y. Fua, J. Yang, Y. Jin, X. Xia, and H. Meng, "Equivalent two-dimensional numerical simulation of an ECR neutralizer," Acta Astronaut. **164**, 387 (2019).
[218]Y. Fu, J. Yang, G. H. X. Wu, Z. Hu, and X. Xia, "Simulation study on electron extraction mechanism of an ECR neutralizer," Vacuum **184**, 109932 (2021).
[219]Y. Fu, J. Yang, H. Mou, R. Tan, X. Xia, and Z. Gao, "Integrative simulation of a 2 cm electron cyclotron resonance ion source with full particle-in-cell method," Comput. Phys. Commun. **278**, 108395 (2022).
[220]N. Gascon, M. Dudeck, and S. Barral, "Wall material effects in stationary plasma thrusters. I. Parametric studies of an SPT-100," Phys. Plasmas **10**, 4123–4136 (2003).
[221]S. Barral, K. Makowski, Z. Peradzyński, N. Gascon, and M. Dudeck, "Wall material effects in stationary plasma thrusters. II. Near-wall and in-wall conductivity," Phys. Plasmas **10**, 4137–4152 (2003).
[222]Y. Raitses, A. Smirnov, D. Staack, and N. J. Fisch, "Measurements of secondary electron emission effects in the Hall thruster discharge," Phys. Plasmas **13**, 014502 (2006).
[223]S. Tsikata, A. Héron, and C. Honoré, "Hall thruster microturbulence under conditions of modified electron wall emission," Phys. Plasmas **24**, 053519 (2017).
[224]A. Dominguez-Vázquez, F. Taccogna, and E. Ahedo, "Particle modeling of radial electron dynamics in a controlled discharge of a Hall thruster," Plasma Sources Sci. Technol. **27**, 064006 (2018).
[225]A. Dominguez-Vázquez, F. Taccogna, P. Fajardo, and E. Ahedo, "Parametric study of the radial plasma-wall interaction in a Hall thruster," J. Phys. D: Appl. Phys. **52**, 474003 (2019).
[226]A. Marín-Cebrián, A. Domínguez-Vázquez, P. Fajardo, and E. Ahedo, "Macroscopic plasma analysis from 1D-radial kinetic results of a Hall thruster discharge," Plasma Sources Sci. Technol. **30**, 115011 (2021).
[227]A. Marín-Cebrián, A. Domínguez-Vázquez, P. Fajardo, and E. Ahedo, "Kinetic plasma dynamics in a radial model of a Hall thruster with a curved magnetic field," Plasma Sources Sci. Technol. **31**, 115003 (2022).
[228]F. Taccogna, S. Longo, M. Capitelli, and R. Schneider, "Surface-driven asymmetry and instability in the acceleration region of Hall thruster," Contrib. Plasma Phys. **48**, 375–386 (2008).
[229]F. Taccogna, "Non-classical plasma sheaths: Space-charge-limited and inverse regimes under strong emission from surfaces," Eur. Phys. J. D **68**, 199 (2014).
[230]I. D. Kaganovich, Y. Raitses, D. Sydorenko, and A. Smolyakov, "Kinetic effects in a Hall thruster discharge," Phys. Plasmas **14**, 057104 (2007).
[231]A. Bogaerts and R. Gijbels, "The ion- and atom-induced secondary electron emission yield: Numerical study for the effect of clean and dirty cathode surfaces," Plasma Sources Sci. Technol. **11**, 27 (2002).
[232]F. Taccogna, S. Longo, M. Capitelli, and R. Schneider, "Anomalous transport induced by sheath instability in Hall effect thrusters," Appl. Phys. Lett. **94**, 251502 (2009).
[233]A. Dunaevsky, Y. Raitses, and N. J. Fisch, "Secondary electron emission from dielectric materials of a Hall thruster with segmented electrodes," Phys. Plasmas **10**, 2574–2577 (2003).
[234]P. Tolias, "On secondary electron emission and its semi-empirical description," Plasma Phys. Control. Fusion **56**, 123002 (2014).
[235]D. Sydorenko, "Particle-in-cell simulations of electron dynamics in low pressure discharges with magnetic fields," Ph.D. thesis (Department of Physics and Engineering Physics, University of Saskatchewan, 2006), unpublished thesis.
[236]M. Villemant, M. Belhaj, P. Sarrailh, S. Dadouch, L. Garrigues, and C. Boniface, "Measurements of electron emission under electron impact on BN sample for incident electron energy between 10 eV and 1000 eV," Europhys. Lett. **127**, 23001 (2019).
[237]M. A. Furman and M. T. F. Pivi, "Probabilistic model for the simulation of secondary electron emission," Phys. Rev. ST Accel. Beams **5**, 124404 (2002).
[238]H.-Y. Chang, A. Alvarado, T. Weber, and J. Marian, "Monte carlo modeling of low-energy electron-induced secondary electron emission yields in micro-architected boron nitride surfaces," Nucl. Instrum. Methods Phys. Res., Sect. B **454**, 14–22 (2019).
[239]T. Tondu, M. Belhaj, and V. Inguimbert, "Electron-emission yield under electron impact of ceramics used as channel materials in Hall-effect thrusters," J. Appl. Phys. **110**, 093301 (2011).
[240]A. N. Andronov, A. S. Smirnov, I. D. Kaganovich, E. A. Startsev, Y. Raitses, and V. I. Demidov, "Secondary electron emission yield in the limit of low electron energy," arXiv:1309.4658 (2013). doi:10.5170/CERN-2013-002.161.
[241]L. A. Gonzalez, M. Angelucci, R. Larciprete, and R. Cimino, "The secondary electron yield of noble metal surfaces," AIP Adv. **7**, 115203 (2017).
[242]J. Löffler, M. Belhaj, N. Bundaleski, J. J. D. Leon, J. Thomet, S. Frey, C. Ballif, and N. Wyrsch, "A comprehensive analysis of electron emission from a-Si:H/Al_2O_3 at low energies," J. Phys. D: Appl. Phys. **56**, 065306 (2023).

[243]F. X. Bronold, K. Rasek, and H. Fehske, "Electron microphysics at plasma-solid interfaces," J. Appl. Phys. **128**, 180908 (2020).
[244]V. Pigeon, N. Claire, C. Arnas, K. Terasaka, and S. Inagaki, "Plasma sheath material induced dependence due to secondary electron emission," Phys. Plasmas **27**, 043505 (2020).
[245]A. Jablonski, "Angular distribution of elastic electron backscattering from surfaces: Determination of the electron inelastic mean free path," J. Phys. D: Appl. Phys. **47**, 055301 (2013).
[246]M. Villemant, P. Sarrailh, M. Belhaj, C. Inguimbert, O. Vermorel, L. Garrigues, and C. Boniface, "Electron emission model for Hall thruster plasma modelling," in *The 35th International Electric Propulsion Conference, Georgia Institute of Technology, Atlanta, GA, USA, October 8–12, 2017, IEPC-2017-366* (Electric Rocket Propulsion Society, 2017).
[247]J. Greenwood, "The correct and incorrect generation of a cosine distribution of scattered particles for Monte-Carlo modelling of vacuum systems," Vacuum **67**, 217–222 (2002).
[248]C. Costin, "Particle distribution functions at plasma–surface interface," AIP Adv. **10**, 115308 (2020).
[249]J. Petillo, K. Eppley, D. Panagos, P. Blanchard, E. Nelson, N. Dionne, J. DeFord, B. Held, L. Chernyakova, W. Krueger, S. Humphries, T. McClure, A. Mondelli, J. Burdette, M. Cattelino, R. True, K. Nguyen, and B. Levush, "The MICHELLE three-dimensional electron gun and collector modeling tool: Theory and design," IEEE Trans. Plasma Sci. **30**, 1238–1264 (2002).
[250]S. Cho, K. Komurasaki, and Y. Arakawa, "Kinetic particle simulation of discharge and wall erosion of a Hall thruster," Phys. Plasmas **20**, 063501 (2013).
[251]N. P. Brown and M. L. R. Walker, "Review of plasma-induced Hall thruster erosion," Appl. Sci. **10**, 3775 (2020).
[252]S. J. Araki and R. S. Martin, "Sputtered atom transport calculation via radiosity view factor model and particle data compression," Vacuum **210**, 111867 (2023).
[253]W. Eckstein and J. Biersack, "Reflection of heavy ions," Z. Phys. B: Condens. Matter **63**, 471–478 (1986).
[254]G. Ito, R. Kawashima, K. Komurasaki, and H. Koizumi, "Incident angle dependence of reflected particles in low-energy xenon-ion impacts on metal surfaces," Comput. Mater. Sci. **186**, 109989 (2021).
[255]V. A. Shuvalov, "Energy accommodation for gas ions on a polycrystalline material," J. Appl. Mech. Tech. Phys. **24**, 778–785 (1983).
[256]J. C. Gregory and P. N. Peters, "A measurement of the angular distribution of 5 eV atomic oxygen scattered off a solid surface in earth orbit," in *Proceedings of the 14th International Symposium on Rarefied Gas Dynamics*, July 16–20 (Tsukuba Science City, Japan, 1984).
[257]K. Moe and M. M. Moe, "Gas–surface interactions and satellite drag coefficients," Planet. Space Sci. **53**, 793–801 (2005).
[258]L. Liu, G. Cai, H. Zheng, S. Shang, and B. He, "Measurement of the momentum accommodation coefficient for the interactions between electric thruster plume and a solid surface," Phys. Plasmas **27**, 053511 (2020).
[259]A. R. Gibson, M. Foucher, D. Marinov, P. Chabert, T. Gans, M. J. Kushner, and J.-P. Booth, "The role of thermal energy accommodation and atomic recombination probabilities in low pressure oxygen plasmas," Plasma Phys. Control. Fusion **59**, 024004 (2017).
[260]P. Guerrero, I. G. Mikellides, J. E. Polk, R. Carmina Monreal, and D. I. Meiron, "Critical implications of ion-surface energy accommodation and neutralization mechanism in hollow cathode physics," J. Appl. Phys. **130**, 043306 (2021).
[261]A. Domínguez-Vázquez, F. Cichocki, M. Merino, P. Fajardo, and E. Ahedo, "On heavy particle-wall interaction in axisymmetric plasma discharges," Plasma Sources Sci. Technol. **30**, 085004 (2021).
[262]R. M. Logan and J. C. Keck, "Classical theory for the interaction of gas atoms with solid surfaces," J. Chem. Phys. **49**, 860–876 (1968).
[263]D. M. Prieto, B. P. Graziano, and P. C. Roberts, "Spacecraft drag modelling," Prog. Aeronaut. Sci. **64**, 56–65 (2014).
[264]S. Boccelli, T. E. Magin, and A. Frezzotti, "Numerical investigation of reversed gas-feed configurations for Hall thrusters," J. Propul. Power **37**, 919–927 (2021).
[265]F. Romano, J. Espinosa-Orozco, M. Pfeiffer, G. Herdrich, N. Crisp, P. Roberts, B. Holmes, S. Edmondson, S. Haigh, S. Livadiotti, A. Macario-Rojas, V. Oiko, L. Sinpetru, K. Smith, J. Becedas, V. Sulliotti-Linner, M. Bisgaard, S. Christensen, V. Hanessian, T. K. Jensen, J. Nielsen, Y.-A. Chan, S. Fasoulas, C. Traub, D. García-Almiñana, S. Rodríguez-Donaire, M. Sureda, D. Kataria, B. Belkouchi, A. Conte, S. Seminari, and R. Villain, "Intake design for an atmosphere-breathing electric propulsion system (ABEP)," Acta Astronaut. **187**, 225–235 (2021).
[266]C. Rapisarda, P. C. Roberts, and K. L. Smith, "Design and optimisation of a passive atmosphere-breathing electric propulsion (ABEP) intake," Acta Astronaut. **202**, 77–93 (2023).
[267]M. Merino, F. Cichocki, and E. Ahedo, "A collisionless plasma thruster plume expansion model," Plasma Sources Sci. Technol. **24**, 035006 (2015).
[268]A. L. Ortega, I. Katz, I. G. Mikellides, and D. M. Goebel, "Self-consistent model of a high-power Hall thruster plume," IEEE Trans. Plasma Sci. **43**, 2875–2886 (2015).
[269]T. A. Marks, I. G. Mikellides, A. Lopez Ortega, and B. Jorns, "Hall2De simulations of a magnetic nozzle," AIAA Paper No. 2020-3642, 2020.
[270]F. Taccogna, S. Longo, and M. Capitelli, "Particle-in-cell with Monte Carlo simulation of SPT-100 exhaust plumes," J. Spacecr. Rockets **39**, 409–419 (2002).
[271]F. Taccogna, S. Longo, and M. Capitelli, "Very-near-field plume simulation of a stationary plasma thruster," Eur. Phys. J. Appl. Phys. **28**, 113–122 (2004).
[272]F. Taccogna, D. Pagano, F. Scortecci, and A. Garulli, "Three-dimensional plume simulation of multi-channel thruster configuration," Plasma Sources Sci. Technol. **23**, 065034 (2014).
[273]C. Cai, "Numerical studies on plasma plume flows from a cluster of electric propulsion devices," Aerosp. Sci. Technol. **41**, 134–143 (2015).
[274]B. Korkut, Z. Li, and D. A. Levin, "3-D simulation of ion thruster plumes using octree adaptive mesh refinement," IEEE Trans. Plasma Sci. **43**, 1706–1721 (2015).
[275]F. Filleul, O. Sutherland, F. Cipriani, and C. Charles, "Bepicolombo: A platform for improving modeling of electric propulsion-spacecraft interactions," Front. Space Technol. **2**, 639819 (2021).
[276]S. H. Kang, "PIC-DSMC simulation of a Hall thruster plume with charge exchange effects using pdfoam," Aerospace **10**, 44 (2023).
[277]F. Cichocki, M. Merino, and E. Ahedo, "Three-dimensional geomagnetic field effects on a plasma thruster plume expansion," Acta Astronaut. **175**, 190–203 (2020).
[278]F. Cichocki, J. Navarro-Cavallé, A. Modesti, and G. Ramírez Vázquez, "Magnetic nozzle and RPA simulations vs experiments for a helicon plasma thruster plume," Front. Phys. **10**, 260 (2022).
[279]F. Cichocki, A. Domínguez-Vázquez, M. Merino, P. Fajardo, and E. Ahedo, "Three-dimensional neutralizer effects on a Hall-effect thruster near plume," Acta Astronaut. **187**, 498–510 (2021).
[280]E. Ahedo, S. Correyero, J. Navarro-Cavallé, and M. Merino, "Macroscopic and parametric study of a kinetic plasma expansion in a paraxial magnetic nozzle," Plasma Sources Sci. Technol. **29**, 045017 (2020).
[281]F. Cichocki, M. Merino, and E. Ahedo, "Spacecraft-plasma-debris interaction in an ion beam shepherd mission," Acta Astronaut. **146**, 216–227 (2018).
[282]A. Modesti, F. Cichocki, J. Zhou, and E. Ahedo, "A 3D electron fluid model with energy balance for plasma plumes," in *37th International Electric Propulsion Conference, Massachusetts Institute of Technology, Cambridge, MA, USA, June 19–23, 2022, IEPC-2022-321* (Electric Rocket Propulsion Society, 2022).
[283]M. Merino, J. Mauriño, and E. Ahedo, "Kinetic electron model for plasma thruster plumes," Plasma Sources Sci. Technol. **27**, 035013 (2018).
[284]Y. Hu and J. Wang, "Fully kinetic simulations of collisionless, mesothermal plasma emission: Macroscopic plume structure and microscopic electron characteristics," Phys. Plasmas **24**, 033510 (2017).
[285]Y. Hu and J. Wang, "Expansion of a collisionless hypersonic plasma plume into a vacuum," Phys. Rev. E **98**, 023204 (2018).
[286]J. Wang and Y. Hu, "On the limitations of hybrid particle-in-cell for ion thruster plume simulations," Phys. Plasmas **26**, 103502 (2019).

[287]N. Nuwal, R. Jambunathan, and D. A. Levin, "Kinetic modeling of spacecraft surfaces in a plume backflow region," IEEE Trans. Plasma Sci. **48**, 4305–4325 (2020).
[288]M. Li, M. Merino, E. Ahedo, and H. Tang, "On electron boundary conditions in PIC plasma thruster plume simulations," Plasma Sources Sci. Technol. **28**, 034004 (2019).
[289]R. Jambunathan and D. A. Levin, "A self-consistent open boundary condition for fully kinetic plasma thruster plume simulations," IEEE Trans. Plasma Sci. **48**, 610–630 (2020).
[290]R. Procassini, C. Birdsall, and E. Morse, "A fully kinetic, self-consistent particle simulation model of the collisionless plasma–sheath region," Phys. Fluids B **2**, 3191–3205 (1990).
[291]L. Yan, P.-Y. Wang, Y.-H. Ou, and X.-L. Kang, "Numerical study of Hall thruster plume and sputtering erosion," J. Appl. Math. **2012**, 327021 (2012).
[292]E. J. Beiting, X. Le Eapen, J. E. Pollard, M. Gambon, F. R. Marchandise, and M. Oberg, "Electromagnetic emissions from PPS ®1350 Hall thruster," in *The 31st International Electric Propulsion Conference, Ann Arbor, MI, USA, IEPC-2009-71* (Electric Rocket Propulsion Society, 2009).
[293]V. Mazières, F. Gaboriau, A. Guglielmi, V. Laquerbe, R. Pascaud, and O. Pascal, "Broadband (kHz-GHz) characterization of instabilities in Hall thruster inside a metallic vacuum chamber," Phys. Plasmas **29**, 072107 (2022).
[294]N. de Mejanes, R. Pascaud, V. Mazières, A. Rossi, V. Laquerbe, L. Garrigues, and O. Pascal, "Simulation of the microwave propagation through the plume of a Hall thruster integrated on small spacecraft," J. Appl. Phys. **131**, 243303 (2022).
[295]L. Garrigues, J. Bareilles, J. P. Boeuf, and I. D. Boyd, "Modeling of the plasma jet of a stationary plasma thruster," J. Appl. Phys. **91**, 9521–9528 (2002).
[296]T. Hallouin and S. Mazouffre, "Far-field plume characterization of a 100-W class Hall thruster," Aerospace **7**, 58 (2020).
[297]M. Lieberman and A. Lichtenberg, "Plasma dynamics," in *Principles of Plasma Discharges and Materials Processing*, edited by M. Lieberman and A. Lichtenberg (John Wiley & Sons, Ltd, 2005), Chap. 4, pp. 87–132.
[298]Ansys HFSS, see https://www.ansys.com/fr-fr/products/electronics/ansys-hfss for "Low Temperature Magnetized Plasma Benchmarks" (2022) (last accessed Febuary 7, 2023).
[299]G. G. Raju, *Gaseous Electronics. Theory and Practice* (Taylor and Francis, New York, 2006).
[300]G. G. Raju, *Gaseous Electronics. Tables, Atoms, and Molecules* (Taylor and Francis, New York, 2012).
[301]see https://amdis.iaea.org/databases/ for"Iaea—Atomic and Molecular Data Unit" (2023) (last accessed March 30, 2023).
[302]see https://nl.lxcat.net/home/ for "Lxcat Database—Plasma Data Exchange Project" (2023) (last accessed March 30, 2023).
[303]see https://quantemoldb.com/ for "Quantemol db" (2023) (last accessed March 30, 2023).
[304]see https://www.nist.gov/pml/electron-impact-cross-sections-ionization-and-excitation-database/ for "Nist—Electron-Impact Cross Sections for Ionization and Excitation Database" (2023) (last accessed March 30, 2023).
[305]see http://dbshino.nifs.ac.jp for "Nifs Database. Atomic and Molecular Numerical Databases" (2023) (last accessed March 30, 2023).
[306]J. F. J. Janssen, L. C. Pitchford, G. J. M. Hagelaar, and J. van Dijk, "Evaluation of angular scattering models for electron-neutral collisions in Monte Carlo simulations," Plasma Sources Sci. Technol. **25**, 055026 (2016).
[307]R. M. Park, W. Kupets, M. C. Zammit, J. Colgan, C. J. Fontes, B. S. Scheiner, E. Timmermans, X.-Z. Tang, L. H. Scarlett, D. V. Fursa, I. Bray, and N. A. Garland, "Anisotropic angular scattering models of elastic electron-neutral collisions for Monte Carlo plasma simulations," Plasma Sources Sci. Technol. **31**, 065013 (2022).
[308]H. Wang, V. S. Sukhomlinov, I. D. Kaganovich, and A. S. Mustafaev, "Simulations of ion velocity distribution functions taking into account both elastic and charge exchange collisions," Plasma Sources Sci. Technol. **26**, 024001 (2017).
[309]R. Pan, J. Ren, R. Mao, and H. Tang, "Practical analysis of different neutral algorithms for particle simulation of Hall thruster," Plasma Sources Sci. Technol. **32**, 034005 (2023).
[310]F. Faraji, M. Reza, and A. Knoll, "Effects of the neutral dynamics model on the particle-in-cell simulations of a Hall thruster plasma discharge," J. Appl. Phys. **133**, 213301 (2023).
[311]A. Gurciullo, A. L. Fabris, and M. A. Cappelli, "Ion plume investigation of a Hall effect thruster operating with Xe/N_2 and Xe/air mixtures," J. Phys. D: Appl. Phys. **52**, 464003 (2019).
[312]F. Marchioni and M. A. Cappelli, "Extended channel Hall thruster for air-breathing electric propulsion," J. Appl. Phys. **130**, 053306 (2021).
[313]T. F. Munro-O'Brien and C. N. Ryan, "Performance of a low power Hall effect thruster with several gaseous propellants," Acta Astronaut. **206**, 257–273 (2023).
[314]T. Lafleur, L. Habl, E. Z. Rossi, and D. Rafalskyi, "Development and validation of an iodine plasma model for gridded ion thrusters," Plasma Sources Sci. Technol. **31**, 114001 (2022).
[315]S. Andrews, R. Andriulli, N. Souhair, S. Di Fede, D. Pavarin, F. Ponti, and M. Magarotto, "Coupled global and PIC modelling of the REGULUS cathodeless plasma thrusters operating on xenon, iodine and krypton," Acta Astronaut. **207**, 227–239 (2023).
[316]A. J. Sheppard and J. M. Little, "Scaling laws for electrodeless plasma propulsion with water vapor propellant," Plasma Sources Sci. Technol. **29**, 045007 (2020).
[317]K. Shirasu, H. Kuwabara, M. Matsuura, H. Koizumi, Y. Nakagawa, H. Watanabe, H. Sekine, and K. Komurasaki, "Demonstration and experimental characteristics of a water-vapor Hall thruster," J. Electr. Propul. **2**, 11 (2023).
[318]K. Hohman, "Atmospheric breathing electric thruster for planetary exploration," Tech. Rep. 10 (BUSEK Co. Inc., 2012).
[319]L. Garrigues, "Computational study of Hall-effect thruster with ambient atmospheric gas as propellant," J. Propul. Power **28**, 344–354 (2012).
[320]B. Zheng, Y. Fu, D. qi Wen, K. Wang, T. Schuelke, and Q. H. Fan, "Influence of metastable atoms in low pressure magnetized radio-frequency argon discharges," J. Phys. D: Appl. Phys. **53**, 435201 (2020).
[321]D.-Q. Wen, J. Krek, J. T. Gudmundsson, E. Kawamura, M. A. Lieberman, and J. P. Verboncoeur, "Benchmarked and upgraded particle-in-cell simulations of a capacitive argon discharge at intermediate pressure: The role of metastable atoms," Plasma Sources Sci. Technol. **30**, 105009 (2021).
[322]D.-Q. Wen, J. Krek, J. T. Gudmundsson, E. Kawamura, M. A. Lieberman, and J. P. Verboncoeur, "Particle-in-cell simulations with fluid metastable atoms in capacitive argon discharges: Electron elastic scattering and plasma density profile transition," IEEE Trans. Plasma Sci. **50**, 2548–2557 (2022).
[323]Y. Yamashita, R. Tsukizaki, and K. Nishiyama, "Importance of stepwise ionization from the metastable state in electron cyclotron resonance ion thrusters," J. Electr. Propul. **1**, 2731–4596 (2022).
[324]M. Hayashi, "Bibliography of electron and photon cross sections with atoms and molecules published in the 20th century. Xenon," NIFS, research report NIFS Data series, NIFS-DATA-79, available at www.osti.gov/etdeweb/servlets/purl/20439341
[325]H. A. Hyman, "Electron-impact ionization cross sections for excited states of the rare gases (Ne, Ar, Kr, Xe), cadmium, and mercury," Phys. Rev. A **20**, 855–859 (1979).
[326]B. Chaudhury, M. Shah, U. Parekh, H. Gandhi, P. Desai, K. Shah, A. Phadnis, M. Shah, M. Bandyopadhyay, and A. Chakraborty, "Hybrid parallelization of particle in cell Monte Carlo collision (PIC-MCC) algorithm for simulation of low temperature plasmas," in *Software Challenges to Exascale Computing*, edited by R. Majumdar and A. Arora (Springer, Singapore, 2019), pp. 32–53.
[327]J. M. Dawson, V. Decyk, R. Sydora, and P. Liewer, "High-performance computing and plasma physics," Phys. Today **46**(3), 64–70 (1993).
[328]P. Ortwein, T. Binder, S. Copplestone, A. Mirza, P. Nizenkov, M. Pfeiffer, T. Stindl, S. Fasoulas, and C.-D. Munz, "Parallel performance of a discontinuous galerkin spectral element method based PIC-DSMC solver," in *High Performance Computing in Science and Engineering '14: Transactions of the High Performance Computing Center, Stuttgart (HLRS) 2014* (Springer, 2015), pp. 671–681.
[329]R. Ismail, N. A. Wati Abdul Hamid, M. Othman, R. Latip, and M. A. Sanwani, "Point-to-point communication on gigabit ethernet and

infiniband networks," in *Informatics Engineering and Information Science: International Conference, ICIEIS 2011, Kuala Lumpur, Malaysia, November 14–16, 2011, Proceedings, Part IV* (Springer, Berlin, Heidelberg, 2011), pp. 369–382.
[330]S. J. Araki and R. S. Martin, "Dynamic load balancing with over decomposition in plasma plume simulations," J. Parallel Distrib. Comput. **163**, 136–146 (2022).
[331]H. Vincenti, M. Lobet, R. Lehe, R. Sasanka, and J.-L. Vay, "An efficient and portable SIMD algorithm for charge/current deposition in particle-in-cell codes," Comput. Phys. Commun. **210**, 145–154 (2017).
[332]D. Tskhakaya and R. Schneider, "Optimization of pic codes by improved memory management," J. Comput. Phys. **225**, 829–839 (2007).
[333]L. Garrigues, G. Fubiani, and J.-P. Boeuf, "Appropriate use of the particle-in-cell method in low temperature plasmas: Application to the simulation of negative ion extraction," J. Appl. Phys. **120**, 213303 (2016).
[334]R. Jambunathan and D. A. Levin, "Chaos: An octree-based PIC-DSMC code for modeling of electron kinetic properties in a plasma plume using mpi-cuda parallelization," J. Comput. Phys. **373**, 571 (2018).
[335]W.-m. W. Hwu, D. B. Kirk, and I. E. Hajj, *Programming Massively Parallel Processors: A Hands-on Approach* (Morgan Kaufmann, 2022).
[336]P. Mertmann, D. Eremin, T. Mussenbrock, R. Brinkmann, and P. Awakowicz, "Fine-sorting one-dimensional particle-in-cell algorithm with Monte Carlo collisions on a graphics processing unit," Comput. Phys. Commun. **182**, 2161 (2011).
[337]Z. Juhasz, J. Durian, A. Derzsi, S. Matejcik, Z. Donko, and P. Hartmann, "Efficient GPU implementation of the particle-in-cell/Monte-Carlo collisions method for 1D simulation of low-pressure capacitively coupled plasmas," Comput. Phys. Commun. **263**, 107913 (2021).
[338]G. Gallo, A. Isoldi, D. D. Gatto, R. Savino, A. Capozzoli, C. Curcio, and A. Liseno, "Numerical aspects of particle-in-cell simulations for plasma-motion modeling of electric thrusters," Aerospace **8**, 138 (2021).
[339]R. Jambunathan and D. A. Levin, "Multi-GPU PIC solver for modeling of ion thruster plasma plume," AIAA Paper No. 2018-1297, 2018.
[340]K. Nishii, S. Clark, J. Tompkins, N. Nuwal, D. A. Levin, and J. L. Rovey, "Numerical simulation of carbon sputtering for electric propulsion in the ground facility," in *37th International Electric Propulsion Conference Massachusetts Institute of Technology, Cambridge, MA, USA, IEPC-2022-379* (Electric Rocket Propulsion Society, 2022).
[341]K. Amyx, "GPU-accelerated 3-D electromagnetic particle-in-cell implementations in VORPAL," in *Proceedings of the GPU Technology Conference* (San Jose, CA, 2012).
[342]J. Leddy, S. Averkin, B. Cowan, S. Sides, and J. Cary, "Modeling collisional processes on GPU in the Vorpal code," in *2018 IEEE International Conference on Plasma Science (ICOPS)* (IEEE, 2018).
[343]J. Cheng, M. Grossman, and T. McKercher, *Professional CUDA C Programming* (Wrox, 2014).
[344]D. R. Kaeli, P. M. Mistry, D. S. Schaa, and D. P. Zhang, *Heterogeneous Computing with OpenCL 2.0* (Morgan Kaufmann, 2015).
[345]C. R. Trott, D. Lebrun-Grandié, D. Arndt, J. Ciesko, V. Dang, N. Ellingwood, R. Gayatri, E. Harvey, D. S. Hollman, D. Ibanez, and N. Liber, "Kokkos 3: Programming model extensions for the exascale era," IEEE Trans. Parallel Distrib. Syst. **33**, 805–817 (2021).
[346]D. A. Beckingsale, J. Burmark, R. Hornung, H. Jones, W. Killian, A. J. Kunen, O. Pearce, P. Robinson, B. S. Ryujin, and T. R. Scogland, "RAJA: Portable performance for large-scale scientific applications," in *2019 IEEE/ACM International Workshop on Performance, Portability and Productivity in HPC (P3HPC)* (IEEE, 2019), pp. 71–81.
[347]R. Farber, *Parallel Programming with OpenACC* (Newnes, 2016).
[348]J. Garcke, "Sparse grids in a nutshell," in *Sparse Grids and Applications*, edited by J. Garcke and M. Griebel (Springer, Berlin, 2013), pp. 57–80.
[349]M. Obersteiner and H.-J. Bungartz, "A spatially adaptive sparse grid combination technique for numerical quadrature," in *Sparse Grids and Applications—Munich 2018*, edited by H.-J. Bungartz, J. Garcke, and D. Pflüger (Springer International Publishing, Cham, 2021), pp. 161–185.
[350]L. F. Ricketson and A. J. Cerfon, "Sparse grid techniques for particle-in-cell schemes," Plasma Phys. Control. Fusion **59**, 024002 (2016).
[351]L. Garrigues, B. Tezenas du Montcel, G. Fubiani, F. Bertomeu, F. Deluzet, and J. Narski, "Application of sparse grid combination techniques to low temperature plasmas particle-in-cell simulations. I. Capacitively coupled radio frequency discharges," J. Appl. Phys. **129**, 153303 (2021).
[352]L. Garrigues, B. Tezenas du Montcel, G. Fubiani, and B. C. G. Reman, "Application of sparse grid combination techniques to low temperature plasmas particle-in-cell simulations. II. Electron drift instability in a Hall thruster," J. Appl. Phys. **129**, 153304 (2021).
[353]F. Deluzet, G. Fubiani, L. Garrigues, C. Guillet, and J. Narski, "Sparse grid reconstructions for particle-in-cell methods," ESAIM: M2AN **56**, 1809–1841 (2022).
[354]S. Muralikrishnan, A. J. Cerfon, M. Frey, L. F. Ricketson, and A. Adelmann, "Sparse grid-based adaptive noise reduction strategy for particle-in-cell schemes," J. Comput. Phys.: X **11**, 100094 (2021).
[355]F. Deluzet, G. Fubiani, L. Garrigues, C. Guillet, and J. Narski, "Efficient parallelization for 3D-3V sparse grid particle-in-cell: Shared memory systems architectures," J. Comput. Phys. **480**, 112022 (2023).
[356]F. Deluzet, G. Fubiani, L. Garrigues, C. Guillet, and J. Narski, "Efficient parallelization for 3D-3V sparse grid particle-in-cell: Single GPU architectures," Comput. Phys. Commun. **289**, 108755 (2023).
[357]M. Chung-To-Sang, L. Garrigues, T. Dubois, and S. Tsikata, "3D sparse PIC modeling of a Hall thruster: Comparisons with experimental results," in *The 37th International Electric Propulsion Conference, Massachusetts Institute of Technology, Cambridge, MA, USA, IEPC-2022-316* (Electric Rocket Propulsion Society, 2022).
[358]A. Friedman, A. B. Langdon, and B. I. Cohen, "A direct method for implicit particle-in-cell simulation," Commun. Plasma Phys. Control. Fusion **6**, 225 (1981).
[359]A. B. Langdon and D. C. Barnes, "Direct implicit plasma simulation," in *Multiple Time Scales* (Academic Press, Inc., 1985), Chap. 11, p. 335.
[360]R. J. Mason, "Implicit moment particle simulation of plasmas," J. Comput. Phys. **41**, 233 (1981).
[361]J. U. Brackbill and D. W. Forslund, "Simulation of low-frequency, electromagnetic phenomena in plasmas," in *Multiple Time Scales* (Academic Press, Inc., 1985), Chap. 9, p. 271.
[362]R. Clark and T. Hughes, *User Manual for the Commercial Software LSP* (Mission Research Corporation, Santa Barbara, CA, 2005).
[363]J.-L. Vay, D. P. Grote, R. H. Cohen, and A. Friedman, "Novel methods in the particle-in-cell accelerator code-framework warp," Comput. Sci. Discov. **5**, 014019 (2013).
[364]J. Carlsson, A. Khrabrov, I. Kaganovich, D. Keating, S. Selezneva, and T. Sommerer, "Low-temperature plasma simulations with the LSP PIC code," in *APS Division of Plasma Physics Meeting Abstracts, APS Meeting Abstracts* (APS, 2014), Vol. 2014, p. GP8.110.
[365]D. Levko, Ya. E. Krasik, V. Vekselman, and I. Haber, "Two-dimensional model of orificed micro-hollow cathode discharge for space application," Phys. Plasmas **20**, 083512 (2013).
[366]I. D. Kaganovich, C. Lan, A. T. Powis, A. V. Khrabrov, J. Carlsson, Y. Raitses, S. Janhunen, L. Xu, A. Smolyakov, and D. Sydorenko, "Towards predictive kinetic simulations of Hall thrusters and on ubiquitous formation of solitons," in *36th International Electric Propulsion Conference, University of Vienna, IEPC-2019-543* (Electric Rocket Propulsion Society, 2019).
[367]L. Lei, X. Jin, J. Li, L. Li, and B. Li, "Some aspects of the plasma potential in 3D simulation of ECRIS operation," Phys. Plasmas **29**, 073904 (2022).
[368]S. Cho, K. Komurasaki, and Y. Arakawa, "Lifetime simulation of a spt type Hall thruster by using a 2D fully kinetic pic model," AIAA Paper No. AIAA 2012-4016, 2012.
[369]A. B. Langdon, "'Energy-conserving' plasma simulation algorithms," J. Comput. Phys. **12**, 247 (1973).
[370]H. Ueda, Y. Omura, H. Matsumoto, and T. Okuzawa, "A study of the numerical heating in electrostatic particle simulations," Comput. Phys. Commun. **79**, 249 (1994).

[371]L. Chacón, G. Chen, and D. C. Barnes, "A charge- and energy-conserving implicit, electrostatic particle-in-cell algorithm on mapped computational meshes," J. Comput. Phys. **233**, 1 (2013).
[372]P. Parodi, G. Lapenta, and T. Magin, "Simulation of plasmas for electric propulsion using the energy-conserving semi-implicit PIC scheme," in *9th European Conference for Aeronautics and Space Sciences (EUCASS)* (EUCASS Association, 2022).
[373]G. Lapenta, "Exactly energy conserving semi-implicit particle in cell formulation," J. Comput. Phys. **334**, 349 (2017).
[374]G. Lapenta, "Advances in the implementation of the exactly energy conserving semi-implicit (ECsim) particle-in-cell method," Physics **5**, 72 (2023).
[375]H. R. Lewis, "Energy-conserving numerical approximations for Vlasov plasmas," J. Comput. Phys. **6**, 136 (1970).
[376]B. Berger, D. Eremin, M. Oberberg, D. Engel, C. Woelfel, Q.-Z. Zhang, P. Awakowicz, J. Lunze, R. Brinkmann, and J. Schulze, "Electron dynamics in planar radio frequency magnetron plasmas: III. Comparison of experimental investigations of power absorption dynamics to simulation results," Plasma Sources Sci. Technol. **32**, 045009 (2023).
[377]F. Faraji, M. Reza, and A. Knoll, "Enhancing one-dimensional particle-in-cell simulations to self-consistently resolve instability-induced electron transport in Hall thrusters," J. Appl. Phys. **131**, 193302 (2022).
[378]F. Faraji, M. Reza, and A. Knoll, "Verification of the generalized reduced-order particle-in-cell scheme in a radial–azimuthal E × B plasma configuration," AIP Adv. **13**, 025315 (2023).
[379]M. Reza, F. Faraji, and A. Knoll, "Resolving multi-dimensional plasma phenomena in Hall thrusters using the reduced-order particle-in-cell scheme," J. Electr. Propul. **1**, 19 (2022).
[380]M. Reza, F. Faraji, and A. Knoll, "Concept of the generalized reduced-order particle-in-cell scheme and verification in an axial-azimuthal Hall thruster configuration," J. Phys. D: Appl. Phys. **56**, 175201 (2023).
[381]M. Reza, F. Faraji, and A. Knoll, "Parametric investigation of azimuthal instabilities and electron transport in a radial-azimuthal ExB plasma configuration," J. Appl. Phys. **133**, 123301 (2023).
[382]K. Fujita, Y. Kikuchi, T. Ichimura, M. Hori, L. Maddegedara, and N. Ueda, *GPU Porting of Scalable Implicit Solver with Green's Function-Based Neural Networks by Openacc* (Springer-Verlag, Berlin, 2021).
[383]S. Markidis, "The old and the new: Can physics-informed deep-learning replace traditional linear solvers?," Front. Big Data **4**, 669097 (2021).
[384]X. Guo, W. Li, and F. Iorio, "Convolutional neural networks for steady flow approximation," in *Proceedings of the 22nd ACM SIGKDD International Conference on Knowledge Discovery and Data Mining, KDD '16* (Association for Computing Machinery, New York, 2016), pp. 481–490.
[385]X.-Y. Xu, M. Shao, P.-L. Chen, and Q.-G. Wang, "Tropical cyclone intensity prediction using deep convolutional neural network," Atmosphere **13**, 783 (2022).
[386]X. Aguilar and S. Markidis, in *2021 IEEE International Conference on Cluster Computing (CLUSTER)* (IEEE, 2021), pp. 692–697.
[387]B. Jorns, "Predictive, data-driven model for the anomalous electron collision frequency in a Hall effect thruster," Plasma Sources Sci. Technol. **27**, 104007 (2018).
[388]T. A. Marks and B. A. Jorns, "Challenges with the self-consistent implementation of closure models for anomalous electron transport in fluid simulations of Hall thrusters," Plasma Sources Sci. Technol. **32**, 045016 (2023).
[389]D. Maddaloni, A. Domínguez-Vázquez, F. Terragni, and M. Merino, "Data-driven analysis of oscillations in Hall thruster simulations," Plasma Sources Sci. Technol. **31**, 045026 (2022).
[390]M. Lee, D. Kim, J. Lee, Y. Kim, and M. Yi, "A data-driven approach for analyzing Hall thruster discharge instability leading to plasma blowoff," Acta Astronaut. **206**, 1–8 (2023).
[391]L.F. Ricketson and L. Chacón, "An energy-conserving and asymptotic-preserving charged-particle orbit implicit time integrator for arbitrary electromagnetic fields," J. Computational Physics **418**, 109639 (2020).